2018

Quantitative Multimodal Mapping Of Seizure Networks In Drug-Resistant Epilepsy

Preya Shah
University of Pennsylvania, preya.a.shah@gmail.com

Quantitative Multimodal Mapping Of Seizure Networks In Drug-Resistant Epilepsy

Abstract
Over 15 million people worldwide suffer from localization-related drug-resistant epilepsy. These patients are candidates for targeted surgical therapies such as surgical resection, laser thermal ablation, and neurostimulation. While seizure localization is needed prior to surgical intervention, this process is challenging, invasive, and often inconclusive. In this work, I aim to exploit the power of multimodal high-resolution imaging and intracranial electroencephalography (iEEG) data to map seizure networks in drug-resistant epilepsy patients, with a focus on minimizing invasiveness. Given compelling evidence that epilepsy is a disease of distorted brain networks as opposed to well-defined focal lesions, I employ a graph-theoretical approach to map structural and functional brain networks and identify putative targets for removal. The first section focuses on mesial temporal lobe epilepsy (TLE), the most common type of localization-related epilepsy. Using high-resolution structural and functional 7T MRI, I demonstrate that noninvasive neuroimaging-based network properties within the medial temporal lobe can serve as useful biomarkers for TLE cases in which conventional imaging and volumetric analysis are insufficient. The second section expands to all forms of localization-related epilepsy. Using iEEG recordings, I provide a framework for the utility of interictal network synchrony in identifying candidate resection zones, with the goal of reducing the need for prolonged invasive implants. In the third section, I generate a pipeline for integrated analysis of iEEG and MRI networks, paving the way for future large-scale studies that can effectively harness synergy between different modalities. This multimodal approach has the potential to provide fundamental insights into the pathology of an epileptic brain, robustly identify areas of seizure onset and spread, and ultimately inform clinical decision making.

Degree Type
Dissertation

Degree Name
Doctor of Philosophy (PhD)

Graduate Group
Bioengineering

First Advisor
Brian Litt

Second Advisor
Kathryn A. Davis

Keywords
Electrophysiology, Epilepsy, Intracranial EEG, MRI, Network Neuroscience, Neuroimaging

QUANTITATIVE MULTIMODAL MAPPING OF SEIZURE NETWORKS IN DRUG-RESISTANT EPILEPSY

Preya Shah

A DISSERTATION

in

Bioengineering

Presented to the Faculties of the University of Pennsylvania

in

Partial Fulfillment of the Requirements for the

Degree of Doctor of Philosophy

2018

Supervisor of Dissertation

Brian Litt, M.D.
Professor of Bioengineering and Neurology

Co-Supervisor of Dissertation

Kathryn A. Davis, M.D., M.T.R.
Assistant Professor of Neurology

Graduate Group Chairperson

Ravi Radhakrishnan, Ph.D.
Professor of Bioengineering

Dissertation Committee

Danielle S. Bassett, Ph.D., Associate Professor of Bioengineering, Electrical & Systems Engineering, Physics & Astronomy, and Neurology
Paul Yushkevich, Ph.D., Associate Professor of Radiology
Russell Taki Shinohara, Ph.D., Associate Professor of Biostatistics, Epidemiology, and Informatics

QUANTITATIVE MULTIMODAL MAPPING OF SEIZURE NETWORKS IN DRUG-RESISTANT EPILEPSY

Dedicated to my parents,
for their unwavering love and support

Acknowledgements

The work presented in this thesis would not have been possible without the assistance and support of many people.

First, I would like to thank Dr. Brian Litt for welcoming me into his lab and for going far above and beyond the call of duty as a thesis advisor. Brian offered me the freedom to think up and work on projects most interesting to me, while guiding me towards research questions that are both quantitatively rigorous and clinically impactful. He has fostered in me a sense of intellectual independence and has shared many valuable nuggets of career advice along the way. Brian is a leader in his field and wears many hats, including treating patients, running a lab, teaching courses, leading organizations, and of course, mentoring graduate students. It is inspiring to watch him manage his many roles with astounding success and humility, along with a healthy sense of humor. Brian cares deeply about his trainees and I could not be more grateful.

Brian also introduced me to my co-advisor, Dr. Kate Davis. Kate juggles the dual roles of physician and scientist remarkably efficiently and seemingly effortlessly. She took me under her wing early on, and has been a significant mentor and role model to me. Kate has achieved incredible success in a short amount of time, and I have learned a lot from her example. Together, Brian and Kate embody the qualities of a physician-scientist that I hope to emulate in my future career.

I am thankful for the time and support of my thesis committee: Dr. Danielle (Dani) Bassett, Dr. Paul Yushkevich, and Dr. Russell (Taki) Shinohara. Dani has graciously lent her expertise to my projects, and much of the work presented in this thesis is motivated by her seminal contributions to the field of network neuroscience. Paul always brings astute insights to my committee meetings, and I am inspired by his commitment to developing open-source tools such as ITK-SNAP and ASHS, which have directly benefited my work and the work of many others worldwide. Taki has a wealth of statistical knowledge which he has generously shared with me; I thank him for introducing me to new statistical techniques, lending me textbooks, and engendering in me a newfound enthusiasm for biostatistics.

I've also had the opportunity to receive advice from several experts in the neuroimaging community at Penn, including Dr. Joel Stein and Dr. John Detre. Dr. Sandy Das served as a valuable mentor during my first couple of projects in graduate school, and helped me learn the ropes of fMRI processing and analysis. Dr. James Gee welcomed me into the HHMI-NIBIB Imaging Interfaces Program, which allowed me to gain exposure to many facets of medical imaging.

I am incredibly appreciative of the entire Litt Lab family. Carolyn Wilkinson, Ruthie Krieger, and Everett Prince are the true MVPs who take care of the nuts and bolts of running the lab and keeping it thriving. Many thanks to the "data wizards" who have been instrumental in helping me obtain and curate the multimodal patient data needed for this thesis work: Jacqueline Boccanfuso, Ryan Archer, Kelly Oeschel, Magda Wernovsky, Heather Gatens, and John Frommeyer. Thank you to Dr. Arian Ashourvan for his enthusiastic guidance and encouragement, Dr. Fadi Mikhail for his important clinical insights, and Dr. Shawniqua Williams for the opportunity to work with her on interesting projects. Finally, thank you to all labmates, both past and present, including: Nicki Driscoll, Brendan Murphy, Flavia Vitale, Steve Baldassano, Lohith Kini, Hoameng Ung, John Bernabei, Peter Hadar, Nick Apollo, Hank Bink, Ankit Khambhati, Andrew Zhao, Pippa Karoly, and many others. They have made every day fun, both in and out of lab. Thanks for the laughs and adventures.

Thank you to Dr. Skip Brass and Maggie Krall of the Penn Medical Scientist Training Program for their continuous support.

Last but certainly not least, I am infinitely grateful to my family for encouraging my intellectual curiosity at an early age, and for their life-long love and support.

ABSTRACT

QUANTITATIVE MULTIMODAL MAPPING OF SEIZURE NETWORKS IN DRUG-RESISTANT EPILEPSY

Preya Shah

Brian Litt, M.D.

Over 15 million people worldwide suffer from localization-related drug-resistant epilepsy. These patients are candidates for targeted surgical therapies such as surgical resection, laser thermal ablation, and neurostimulation. While seizure localization is needed prior to surgical intervention, this process is challenging, invasive, and often inconclusive. In this work, I aim to exploit the power of multimodal high-resolution imaging and intracranial electroencephalography (iEEG) data to map seizure networks in drug-resistant epilepsy patients, with a focus on minimizing invasiveness. Given compelling evidence that epilepsy is a disease of distorted brain networks as opposed to well-defined focal lesions, I employ a graph-theoretical approach to map structural and functional brain networks and identify putative targets for removal. The first section focuses on mesial temporal lobe epilepsy (TLE), the most common type of localization-related epilepsy. Using high-resolution structural and functional 7T MRI, I demonstrate that noninvasive neuroimaging-based network properties within the medial temporal lobe can serve as useful biomarkers for TLE cases in which conventional imaging and volumetric analysis are insufficient. The second section expands to all forms of localization-related epilepsy. Using iEEG recordings, I provide a framework for the utility of interictal network synchrony in identifying candidate resection zones, with the goal of reducing the need for prolonged invasive implants. In the third section, I generate a pipeline for integrated analysis of iEEG and MRI networks, paving the way for future large-scale studies that can effectively harness synergy between different modalities. This multimodal approach has the potential to provide fundamental insights into the pathology of an epileptic brain, robustly identify areas of seizure onset and spread, and ultimately inform clinical decision making.

Table of Contents

ACKNOWLEDGEMENTS **IV**

ABSTRACT **VI**

TABLE OF CONTENTS **VII**

LIST OF TABLES **X**

LIST OF ILLUSTRATIONS **XI**

CHAPTER 1: INTRODUCTION **1**

CHAPTER 2: BACKGROUND **5**

CHAPTER 3: USING HIGH-RESOLUTION MRI TO MAP THE MEDIAL TEMPORAL SUBREGIONAL NETWORK **9**

3.1 ABSTRACT 10
3.2 INTRODUCTION 11
3.3 METHODS 14
3.3.1 Subjects 14
3.3.2 Image Acquisition 15
3.3.3 MTL Segmentation 16
3.3.4. MTL Volumetry 19
3.3.5 Functional and Structural Network Generation 20
3.3.6 Functional and Structural Network Analysis 23
3.3.7 Statistical Analysis 27
3.3.8 Reproducibility Analysis 29
3.3.9 Software 30
3.4. RESULTS 30
3.4.1 MTL Volumetric Analysis 30
3.4.2 MTL Network Findings 31
3.5. DISCUSSION 36
3.5.1 MTL volumetric and network findings 36
3.5.2 Methodological Considerations and Limitations 39
3.5.3 Conclusion 42
3.6 ACKNOWLEDGMENTS 43
3.7 SUPPLEMENTARY MATERIAL 43
3.7.1 Binary Network Analysis 43
3.7.2 Supplementary Figures 45

CHAPTER 4: USING MRI TO UNCOVER MEDIAL TEMPORAL NETWORK ASYMMETRY IN TEMPORAL LOBE EPILEPSY **53**

4. 1 ABSTRACT 54
4.2 INTRODUCTION 55

4.3 METHODS 58
4.3.1 Subjects 58
4.3.2 Image Acquisition 59
4.3.3 MTL Segmentation 60
4.3.4 MTL Volumetric Asymmetry from Structural MRI 62
4.3.5 MTL Functional Network Asymmetry 63
4.3.6 Statistical Analysis 64
4.3.7 Software 65
4.4. RESULTS 65
4.4.1 MTL Volumetric Asymmetry 65
4.4.2 MTL Functional Network Asymmetry 67
4.5 DISCUSSION 68
4.5.1 Asymmetry-based findings 69
4.5.2 Methodological Considerations and Limitations 71
4.5.3 Conclusion 72
4.6 SUPPLEMENTARY INFORMATION 72
4.6.1 Mathematical definitions and intuitive descriptions of network metrics 72
4.6.2 Supplementary Figures 75
CHAPTER 5: USING INTRACRANIAL EEG TO MAP BRAIN NETWORKS 76
5.1 ABSTRACT 77
5.2 INTRODUCTION 78
5.3 METHODS 81
5.3.1 Patients 81
5.3.2 Task Procedures 82
5.3.3 EEG Collection and Behavioral Recording 83
5.3.4 EEG Analysis 84
5.3.5 Statistical Analyses 85
5.4 RESULTS 86
5.4.1 Subjects and behavioral task performance 86
5.4.2 Spatiotemporal activation patterns associated with word utterances 88
5.4.3 Comparison of patterns for category- and letter-motivated utterances 92
5.5 DISCUSSION 93
5.5.1 Spatial and temporal dynamics of spontaneous utterances 94
5.5.2 Category-motivated versus letter-motivated verbal fluency 98
5.5.3 Potential contribution of the medial temporal region 100
5.5.4 Toward a model of verbal fluency 101
5.5.5 Implications for invasive strategies to improve language function 103
5.5.6 Limitations 104
5.5.7 Conclusions 107
5.6 ACKNOWLEDGEMENTS 108
5.7 SUPPLEMENTARY INFORMATION 108
5.7.1 Detailed Description of Statistical Analyses 108
5.7.2 Supplementary Figures 111

CHAPTER 6: USING INTRACRANIAL EEG TO LOCALIZE EPILEPTIC NETWORKS 115
6.1 ABSTRACT 116
6.2 INTRODUCTION 117
6.3 METHODS 119
6.3.1 Subjects 119
6.3.2 Intracranial EEG acquisition 121
6.3.3 Electrode and resection zone localization 121
6.3.4 Functional network analysis 122
6.4 RESULTS 125
6.5 DISCUSSION 129
6.5.1 High interictal connectivity within resection zone is associated with good outcomes 130
6.5.2 Methodological Considerations and Limitations 133
6.5.3 Conclusion 134
7. ACKNOWLEDGEMENTS 134
CHAPTER 7: MERGING NEUROIMAGING AND ELECTROPHYSIOLOGY 135
7.1 ABSTRACT 136
7.2 INTRODUCTION 137
7.3 MATERIALS AND METHODS 140
7.3.1 Subjects 140
7.3.2 Intracranial EEG acquisition 140
7.3.3 Image acquisition 141
7.3.4 Region of interest selection 142
7.3.5 Structural network generation 143
7.3.6 Functional network generation 145
7.3.7 Structure-function coupling analysis 146
7.3.8 Statistical analyses 149
7.4 RESULTS 150
7.4.1 Clinical data 150
7.4.2 SC-FC coupling using broadband functional connectivity 151
7.4.3 Frequency-specific SC-FC analysis 153
7.4.4 SC-FC sub-analysis in focal to bilateral tonic-clonic seizures 155
7.4.5 Virtual edge resection analysis 157
7.5 DISCUSSION 159
7.5.1 Structure-function coupling across time, frequency and space 159
7.5.2 Methodological Considerations and Limitations 163
7.5.3 Conclusions 165
7.6 ACKNOWLEDGEMENTS 165
7.7 SUPPLEMENTARY INFORMATION 166
7.7.1 Supplementary Figures 166
CHAPTER 8: CONCLUSIONS 169
REFERENCES 172

List of Tables

Table 3.1: Atlas validation 18
Table 3.2: Mean and standard deviations of computed volumes 30
Supplementary Table 3.1: Computed MTL volumes and correspondence with reference volumes 45
Table 4.1: Demographic and clinical information 59
Supplementary Table 4.1: Table of volumetric and functional asymmetry values 75
Table 5.1: Behavioral task performance 88
Table 6.1: Clinical and demographic patient information 120
Table 7.1: Patient demographic and clinical information 151

List of Illustrations

Figure 2.1: Intracranial EEG (iEEG) 7
Figure 3.1: Example MTL manual segmentation 17
Figure 3.2: Coronal slices of left MTL in a representative subject 19
Figure 3.3: Network analysis approach 22
Figure 3.4: Mean and standard deviations of volumetric asymmetry indices 31
Figure 3.5: Functional and structural node metrics plotted for each MTL subregion 32
Figure 3.6: Detection of functional and structural modules within MTL connectivity matrices .. 34
Figure 3.7: Relationship between functional and structural connectivity networks 35
Supplementary Figure 3.1: Functional and structural local network metrics and asymmetries 47
Supplementary Figure 3.2: Functional network findings on images with no global signal regression 47
Supplementary Figure 3.3: Structural and functional analyses replicated after replacing manual segmentations with corresponding automated segmentations 48
Supplementary Figure 3.4: Functional binary network findings 49
Supplementary Figure 3.5: Structural binary network findings..... 50
Supplementary Figure 3.6: Dice Similarity Coefficient (DSC) between functional and structural networks 51
Supplementary Figure 3.7: Structural and functional analyses replicated after merging CA2/3 subregions with CA1..... 51
Supplementary Figure 3.8: Structural and functional analyses replicated after removing CA2/3 subregions 52
Figure 4.1: MTL segmentation from randomly chosen healthy adult 61
Figure 4.2: T2-weighted MRI coronal slices and corresponding automated segmentations..... 62
Figure 4.3: MTL volumetric asymmetry analyses..... 66
Figure 4.4: MTL functional asymmetry analyses..... 68
Supplementary Figure 4.1: Individual subject level heat maps 75
Figure 5.1: Stimulus presentation paradigm 83
Figure 5.2: Clinical profiles and electrode placement 87
Figure 5.4: Temporal activation patterns at selected electrodes in left hemisphere subject..... 89
Figure 5.4: Temporal activation patterns at selected electrodes in right hemisphere subject..... 90

Figure 5.5: Proposed model for verbal fluency 102
Supplementary Figure 5.1: Behavioral Task Performance 111
Supplementary Figure 5.2: Temporal progression of high gamma activity patterns 112
Supplementary Figure 5.3: Pooled high gamma activity patterns 113
Supplementary Figure 5.4: Differences between letter and category verbal fluency across time 114
Figure 6.1: Schematic of subject-level iEEG network analysis pipeline 124
Figure 6.2: Patient-level strength selectivity analysis 126
Figure 6.3: Group-level strength selectivity analysis 127
Figure 6.4: Edge-level analysis in relation to resection zone 128
Figure 6.5: Matrix of similarity values between functional networks generated using different frequency bands 129
Figure 7.1: Summary of patient-level SC-FC analysis pipeline 148
Figure 7.2: SC-FC analysis using broadband functional connectivity 152
Figure 7.3: Frequency-specific SC-FC analysis 155
Figure 7.4: Assessment of SC-FC coupling in focal to bilateral tonic-clonic seizures 156
Figure 7.5: Subject-specific virtual edge resection approach 157
Figure 7.6: Relationship between edge contribution and edge length 158
Supplementary Figure 7.1: Distributions of streamline lengths for each subject 166
Supplementary Figure 7.2: Repetition of key SC-FC coupling analyses repeated following distance regression 166
Supplementary Figure 7.3: Per-seizure paired differences in mean *z* values 167
Supplementary Figure 7.4: Temporal dynamics of SC-C correlation 168

Chapter 1: Introduction

Epilepsy is a common neurological disorder affecting over 60 million people worldwide. Over one-third of epilepsy patients experience uncontrolled seizures despite medication; within this group, approximately 80% have localization-related epilepsy and are candidates for surgical removal of the seizure-generating region in the brain. Accurate seizure localization is needed to maximize chances of seizure freedom and minimize memory deficits following surgery. With the recent development of more targeted therapeutic options such as laser ablation [1] and neurostimulation [2], precise localization is becoming increasingly valuable for guiding therapy.

Currently, seizure localization involves extensive analysis of neuroimaging, electrophysiology, and clinical data. Seizure localization is challenging in patients with no identifiable structural lesion on clinical MRI, which may preclude therapy or lead to poor post-surgical outcomes. The gold standard for localization involves implanting and recording from intracranial electroencephalography (iEEG) electrodes for up to several weeks with the intent of capturing seizure activity; however, this procedure is highly invasive, time consuming, expensive, and still not always conclusive. There is a clinical need to establish robust biomarkers for seizure networks while minimizing invasiveness and morbidity to the patient.

The primary goal of this thesis is to harness data derived from structural MRI, resting-state functional MRI, and interictal iEEG to localize seizure networks in drug-

resistant epilepsy patients, with a focus on minimizing invasiveness. Drawing from previous literature in the field of network neuroscience, I employ a graph-theoretical approach to map structural and functional brain networks and identify candidate targets for removal. The overarching hypothesis is that multimodal local network connectivity properties can serve as useful biomarkers for epilepsy and add to a growing repertoire of tools used for seizure localization. This thesis is divided into the following three sections:

Section 1: **Map epileptic networks using high-resolution MRI**.

In this section, I focus on medial temporal lobe epilepsy (TLE), the most common form of localization-related epilepsy [3, 4]. In **Chapter 3**, I employ high-resolution structural and functional 7T MRI and automated imaging segmentation techniques to map the medial temporal lobe (MTL) network architecture and asymmetry in a normative population of healthy adults. In **Chapter 4**, I apply the knowledge and methods gained in Chapter 3 to characterize MTL network abnormalities in TLE. I hypothesize that intra-MTL network asymmetry metrics can serve as useful biomarkers for TLE, particularly in nonlesional cases, in which current imaging-based techniques are unsuccessful.

Section 2: **Map epileptic networks using interictal iEEG**.

iEEG recordings can capture brain signals from epilepsy patients with high spatial and temporal resolution. While the majority of iEEG quantitative analyses focus on ictal data, interictal data can also be valuable in mapping epileptic activity and normal

cognitive activities which may be impacted in epilepsy. To introduce the utility of iEEG in mapping brain function, **Chapter 5** describes the development of an iEEG-based method for subject-specific spatiotemporal mapping of language networks in epilepsy patients. In **Chapter 6**, I explore the utility of interictal iEEG recordings for localizing epileptic networks, using data from patients who underwent surgical resection. By integrating iEEG network analysis with clinical and neuroimaging data, I characterize network connectivity inside and outside of the resected tissue in good and poor outcome patients. I hypothesize that high interictal connectivity within the resection zone is associated with good outcomes. Extracting valuable information from interictal iEEG can ultimately reduce the need for prolonged implant times, thereby reducing patient morbidity.

Section 3: Map epileptic networks by integrating MRI and iEEG data.

In **Chapter 7** I develop a pipeline to facilitate combined analysis of MRI and iEEG data to better understand the relationship between the structural and functional epileptic networks. In order to probe brain connectivity as directly as possible at the highest resolution, I focus on high angular resolution diffusion MRI (HARDI) for structural connectivity and iEEG for functional connectivity. I characterize relationships between these two modalities across time, frequency, and space. I hypothesize that structure-function coupling increases during the progression from preictal to ictal states, as seizures spread along structural pathways.

This multi-pronged approach will pave the way for minimally invasive, patient-specific localization of seizure networks, which can facilitate surgical planning and lead to improved outcomes in drug-resistant epilepsy patients.

Chapter 2: Background

Epilepsy is a neurological disease characterized by recurrent, unprovoked seizures. While the majority of the 60 million people who suffer from this disorder are treated with medications, over one-third are drug-resistant [5]. These patients experience uncontrolled seizures that often lead to deterioration in quality of life, severe neurological and psychiatric morbidity, and up to an eleven-fold increase in mortality rate [6]. Approximately 80% of drug-resistant epilepsies are localization-related, meaning that there is a presumed focus in the brain from which seizures arise [7]. If this focus can be identified, it can serve as the target for invasive therapeutic intervention. The most common such therapy is surgical resection, characterized by removal of gross structural lesions of the brain. New surgical techniques, such as laser thermal ablation and implanted closed-loop neurostimulation, have recently gained popularity and aim to achieve similar seizure-freedom rates with reduced invasiveness.

Seizure localization involves attaining and analyzing data from multiple modalities, including MRI, positron-emission tomography, scalp and intracranial EEG, neuropsychological testing, seizure semiology, and clinical evaluations. In patients with lesions identified on clinical MRI scans, surgical resection can result in seizure freedom rates of up to 80% [9, 10]. In contrast, nonlesional patients with normal MRI scans may not be suitable candidates for surgery due to difficulties in localizing seizure-generating

regions. In nonlesional patients who do undergo surgery, post-surgical outcomes are still substantially worse than in patients with well-defined lesions on MRI [11, 12].

Intracranial EEG can be incredibly valuable for localizing seizures, particularly in nonlesional patients. In this approach, implanted subdural and depth electrodes record brain signals for up to several weeks, with the intent of capturing ictal events and identifying seizure onset regions (**Figure 2.1**). While this process is the gold standard for recording seizures with high spatial resolution, it is plagued with limitations. For example, seizures are provoked during the recording period via medication reduction and sleep deprivation; these provoked seizures may be fundamentally different than patients' stereotypical spontaneous seizures, and could misinform localization attempts. Additionally, prolonged implantation and seizure provocation can lead to patient morbidity and complications such as infection or hemorrhage [12]. Finally, poor spatial coverage, ambiguity in seizure onset locations, and conflicting findings from other modalities can result in seizure onset patterns that are poorly localized, leading to debate among clinicians about candidate resection zones. The ultimate decision of whether to perform surgery, and what to remove, can be largely subjective. Clearly, there is a need for reliable tools to map seizure networks more accurately and objectively while minimizing invasiveness.

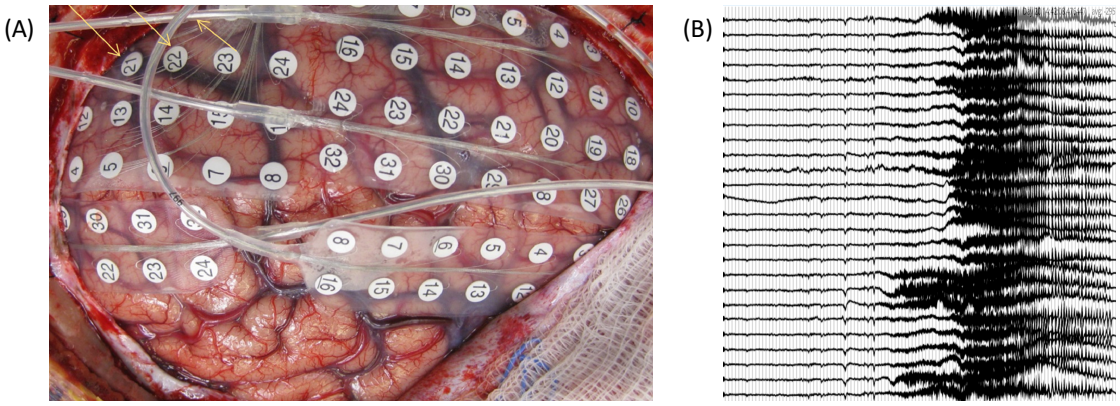

Figure 2.1: Intracranial EEG (iEEG). (A) iEEG electrode placement following craniotomy [13]. (B) Example seizure captured during in-hospital iEEG monitoring.

Recently, it has become evident that epilepsy is a disease of aberrant epileptic networks as opposed to well-defined focal lesions [14, 15]. Therefore, in order to accurately map seizure networks, it is important to identify brain network abnormalities in epilepsy. One approach involves applying methods from graph theory to generate structural and functional networks describing connectivity between pre-defined brain regions; this "network neuroscience" approach has spawned an entire field of research devoted to mapping network changes in various neurological and psychiatric diseases [16, 17]. Structural brain networks can be derived from correlation of MRI-derived morphometric features such as cortical thickness or gray matter volume across subjects [18], or, more directly, from diffusion MRI tractography [19]. Functional networks can be derived from correlations between signal fluctuations recorded through modalities such as resting state functional MRI (fMRI) [20] and intracranial EEG [21–24]. Studies have indicated that key network patterns that manifest during seizures are recapitulated interictally [25, 26],

suggesting that interictal iEEG and/or noninvasive neuroimaging could capture the information needed to localize seizure networks. Yet, most of this work is still far from clinical application, and there remain open questions which now have the potential to be answered given recent advances in neuroimaging modalities and increasing dataset sizes.

This thesis employs novel quantitative methodologies on multimodal high-resolution data to map seizure networks. This work has important implications for our understanding of the structural and functional network topology of epileptic human brains. The long-term goal is to translate this work to clinical practice, allowing for minimally invasive, automated, and optimized seizure localization in drug-resistant epilepsy patients.

Chapter 3: Using high-resolution MRI to map the medial temporal subregional network

In Chapters 3 and 4, I focus on medial temporal lobe epilepsy (TLE), the most common form of localization-related epilepsy [3, 4]. Specifically, I use high-resolution structural and functional MRI to map the subregional network of the medial temporal lobe (MTL), a brain substructure implicated in TLE. In this chapter, I map the MTL connectome in a normative population of healthy adults. These findings can be applied to future studies examining disease-related changes in MTL networks.

Reference: Shah P, Bassett DS, Wisse LEM, Detre JA, Stein JM, Yushkevich PA, Shinohara RT, Pluta JB, Valenciano E, Daffner M, Wolk DA, Elliott MA, Litt B, Davis KA, Das SR. Mapping the structural and functional network architecture of the medial temporal lobe using 7T MRI. *Human Brain Mapping* 39.2 (2018): 851-865.

3.1 Abstract

Medial temporal lobe (MTL) subregions play integral roles in memory function and are differentially affected in various neurological and psychiatric disorders. The ability to structurally and functionally characterize these subregions may be important in understanding MTL physiology and diagnosing diseases involving the MTL. In this study, we characterized network architecture of the MTL in healthy subjects (n=31) using both resting state functional MRI and MTL-focused T2-weighted structural MRI at 7 tesla. Ten MTL subregions per hemisphere, including hippocampal subfields and cortical regions of the parahippocampal gyrus, were segmented for each subject using a multi-atlas algorithm. Both structural covariance matrices from correlations of subregion volumes across subjects, and functional connectivity matrices from correlations between subregion BOLD time series were generated. We found a moderate structural and strong functional inter-hemispheric symmetry. Several bilateral hippocampal subregions (CA1, dentate gyrus, and subiculum) emerged as functional network hubs. We also observed that the structural and functional networks naturally separated into two modules closely corresponding to (1) bilateral hippocampal formations, and (2) bilateral extra-hippocampal structures. Finally, we found a significant correlation in structural and functional connectivity (r=0.25). Our findings represent a comprehensive analysis of network topology of the MTL at the subregion level. We share our data, methods, and findings as a reference for imaging methods and disease-based research.

3.2 Introduction

The medial temporal lobe (MTL) comprises hippocampal subfields and surrounding parahippocampal, perirhinal, and entorhinal cortices. In healthy humans, it serves as the anatomical locus for declarative memory [27] and is a key component of the default mode network [28]. The MTL is also affected in a number of neurological and psychiatric disorders, including Alzheimer's disease, temporal lobe epilepsy, schizophrenia, and depression [29–33].

Prior studies in humans and animal models suggest functional specialization of the various MTL subregions in memory processes, with left and right hemispheres mediating verbal and nonverbal memory, respectively [34–37]. For example, the dentate gyrus plays a role in pattern separation [38], CA3 in pattern completion [Neunuebel and Knierim, 2014], CA1 in place memory and autobiographical memory retrieval [39,40], and entorhinal cortex in hippocampal-neocortical communication [41]. Evidence from a range of modalities indicates that there are spatially non-uniform structural and functional changes in the MTL in neurological diseases. While many of these studies derive from neuroanatomical and neurophysiological data, more recent work uses noninvasive *in vivo* neuroimaging. For example, MRI and PET studies in Alzheimer's disease show hypometabolism of the entorhinal cortex [31,42,43], volumetric atrophy of entorhinal cortex, subiculum, CA1, and the CA1-2 transition zones [29], and atrophy localized to CA1 in early disease [44]. The cortical thickness of Brodmann area 35 (a component of the perirhinal cortex) also discriminates between preclinical Alzheimer's disease and

normal aging [45]. Semantic dementia patients exhibit hippocampal subfield atrophy, most prominently in the left hemisphere [La Joie et al., 2013]. Patients with unilateral mesial temporal sclerosis and temporal lobe epilepsy demonstrate hippocampal subfield atrophy [30] and decreased functional activation in several hippocampal subfields during memory encoding, ipsilateral to seizure focus [46]. MTL subregions are also implicated in psychiatric disorders where findings include volume loss in CA3/dentate gyrus subfields in post-traumatic stress disorder [47], hippocampal atrophy and shape deformations localized to the subiculum in depression [33,48,49], and selective CA1 hypermetabolism in schizophrenia [32].

Neuroanatomical studies elucidate intra-MTL circuitry as a complex network of structural connections promoting information transfer [41]. A growing body of research from the field of network neuroscience highlights the importance of characterizing brain connectivity, though predominantly at the scale of a whole brain connectome. This network neuroscience approach involves applying methods from graph theory to describe functional and/or structural connectivity between pre-defined brain regions [16,17,50]. Application of this approach reveals that whole-brain network architecture is modulated during cognitive effort [51–54], and disrupted in various neurological and psychiatric diseases impacting cognition [55–59]. In addition to whole-brain networks, several studies suggest that network features within particular subregions of the brain can serve as useful biomarkers for neurological function and dysfunction [60–62], and may also reflect changes in larger-scale brain patterns of functioning and behavior [63,64]. This

prior work lends evidence to the notion that characterizing the intra-MTL network via non-invasive neuroimaging can lead to a better understanding of MTL physiology and provide a baseline for studies of neurological diseases involving the MTL.

Functional networks in neuroimaging data are typically derived from resting state blood oxygenation level dependent (BOLD) functional MRI (fMRI) time series that show spontaneous, low-frequency signal fluctuations [65]. Structural brain networks can be derived from across-subject covariance of MRI-derived morphometric features such as cortical thickness or grey matter volume [18,66]. These networks display some correspondence with known anatomical networks, perhaps because brain regions that strongly covary in size across subjects may experience common trophic influences [67–70]. Whole-brain functional and structural networks are correlated but also provide complementary information; for example, functional connectivity has been observed between regions with minimal structural connectivity, suggesting that functional connectivity can be mediated by indirect structural connections [19,71–74].

The primary goal of this study was to exploit recent developments in high-resolution MRI and automated segmentation algorithms to investigate the network architecture of the MTL. Specifically, we carried out a multi-atlas segmentation approach to identify MTL subregions in healthy adults, using sub-millimeter 7 tesla (7T) T2-weighted MRI data tailored for MTL subregion visualization, and used graph theoretic methods to characterize both structural and functional MTL subregion networks. We sought to address several key questions. Firstly, to what extent are the

structure and function of the MTL symmetric across hemispheres? Elucidating MTL symmetry in a normative population would be particularly useful to establish a baseline for future studies, given the existence of hemispheric lateralization of memory function and the possibility of unilateral MTL deficits in neurological diseases, most apparently temporal lobe epilepsy and semantic dementia. Secondly, which MTL subregions serve as network hubs that might facilitate information transfer within network? Thirdly, what is the modular organization of the MTL subregion network? And finally, what is the interplay between structure and function within the network? Our findings represent a comprehensive *in vivo* analysis of intra-MTL network topology in healthy subjects at the subregion level, and can serve as the basis for better understanding its physiological function in both health and disease.

3.3 Methods

3.3.1 Subjects

We recruited 31 healthy adult subjects (mean age = 30.9, standard deviation 10.2, 16 female) with no history of neurological or psychiatric disorders. All studies were conducted under an approved Institutional Review Board protocol of the University of Pennsylvania. We additionally recruited 4 adults with temporal lobe epilepsy and 3 adults with mild cognitive impairment for our atlas set of manually segmented structural MRI images to be used for the automated segmentation protocol (see section *3.3.3* for details). The rationale for including subjects with neurological disease is to enhance

usability of our atlas in future studies, with the hypothesis that such a representative atlas will allow for more accurate automated segmentations in both healthy and diseased brains.

3.3.2 Image Acquisition

Whole-brain images were acquired using a 7.0-T whole-body MRI scanner (Siemens Medical Systems) with a 32-channel phased-array head coil (Nova Medical Inc.). For all 31 healthy subjects and additional atlas subjects, we obtained 0.4x0.4x1.0 mm^3 MTL-tailored 7T T2-weighted structural turbo spin-echo MRI (0.4 × 0.4 mm in plane resolution, 1 mm slice thickness, 224 coronal slices, TR = 3000 ms, TE = 388 ms, 6.16 ms echo spacing) with oblique coronal slices oriented perpendicular to the long axis of the hippocampus and 0.8x0.8x0.8 mm^3 T1-weighted MPRAGE (176 axial slices, TR = 2800 ms, TE = 4.4 ms, TI = 1500 ms, flip angle =7°). We also obtained 2 mm^3 isotropic resting state fMRI in a subset of 24 healthy adult subjects (mean age = 31.7, standard deviation 11.2, 14 female), using a gradient-echo echoplanar (EPI) sequence (64 axial slices with 2mm thickness prescribed in the superior-inferior direction starting from the apex of the brain; matrix size = 96x96; FOV = 192mm; TR = 1 s; TE = 23.6 ms; multiband factor = 4; 420 volumes; 7 minutes) and a B0 field-map sequence (TR= 1 s, TE1=3.24 ms, TE2=5.37 ms). This fMRI acquisition led to coverage of the entire cerebrum in all subjects.

3.3.3 MTL Segmentation

To generate MTL segmentations for our dataset, we used the multi-atlas automated segmentation pipeline "Automated Segmentation of Hippocampal Subfields (ASHS) algorithm" [75], which employs joint label fusion [76] and corrective learning [77] to automatically segment a target image based on a set of manually labeled atlas images. To allow for automated segmentation of our data, we first acquired our own atlas set of 19 subjects: 12 healthy adults (a subset of our 31 healthy adult dataset), 4 temporal lobe epilepsy patients, and 3 subjects with mild cognitive impairment. Structural MRI was acquired in these subjects using the protocol described in section 3.3.2.

Manual segmentation of the MTL in these 19 subjects was carried out in ITK-SNAP [78] by a trained segmentation expert, using a protocol adapted from the ASHS 3T MRI study [75]. The protocol defines MTL subregion boundaries based on a combination of image intensity features and geometric rules using the oblique coronal slices of the T2-weighted images. As illustrated in **Figure 3.1**, we segmented 10 subregions per hemisphere as follows: hippocampal subfields (CA1, CA2, CA3, DG, subiculum, tail) and cortical regions of the parahippocampal gyrus (entorhinal cortex, parahippocampal cortex, and perirhinal cortex divided into BA35 and BA36). The hilus (also sometimes called CA4 or included in CA3) was incorporated in the DG label, and the tail region was composed of the posterior-most aspects of the hippocampus in which individual subfields cannot be discriminated.

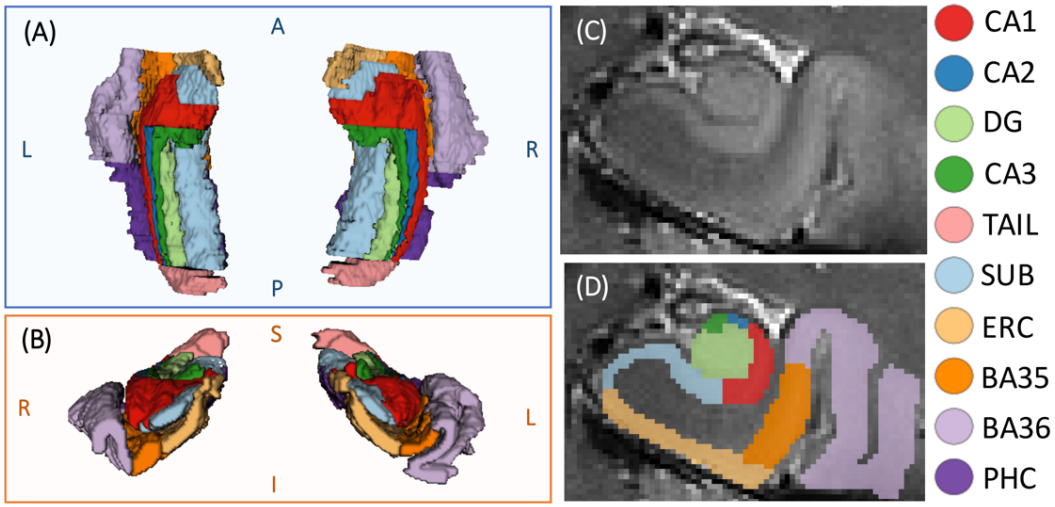

Figure 3.1: Example MTL manual segmentation: (A) superior and (B) anterior 3D views, (C) coronal T2 slice with (D) overlying segmentation. *DG = dentate gyrus, SUB = subiculum, ERC = entorhinal cortex, BA35+BA36 = Brodmann areas 35 & 36 (perirhinal cortex), PHC = parahippocampal cortex.*

To evaluate the efficacy of the atlas, we used a leave-one-out approach to generate automated segmentations for each subject in the atlas. We then assessed for the degree of overlap between the automated and manual segmentations for each subject by computing the Dice Similarity Coefficient (DSC). DSC ranges from 0 to 1 and is computed as follows:

$$DSC(A,B) = \frac{2\,|A \cap B|}{|A|+|B|}, \qquad \textit{(Eq.3.1)}$$

where A and B are, in our case, binary image segmentations. We computed mean DSCs between automated and manual segmentations in our atlas for each individual subregion. The computed DSCs were good across all subregions (range 0.61-0.83) (**Table 3.1**).

	DSC (Auto vs. Manual)	
	Left	**Right**
CA1	0.79 ± 0.04	0.78 ± 0.07
CA2	0.60 ± 0.12	0.62 ± 0.15
CA3	0.62 ± 0.07	0.61 ± 0.09
DG	0.82 ± 0.04	0.83 ± 0.05
Tail	0.78 ± 0.06	0.78 ± 0.07
Sub	0.80 ± 0.02	0.78 ± 0.03
ERC	0.77 ± 0.04	0.76 ± 0.03
BA35	0.66 ± 0.07	0.65 ± 0.07
BA36	0.71 ± 0.04	0.70 ± 0.08
PHC	0.75 ± 0.06	0.75 ± 0.09

Table 3.1: Atlas validation: Dice Similarity coefficients (mean +/- SD) characterizing overlap between automated and manual segmentation for each subregion in the MTL atlas.

While all subregions had a mean DSC>0.6, smaller subregions had lower overlap scores, likely because small, voxel-level shifts between automated and manual segmentations can substantially penalize the DSC in smaller, thinner subregions [79,80]. Perirhinal cortical regions BA35 and BA36 also had slightly lower DSC values, likely due to some ambiguity in the maximal coronal extents of these regions. Our overlaps were comparable to those seen in the prior 3T ASHS MTL atlas (subregion-level DSCs between 0.50 - 0.819) [75] and higher in smaller subregions, perhaps as a result of the higher resolution images. The hippocampal subfield overlaps were also comparable with another recently published hippocampal atlas (DSCs between 0.54 – 0.85) which also used the ASHS protocol on 7T MRI but did not include all regions of the parahippocampal gyrus [80]. For a visual representation of the efficacy of the automated

approach, **Figure 3.2** illustrates the comparison between the manual and automated segmentation for a representative subject.

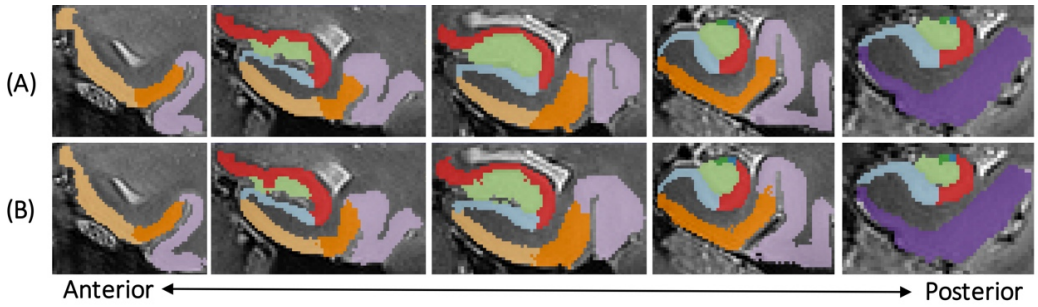

Figure 3.2: Coronal slices of left MTL in a representative subject with (A) manual segmentation and (B) corresponding automated segmentation.

The study atlas was used to generate automated MTL segmentations of the 31 T2-weighted images in our healthy adult dataset. We qualitatively assessed all resulting automated segmentations via visual inspection (by authors P.S., L.W.). The resulting segmented MTL subregions were used as regions of interest for all subsequent analysis, though for the 12 healthy adult subjects which were also in the atlas set, we used the manual rather than automated segmentations to maximize segmentation accuracy.

3.3.4. MTL Volumetry

We first computed MTL subregion volumes to compare findings to prior studies and to relate our network findings to underlying volumetry. We calculated volumes and volumetric asymmetry indices *(Right – Left / Right + Left)* for each of the 10 subregions, as well as for the entire hippocampus and entire MTL.

3.3.5 Functional and Structural Network Generation

We carried out several processing steps on the raw fMRI time series data. First, B0 maps were used to correct EPI distortion. Next, six-parameter rigid body motion correction was implemented to account for head motion-related artifacts [81]. All included subjects experienced minimal head motion (< 1mm translation and < 0.5^{o} rotation in any direction) at all times during acquisition. Following motion correction, the fMRI data were co-registered to the high-resolution structural MRI space (using rigid-body transformation and a mutual information cost function), as there is evidence that analyzing functional MRI data in higher resolution anatomical space improves spatial precision and reproducibility of measurements [82]. To reduce low-frequency drift and high-frequency noise [65,83], the fMRI data were temporally band-pass filtered in the range of 0.008 - 0.08 Hz. Physiological noise was eliminated via linear regression to factor out the global signal and mean signals from white matter and cerebrospinal fluid regions [83]. The Atropos method [84] was used for three-tissue segmentation. We also regressed out the six parameters of head motion (obtained from motion correction) and their six temporal derivatives to minimize motion-induced signal variation [85,86]. To minimize mixing of BOLD signal between neighboring subregions, we did not apply any spatial smoothing, as is common in high-resolution fMRI studies [46,87]. Linear Pearson correlations between the average residual time-series signals for each MTL subregion were used to generate functional connectivity matrices for each subject [88]. The

matrices were Fisher *r-z* transformed for variance stabilization [89] and then averaged across subjects to generate a group-level functional connectivity matrix.

We carried out several extra processing steps on the volumetric data. First, consistent with the procedures in Yushkevich et al. (2015), we normalized the volumes of the extrahippocampal cortical regions (ERC, BA35&36, and PHC) by their the anterior-posterior extents as follows:

$$[\text{normalized volume}] = \frac{[\text{volume}]}{[\text{extent in slices}] \times [\text{slice thickness}]} . \qquad \textit{(Eq. 3.2)}$$

Since the anterior-posterior slice boundaries of these regions were defined relative to the hippocampal head, this normalization step ensures that the volumes are not confounded by hippocampal head length. Additionally, we adjusted each subregion volume by total intracranial volume via linear regression, motivated by a prior study demonstrating that normalizing regional volumes by intracranial volume is necessary to accurately characterize the extent of disease-driven regional atrophy [90], and consistent with other studies [30,75]. We generated a group-level structural covariance matrix using the Pearson correlations between these normalized MTL subregion volumes across subjects, as Pearson correlation between regional grey matter volumes has been found to be a useful measure of structural connectivity in prior studies [91,92]. Similar to the functional networks, the matrix was then Fisher *r-z* transformed.

Matrices were kept fully weighted, as there is evidence that connection strength carries important information about network architecture [93] and that weak connections show potential as disease biomarkers [55]. In both the functional and structural networks,

the matrices represent graphs in which subregions serve as nodes and the strength of correlation between pairs of subregions serve as edge weights. The procedure for generating both functional and structural networks from the MTL subregions is summarized in **Figure 3.3.**

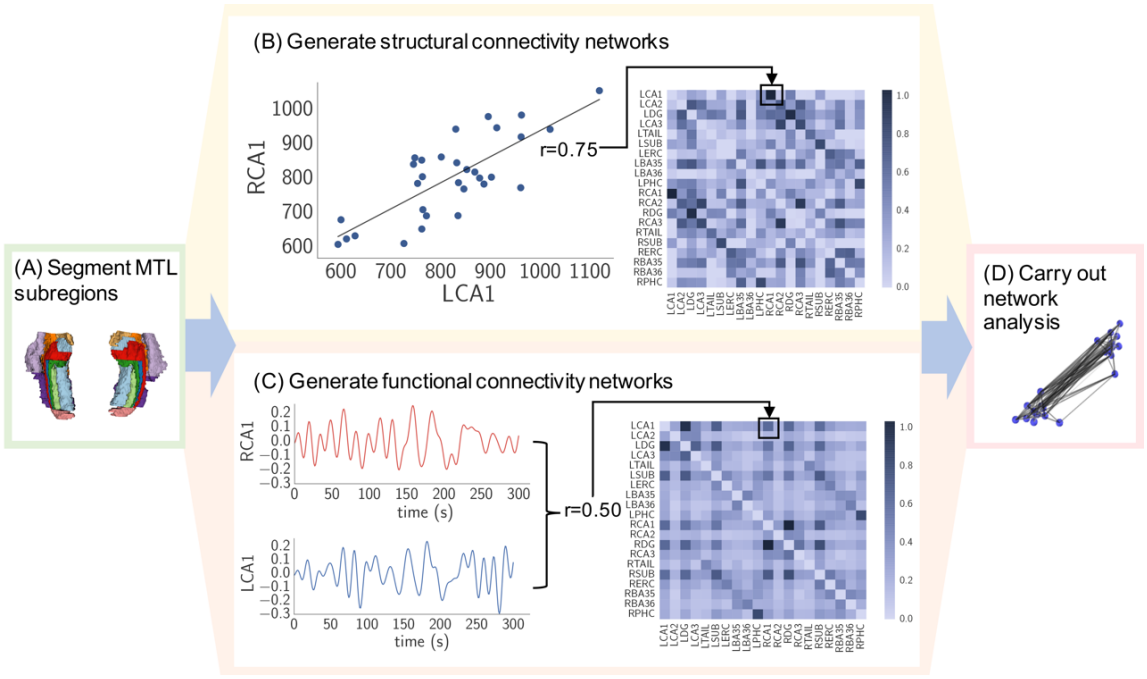

Figure 3.3: Network analysis approach: (A) MTL subregions were segmented. (B) Elements of the structural covariance matrix were equivalent to Pearson correlations between normalized MTL subregion grey matter volume pairs across subjects (each data point in the displayed plot represents one subject). (C) Elements of the subject-specific functional connectivity matrices were equivalent to Pearson correlations of residual time series between MTL subregion pairs (these matrices were then averaged across subjects). (D) Matrices were further processed via Fisher *r*-*z* transformation and analyzed using various graph-theoretic measures.

3.3.6 Functional and Structural Network Analysis

3.3.6.1 Network Symmetry and Hubness

As described in section 3.3.5, we characterized the MTL networks as graphs, which contain nodes and edges. Such graphs can contain heterogeneous structure that is important for the system's function. While a number of graph statistics have been defined to understand this heterogeneous structure, many of them are correlated with one another, especially in brain networks [94,95]. It is useful to choose a set of graph statistics that describe important dimensions of variation in brain networks but are not necessarily redundant. Historically, measures that have proven particularly useful in characterizing brain graphs include the connectivity strength, clustering coefficient, and efficiency [17], largely due to their sensitivity to the markers of small-world architecture [93]. We therefore computed local connectivity strength, clustering coefficient, and efficiency for both group-level structural covariance and functional networks. Since the most widely-applied definitions for these metrics require non-negative edge weights [96], and since the meaning of negative correlations is debatable and not well understood [97–99], we set negative edge weights to zero. The percentage of connections surviving this threshold was 85.3% of edges in the group structural network and 96.8% in the group functional network. We define the network metrics below.

Connectivity Strength: The local connectivity strength $k(i)$ at node i for a weighted network with a set of nodes, N, is the sum of the weights of all connections to node i as follows:

$$k_i = \frac{1}{N}\sum_{j \in N} w_{ij}\ , \qquad \textit{(Eq. 3.3)}$$

where w_{ij} is the edge weight between nodes *i* and *j*.

Clustering Coefficient: The local clustering coefficient *c(i)* at node *i* can be conceptualized as the likelihood that the neighbors of *i* are interconnected. One way in which to quantify this concept for weighted networks is:

$$c_i = \frac{2}{k_i(k-1)}\sum_{j,h \in N}\left(\widetilde{w}_{ij}\widetilde{w}_{ih}\widetilde{w}_{jh}\right)^{1/3}, \qquad \textit{(Eq. 3.4)}$$

where the weights are scaled by the largest weight in the network, i.e. $\widetilde{w}_{ij} = w_{i□}/max(w_{ij})$ [100].

Efficiency: The local efficiency *e(i)* is often thought of as a measure of the capacity of node *i* for information transfer throughout the network [101,102] (although for caveats in this interpretation, see also Rubinov and Bassett, 2011). It can be defined as follows [104]:

$$e_i = \frac{1}{N-1}\sum_{i \neq j \in N}\frac{1}{L_{ij}}, \qquad \textit{(Eq. 3.5)}$$

where L_{ij} is the shortest weighted path length between nodes *i* and *j*, where the length of each edge is the reciprocal of the edge weight, $1/w_{ij}$.

To characterize the network symmetry, we computed the Pearson correlation coefficient between the network metrics for left and right hemispheres, as well as the asymmetry indices *(Right – Left / Right + Left)* for each subregion for each of the three network metrics. To summarize the degree of asymmetry in the network, we also defined

a network asymmetry index ν as the mean of the absolute value of the asymmetry indices across all subregions and across all three network metrics as follows:

$$\nu = \frac{1}{3*N} \sum_{i=1}^{N/2} \left|\frac{k_{i+N/2} - k_i}{k_{i+N/2} + k_i}\right| + \left|\frac{c_{i+N/2} - c_i}{c_{i+N/2} + c_i}\right| + \left|\frac{e_{i+N/2} - e_i}{e_{i+N/2} + e_i}\right|, \qquad \textit{(Eq. 3.6)}$$

where the first *N/2* nodes correspond to the left MTL subregions and the last *N/2* nodes correspond to the analogous right MTL subregions. Like a standard asymmetry index, ν can range from 0 to 1.

We also used the local network metrics to identify network hubs that might serve as key facilitators of information transfer. Although there is no one agreed upon definition of a network hub [105], it has been suggested that aggregating rankings across multiple network metrics is a robust approach to defining a hub [106]. We wanted to identify subregions with relatively high strength, clustering, and efficiency. Since the distributions of metric values were non-Gaussian, we defined a network hub to be any subregion that had a local network metric value at least 25% higher than the median value across subregions, for all three computed metrics (strength, clustering, and efficiency).

3.3.6.2 Modular Organization Assessed by Community Detection

While the previous analysis focused on node-level network analysis, additional characterization of global network topology was needed to highlight the relationships between the MTL subregions. Therefore, we characterized modular organization, which is a network property that has previously been shown in whole-brain studies to vary

across development and in neurological diseases [107–109]. Modules represent "communities" within networks [110,111]: subsets of nodes that are more strongly connected among themselves than they are to nodes in other modules. To quantify the degree to which a network can be partitioned into modules, one can define a modularity quality function as follows (Newman, 2004):

$$Q_0 = \sum_{i \neq j \in N}(A_{ij} - \gamma P_{ij})\delta(g_i, g_j), \qquad \textit{(Eq.3.7)}$$

where A_{ij} is the weighted adjacency matrix, $\delta(g_i, g_j) = 1$ if nodes *i* and *j* are in the same module and 0 otherwise, and γ is a resolution parameter (chosen to be 1 as is standard). The element P_{ij} is the expected weight of the edge connecting node *i* to node *j* under the Newman-Girvan null model defined by:

$$P_{ij} = \frac{k_i k_j}{2m}, \qquad \textit{(Eq. 3.8)}$$

where *m* is the total weight of the edges in the matrix. The Louvain algorithm was used to partition the MTL into modules, as this method is computationally efficient and leads to higher modularity values compared with other approaches [114].

3.3.6.3 Structure-Function Correlation

Given prior work suggesting topological isomorphism between whole-brain structural covariance networks and resting-state fMRI networks [66,115], we wanted to determine to what degree this finding is upheld in intra-MTL networks. This information could clarify the degree to which structural and functional connectivity provide complementary vs. equivalent information. The normal structure-function correlation

may also serve as an informative baseline for future studies, as prior whole-brain studies have revealed changes in structure-function relationship during neurological disease [115] and in various cognitive states [116,117]. To directly quantify the relationship between structure and function in the MTL network, we computed the Pearson correlation coefficient between the edges in the group level structural covariance matrix and the group-level functional connectivity matrix. To minimize loss of information, we included anti-correlations (edge weights less than zero) in this analysis. Furthermore, we repeated the analysis using only the 24 subjects who had both structural and functional scans (n=24) to ensure robustness of findings over a common group of subjects.

3.3.7 Statistical Analysis

3.3.7.1 MTL Volumetry

Regions with significant volumetric asymmetry were determined using a one-sample, two-tailed *t*-test, Bonferroni-corrected for multiple comparisons over the 12 regions (10 MTL subregions + entire hippocampus + entire MTL).

3.3.7.2 Network Analysis

To assess the variability of our findings for both functional and structural networks, we carried out a bootstrapping procedure by randomly sampling subjects with replacement. We generated 1000 bootstrapped samples such that each sample had the same number of subjects as the original dataset (n=31 for structural networks, n=24 for functional networks). For each of 1000 bootstrapped samples, we generated a functional

and structural network as described in section *3.3.5*, leading to a set of 1000 functional and 1000 structural bootstrapped matrices. Variability in local network metrics and the network asymmetry measurements was assessed by repeating these computations across the bootstrapped networks. We determined the significance of network symmetry by comparing the computed ν-values to a null distribution of ν-values generated by randomly permuting the network nodes (1000 permutations).

For modularity, we determined the significance of the partitions by comparing the modularity of the partitioned networks with that of random networks generated via random permutation of the network edges (10,000 permutations) [112]. To verify the replicability of the discovered modules, we also assessed modular organization using alternative approaches. First, for both functional and structural networks, we carried out modularity analysis for each of the 1000 bootstrapped matrices. Specifically, we computed the partitions for each of the 1000 bootstrapped matrices and identified a consensus partition [112]. The consensus partition is defined as the partition that is most similar to the rest [118], where similarity is defined as the z-score of the Rand similarity coefficient [119]. Second, for the functional networks, we computed the partitions for each of the subject-specific functional matrices (prior to averaging across subjects) and identified a consensus partition.

Finally, we computed the significance of the structure-function Pearson correlation by comparing the true correlation to a null distribution of correlations generated via random permutation of the network edges (10,000 permutations).

We considered the possibility that subregion size and temporal signal-to-noise ratio (tSNR) could be confounding factors for our functional network findings. Therefore, we assessed the correlation between mean subregion size and mean subregion tSNR with functional node-level metrics to assess the effect of these variables. Significance in these correlations was determined by permuting the nodes of the network (i.e. subregions) to generate a null distribution of correlations (1000 iterations).

3.3.8 Reproducibility Analysis

We carried out additional analyses to evaluate robustness of our findings to modifications in our analysis pipeline. Firstly, we replicated our functional network analyses omitting global signal regression, as this pre-processing step has been a topic of much debate [99]. Secondly, we replicated our entire analysis after replacing any manual segmentations with their corresponding automated segmentations. Thirdly, since investigations of brain connectivity often utilize binary graphs as input, we carried out analogous analyses on binary networks derived using a range of thresholds (see **Supplementary Information** for a detailed description), to enhance interpretability and applicability to future studies. Finally, since the CA2 and CA3 regions are quite small and may have unreliable signal on their own, we repeated analyses after combining them with CA1 to generate a "CA" region, as well as removing them altogether.

3.3.9 Software

Image processing and network analyses used a combination of SPM [120], FSL [121], ANTS [122], the Brain Connectivity Toolbox [96] and custom python scripts.

3.4. Results

3.4.1 MTL Volumetric Analysis

Following atlas validation, we computed MTL subregion volumes (**Table 3.2**) and asymmetry indices (**Figure 3.4**) across our healthy adult dataset. While normative MTL subregion volumes are unknown due to variation in subregion definitions and protocols, our volumes fall within the range of values from various prior neuroimaging and histological studies (**Supplementary Table 3.1**). Our total hippocampal volumes are consistent with those of previous studies, including a meta-analysis which incorporated data from 3,564 subjects [123].

	Computed Volumes (mm^3)	
	Left	**Right**
CA1	821 ± 182	804 ± 160
CA2	26.2 ± 8.70	30.4 ± 11.3
CA3	107 ± 19	88.9 ± 26.3
DG	623 ± 123	740 ± 128
Tail	315 ± 83.0	296 ± 69.9
Sub	837 ± 93.3	853 ± 97.7
ERC	612 ± 85.4	588 ± 81.5
BA35	660 ± 90.0	608 ± 110
BA36	1816 ± 292	1646 ± 235
PHC	1093 ± 225	1047 ± 271
HIPP	2729 ± 347	2812 ± 344
MTL	6911 ± 787	6701 ± 690

Table 3.2: Mean and standard deviations of computed volumes for each MTL subregion, entire hippocampus (CA1-3, DG, Tail, Sub) and entire MTL over the healthy adult dataset.

As expected, most subregions exhibited hemispheric volumetric symmetry; interestingly, we found significant asymmetries ($p < 0.001$) in the dentate gyrus (R > L), CA3 (L > R), and hippocampus (R > L), using a one-sample, two-tailed *t*-test, Bonferroni-corrected for multiple comparisons over the 12 regions.

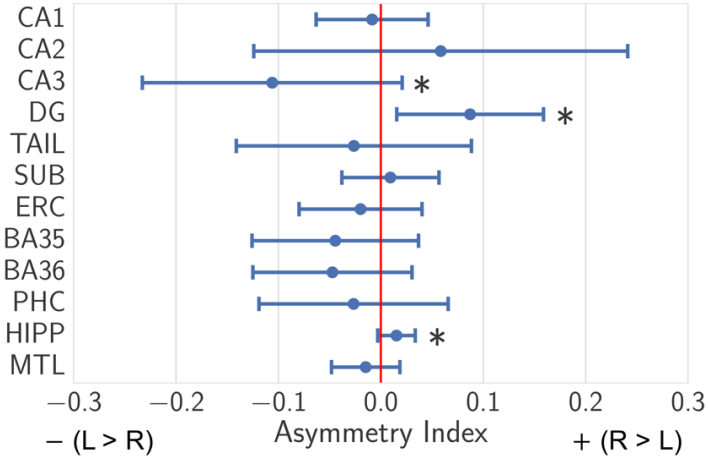

Figure 3.4: Mean and standard deviations of volumetric asymmetry indices *[(Right – Left)/Right + Left)]* for each MTL subregion, entire hippocampus (CA1-3, DG, Tail, Sub) and entire MTL over the healthy adult dataset, *p < 0.001(one-sample, two-tailed t-test, Bonferroni corrected for multiple comparisons over 12 regions).

3.4.2 MTL Network Findings

By relating the three subregion-level functional network metrics (connectivity strength, clustering coefficient, and efficiency) between left and right hemispheres, we found that there is a strong degree of functional MTL symmetry, greater than what would be expected by chance ($r = 0.97$; $\nu = 0.026$, $p < 0.0001$) (**Figure 3.5a**). There is also a moderate degree of structural symmetry, greater than what would be expected by chance ($r = 0.45$-0.67; $\nu = 0.08$, $p = 0.002$), though certain subregions – most notably the dentate

gyrus – exhibit strong structural network asymmetry (**Figure 3.5b**). Mean and standard deviations of individual subregion-level network metric values and asymmetries, based on the bootstrapped matrices, are presented in **Supplementary Figure 3.1**. As shown in **Figure 3.5a**, the bilateral CA1, subiculum, and DG subregions exhibit substantially higher functional connectivity as measured by all 3 metrics, and serve as clear functional network hubs. Using our definition of hubness, no subregions emerge as structural hubs.

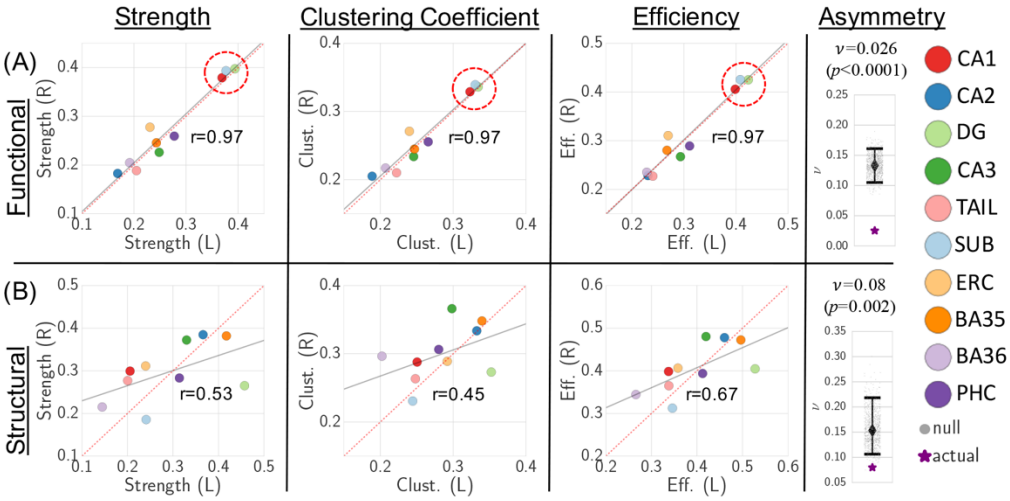

Figure 3.5: Functional (A) and structural (B) local strength, clustering coefficient (clust.), and efficiency (eff.) plotted for each MTL subregion between left (L) and right (R) hemispheres, along with correlation line (grey) and Pearson correlation values. Dotted red y=x line shown for comparison. Functional hubs (bilateral CA1, DG, and subiculum) are highlighted by dotted red circle. Overall network asymmetry (ν) metric is also displayed for functional (A) and structural (B) networks in relation to to null distributions (with associated median and 95% confidence intervals), which demonstrates significantly lower network asymmetry compared with the null distribution (functional permutation $p < 0.001$, structural permutation $p = 0.002$).

After analysis of subregion-level network properties, our next analysis focused on the relationship between subregions via modularity detection. We found that both

functional and structural networks organize into two modules, determined to be significant via permutation testing (structural $p = 0.0006$, functional $p = 0.0241$) (**Figure 3.6**). The functional networks subdivide into one module consisting of bilateral hippocampi and a second module consisting of bilateral parahippocampal regions. The structural networks subdivide into one module consisting of bilateral CA1, DG, subiculum, and tail, and a second module consisting of all remaining regions. Modularity detection and consensus partitioning on the bootstrapped networks yielded the identical functional and structural modules, as did modularity detection and consensus partitioning on the subject-specific functional networks. These results highlight the reproducibility of our findings across a range of approaches for characterizing network modularity.

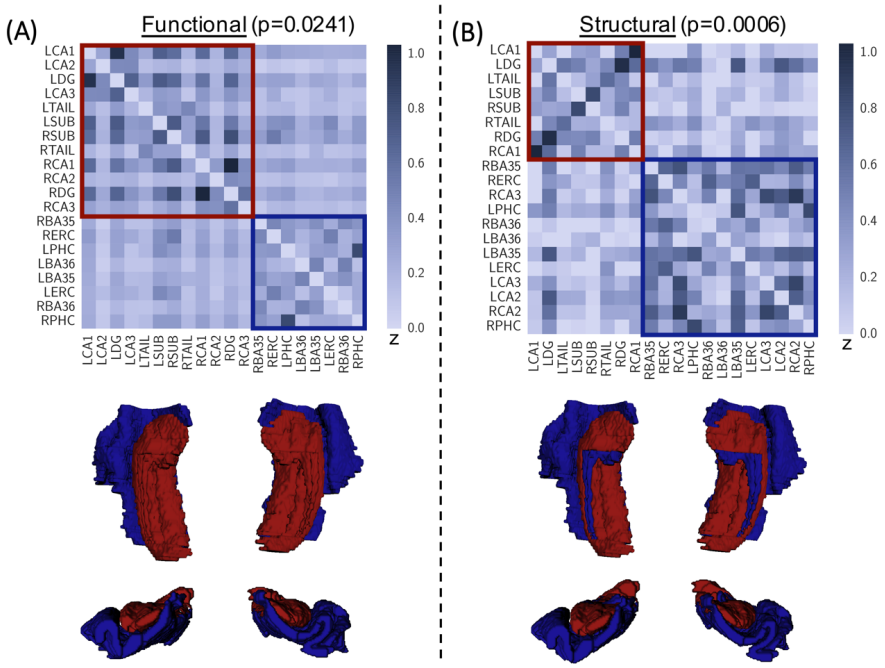

Figure 3.6: Detection of (A) functional and (B) structural modules within MTL connectivity matrices, along with visualization of modules mapped onto MTL segmentation. We find that both networks subdivide into two significant modules (structural p=0.0241, functional p=0.0006, permutation-based testing), one consisting primarily of hippocampal subfields (red) and the second including all extrahippocampal subregions (blue).

Finally, we determined the relationship between function and structure by correlating the edge weights of the structural and mean functional matrices. We found a subtle but significant correlation (r=0.25, p <0.0005 via permutation testing) between the structural and functional networks (**Figure 3.7**). Re-computing the structure-function correlation with only the 24 subjects who had both structural and functional scans (n=24) yielded nearly identical results (r=0.26, p<0.0005).

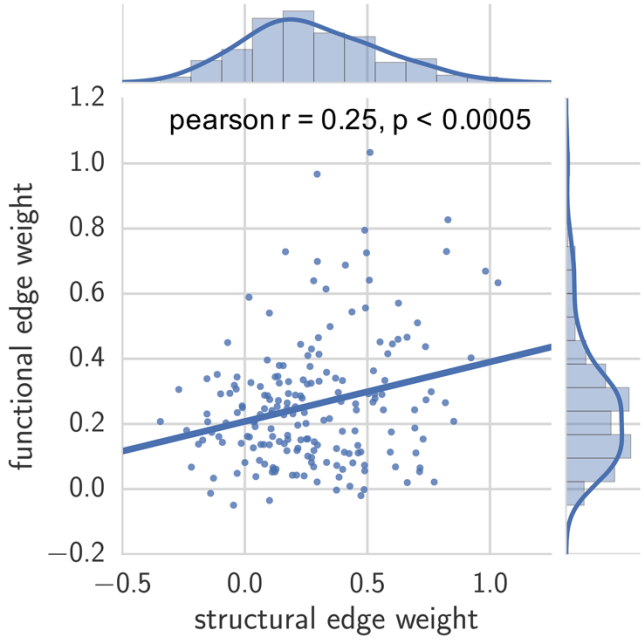

Figure 3.7: Relationship between functional and structural connectivity networks, measured by Pearson correlation of corresponding edge weights in group-level functional and structural networks (Pearson r = 0.25, p < 0.0005, permutation-based testing). Distribution of edge weights are also portrayed.

Overall findings of network symmetry, hubness, modular organization, and structure-function correlation were consistent after replicating analysis with various modifications (omitting global signal regression, utilizing all manual segmentations, carrying out binary network analysis, and removing CA2/3 effects), with only minimal changes in results (**Supplementary Figures 3.2-3.8**). We found no significant correlation between mean subregion size and mean connectivity strength ($r = 0.18$, $p = 0.60$), clustering coefficient ($r = 0.17$, $p = 0.62$), or local efficiency ($r = 0.130$, $p = 0.702$). Similarly, we found no significant correlation between mean subregion tSNR and mean

connectivity strength ($r = 0.19$, $p = 0.59$), clustering coefficient ($r = 0.20$, $p = 0.57$), or local efficiency ($r = 0.20$, $p = 0.59$).

3.5. Discussion

The main goal of this study was to characterize the network architecture of the MTL in healthy adults using high-resolution structural and functional MRI. Using local network metrics, we demonstrated functional and structural inter-hemispheric symmetry, and identified functional and structural network hubs. We also found significant community structure in our networks which revealed inter-hemispheric connectivity and a delineation between hippocampal and extra-hippocampal structures. Finally, we observed a significant correlation in structural and functional network connectivity. Even with a moderate sample size, our findings are robust to variations in processing and analysis steps. Our findings provide an approach to characterizing MTL network structure and function that can be applied to future studies examining disease-related changes in MTL networks.

3.5.1 MTL volumetric and network findings

We found that while functional connectivity was largely symmetric across hemispheres, there was considerably less symmetry in volume and structural connectivity. Structural asymmetry was driven by dentate gyrus and, less substantially, CA3. The volumetric asymmetry in dentate gyrus and CA3 also manifested as asymmetry in structural connectivity, which is likely at least partially due to the fact that volumetric

information was used for structural network construction. Several prior studies have revealed that right hippocampi are subtly larger than left in healthy adults [123–125], though subregion-level asymmetry has not been previously evaluated. Our findings suggest that this asymmetry is primarily localized to the dentate gyrus, though further studies should be carried out on larger datasets to support this finding. Though the underlying mechanism for hippocampal asymmetry is unknown, it may relate to the functional specialization of the hemispheres, as the left and right MTL are associated with verbal and nonverbal memory, respectively [126,127]. While the functional connectivity networks revealed a strong level of functional symmetry during the resting-state, our methodology can be applied to memory task-based data to assess the degree of hemispheric asymmetry based on known functional lateralization.

Our analysis revealed that CA1, DG, and subiculum serve as functional network hubs, suggesting that these subregions facilitate functional integration within the MTL network. Indeed, CA1, DG, and subiculum are implicated in a number of hippocampal pathways, including the mossy fiber pathway (DG → CA3), perforant path (entorhinal cortex → subiculum, DG, CA) and Schaffer collaterals (CA3 → CA1) [31,41,128]. The subiculum also forms a key transition zone between CA1 and the entorhinal cortex [129]. Therefore, our finding of high functional connectivity in these regions is in accordance with existing knowledge of MTL physiology.

Community detection analyses revealed that the functional MTL network subdivides into two modules – one consisting of bilateral hippocampal subfields and the

other consisting of bilateral parahippocampal regions. Since modules exhibit high intra-modular statistical dependence and high inter-modular statistical independence [130], the modular organization suggests a functional segregation of neuronal processing within the MTL. Our finding is supported by a prior fMRI study which found a functional distinction between the hippocampus and adjacent MTL cortices [131]. The structural MTL covariance network subdivided similarly, although surprisingly, bilateral CA2/CA3 fell in the structural module consisting of otherwise parahippocampal structures. Given the relatively high variance and low DSCs of these smallest subregions, this analysis should be confirmed in future studies with larger and/or higher-resolution datasets. Interestingly, we found that the bilateral CA1, DG, and subiculum, which formed a structural module, also were the functional network hubs. This highlights the complementary, yet indirect, relationship between structure and function within the MTL.

Our demonstration of a significant structure-function correlation further suggests that while MTL structure and function are clearly linked, there is also considerable variance between these MTL attributes that warrants further exploration. Our dual structural-functional approach is particularly relevant within the context of several recent studies which reveal that the relationship between whole-brain structural and functional connectivity is implicated in both normal cognition and in disease [58,72,115,117,132–134]. Though a significant correlation in whole-brain structural and functional connectivity is observed in these studies, differences in imaging techniques, parcellation

schemes, and network methods prohibit direct quantitative comparisons in correlation strength.

Previous research in network neuroscience [16] has focused on mapping structural and functional "connectomes" in healthy adults by rigorously characterizing connectivity between regions of the cerebral cortex based on multi-modal neuroimaging [105,135–137]. Such work to establish valid normative data has spawned an entire field of research mapping network changes across variables such as intelligence, gender, and age, as well as in various neurological and psychiatric diseases [57,95,109,138,139]. In the present study we extend this approach to map the MTL connectome, which should lead to new insights into brain-behavior relationships, particularly given the integral role of the MTL in cognition and the increasing availability of high resolution MRI datasets.

3.5.2 Methodological Considerations and Limitations

It is important to note that our measure of structural connectivity is not a measure of direct white matter paths connecting various MTL subregions, but rather a proxy for structural wirings based on covariance in grey matter volumes. While several studies have found robust correlations between structural networks based on covariance of morphometric features and structural networks based on anatomical connections, there is no direct proof that correlations of gray matter volumes across subjects indicate axonal connectivity [18,140]. Therefore, in our model, high structural connectivity between an MTL subregion and its contralateral counterpart does not necessarily support the

presence of a direct interhemispheric anatomical connection. In our case, such an approach is necessary because diffusion tractrography, the primary alternative approach to glean structural connectivity, does not have the resolution to isolate pathways within the MTL. However, recent advances in ultra-high resolution diffusion-weighted imaging [141,142] may allow researchers to employ our methods using diffusion tractography data in future studies.

Another consideration relates to the fMRI data resolution. While most subregions have a substantial average number of voxels in the fMRI space (e.g., CA1: 203, DG:170), the smaller subregions have relatively few voxels (CA2: 7, CA3: 24). Since neighboring voxels in fMRI data are known to be highly correlated, signal from neighboring subregions – particularly the smallest subregions – may be collinear. Our processing pipeline aimed to mitigate this effect by co-registering to the higher-resolution structural MRI space, which has been shown to help maintain the effective resolution of the measured functional activity [82] and is common in high-resolution studies of hippocampal subfields [87,143,144]. We also omitted spatial smoothing to maintain spatial specificity of the measured functional activity and minimize collinearity. Moreover, we regressed out ventricular CSF and white matter to minimize partial volume effects and ensure that the observed signals were not a result of neighboring non-grey matter noise. Finally, we replicated our analysis after removal of CA2 and CA3, and after merging CA2 and CA3 with CA1, to ensure that partial volume effects in these two

regions were not driving our overall findings. Further studies should be carried out on higher resolution fMRI data to confirm our findings related to the smallest subregions.

A related consideration is that functional connectivity networks were generated in this study using a different number of voxels per subregion, since there is inherently a large range of sizes across the 10 MTL subregions. This means that the measurements for smaller subregions are inherently noisier than larger subregions. We decided to keep all voxels rather than eroding the larger regions to more closely approximate the size of smaller regions, in order to minimize effects of biasing results based on the chosen voxels within each subregion. Also, while the small CA2 and CA3 hippocampal subfields had low connectivity strength, so did the larger parahippocampal cortex (PHC) indicating that the correlation strength is not merely a function of subregion size. It may also be possible that central, rounded structures, such as dentate gyrus, may have more reliable signal-to-noise ratio than a more peripheral cortical ribbon-like structure such as PHC. However, we are reassured that subregion size and tSNR are not significant confounds, as they are not significantly correlated with the computed node-level metrics.

A limitation of our 7T atlas set is that we were unable to include intra-rater reliability measurements for validation. However, since our atlas protocol was directly derived from an existing extensively validated 3T protocol, and since MTL subregion DSCs were comparable to those of prior protocols, we believe it is of high reliability. While our atlas yielded high-quality automated segmentations, further studies should be

carried out to optimize atlas composition - such as number and distribution of healthy vs. diseased subjects - for maximal applicability to future investigations.

Several prior fMRI studies reveal differential connectivity patterns along the gradient of the MTL's anterior-posterior axis [145–147]. While our study focused on network connectivity among MTL regions with clear anatomical delineations, further exploration of the intra-MTL subregion connectivity along the anterior-posterior gradient is warranted. Future higher-resolution studies may also allow for the subdivision of the "tail" region into its component subfields to distinguish the detailed neuroanatomy in this region.

3.5.3 Conclusion

We present a comprehensive *in vivo* neuroimaging study characterizing intra-MTL network connectivity in healthy adults by applying graph-theoretical techniques to high-resolution 7T MRI data. This study delineates a methodological approach and provides normative data for a range of future work involving neurological and psychiatric disorders involving the MTL, in which MTL network measures potentially provide insights into disease pathogenesis or serve as biomarkers.

Our network analysis scripts, associated visualizations, and raw data are publicly available at https://github.com/shahpreya/MTLnet.

3.6 Acknowledgments

This work was supported by National Institutes of Health grants T32-EB009384, R03-EB16923-01A1, K23-NS073801-01, 1R01NS099348-02, R01NS085211, R01MH112847, and R01EB017255. We also acknowledge support from the Transdisciplinary Awards Program in Translational Medicine and Therapeutics-Translational Biomedical Imaging Core (TAPITMAT-TBIC) under UL1TR001878, the Center for Biomedical Image Computing and Analytics Seed Award, the Mirowski Family Foundation, and the Thornton Foundation.

3.7 Supplementary Material

3.7.1 Binary Network Analysis

We chose to utilize weighted networks for our primary analysis, as there is evidence that connection strength carries important information about network architecture [93] and that weak connections show potential as disease biomarkers [55]. Though weighted networks may provide richer information, a vast amount of prior and current literature utilizes networks which are binarized using a fixed threshold and then analyzed using various graph-theoretical metrics. With that in mind, we repeated our analysis using binary graphs to facilitate interpretability and applicability of our findings to those of other brain connectivity studies. All code for this analysis is also included in our publicly available repository at https://github.com/shahpreya/MTLnet.

We generated a series of binary networks by thresholding our group-level networks across a range of densities, in 5% increments, in order to retain 1%–50% of all possible edges in the network [104]. For each density, we computed network degree, clustering coefficient, and local efficiency using the commonly accepted binary definitions of these metrics [96]. We computed subregion-level asymmetry indices ([R-L)]/[R+L]) for these metrics, as well as overall network asymmetry. Bootstrapping (sampling subjects with replacement) was used to assess variability of these network metrics. We determined the significance of network asymmetries by permuting the nodes (i.e subregions) of the generated networks (1000 iterations) and generating a null distribution of network asymmetries. Modular organization and modular significance was computed using the same methods as those for the weighted networks. Finally, in order to evaluate the relationship between structural and functional connectivity, we computed the Dice Similarity Coefficient (DSC) to quantify the overlap between the structural and functional adjacency matrices for each density value. The significance of these DSCs was determined by generating a null distribution of DSCs by permuting the edges of the network (1000 iterations).

We found that binary networks exhibited significantly strong symmetry ($p<0.05$) across all density ranges for functional networks (**Supplementary Figure 3.4**), and for densities less than 25% for the structural networks (**Supplementary Figure 3.5**). Moreover, we determined that the modular organization at fixed density thresholds was similar to that observed in the weighted networks, with a strong degree of

interhemispheric connectivity and a segregation of hippocampal and extrahippocampal structures. Finally, the level of overlap between structural and functional networks was significant for most densities up to 30% (**Supplementary Figure 3.6**). While we believe that binary networks are not as robust and representative of underlying physiology as weighted networks, it is still reassuring that our broad conclusions hold up when carrying out analysis on binary networks.

3.7.2 Supplementary Figures

	Computed Volumes (mm^3)		Reference Volumes (mm^3)	
	Left	**Right**	**Histology**	**Imaging**
CA1	821 ± 182	804 ± 160	591^3, 641^4	1420-L*, 1530-R*, 520^2
CA2	26.2 ± 8.70	30.4 ± 11.3	see CA3	60-L*, 71-R*, see CA3
CA3	107 ± 19	88.9 ± 26.3	139^3, 138^4 (CA2+3)	120* (CA3), 179^2 (CA2+3)
DG	623 ± 123	740 ± 128	256^3, 219^4	790-L*, 800-R*, 455^2
Tail	315 ± 83.0	296 ± 69.9	N/A	465^2
Sub	837 ± 93.3	853 ± 97.7	404^3, 850^4	610-L*, 650-R*, 857^2
ERC	612 ± 85.4	588 ± 81.5	N/A	520-L*, 530-R*
BA35	660 ± 90.0	608 ± 110	N/A	see BA36
BA36	1816 ± 292	1646 ± 235	N/A	2585-L^1, 2577-R^1 (BA35+36)
PHC	1093 ± 225	1047 ± 271	N/A	2675-L^5, 2469-R^5

Supplementary Table 3.1: Computed MTL volumes and correspondence with reference volumes from prior histological and neuroimaging studies. *[80], 1. [148], 2. [149], 3. [150], 4. [151], 5. [152]

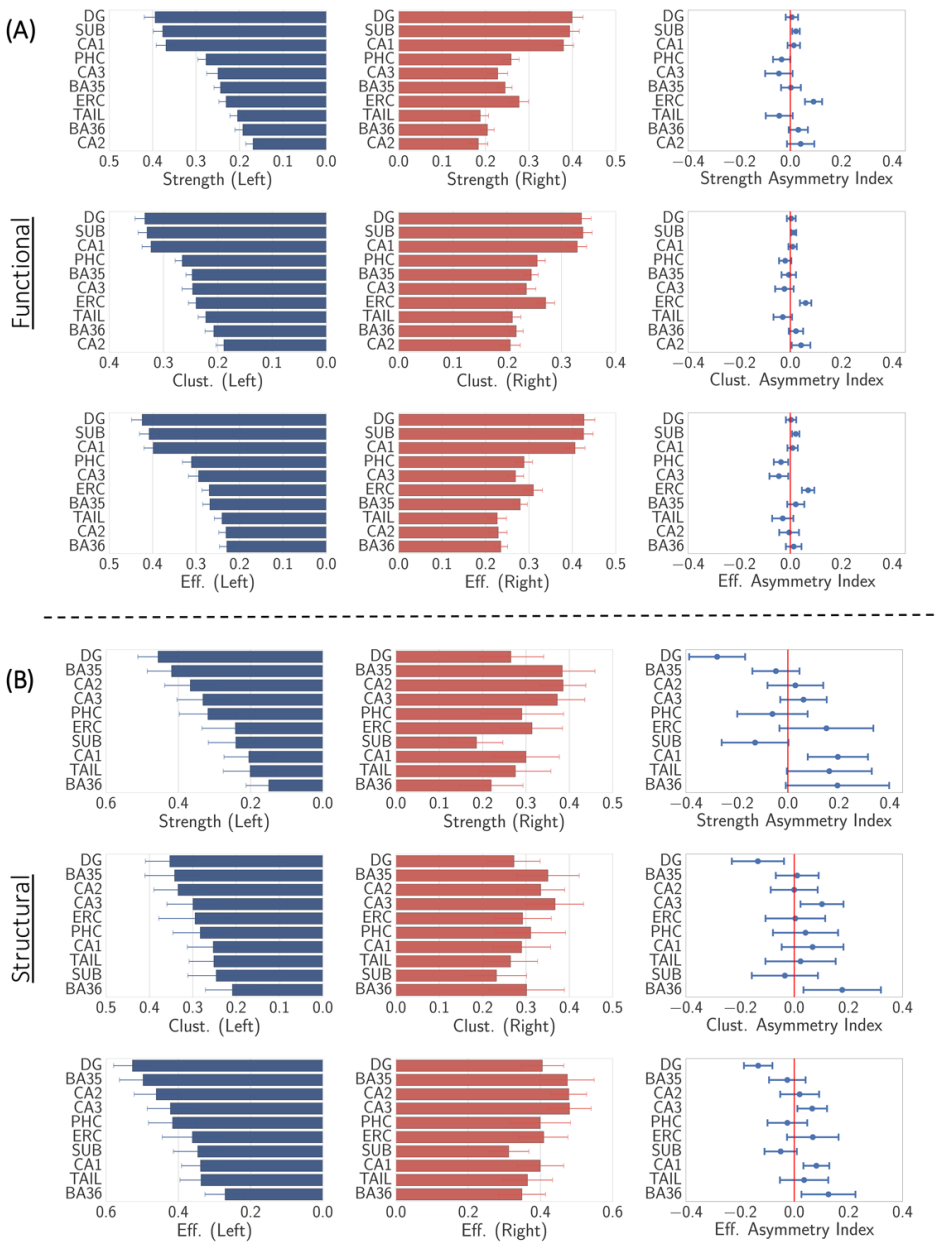

Supplementary Figure 3.1: Functional (A) and structural (B) local network metrics (connectivity strength, clustering coefficient, and local efficiency) computed on bootstrapped matrices for left and right hemispheres (mean +/- S.D.), as well as corresponding asymmetry indices (mean +/- S.D.). For each plot, MTL subregions are rank-ordered based on network metric value for left hemisphere, in order to emphasize hubness of each subregion.

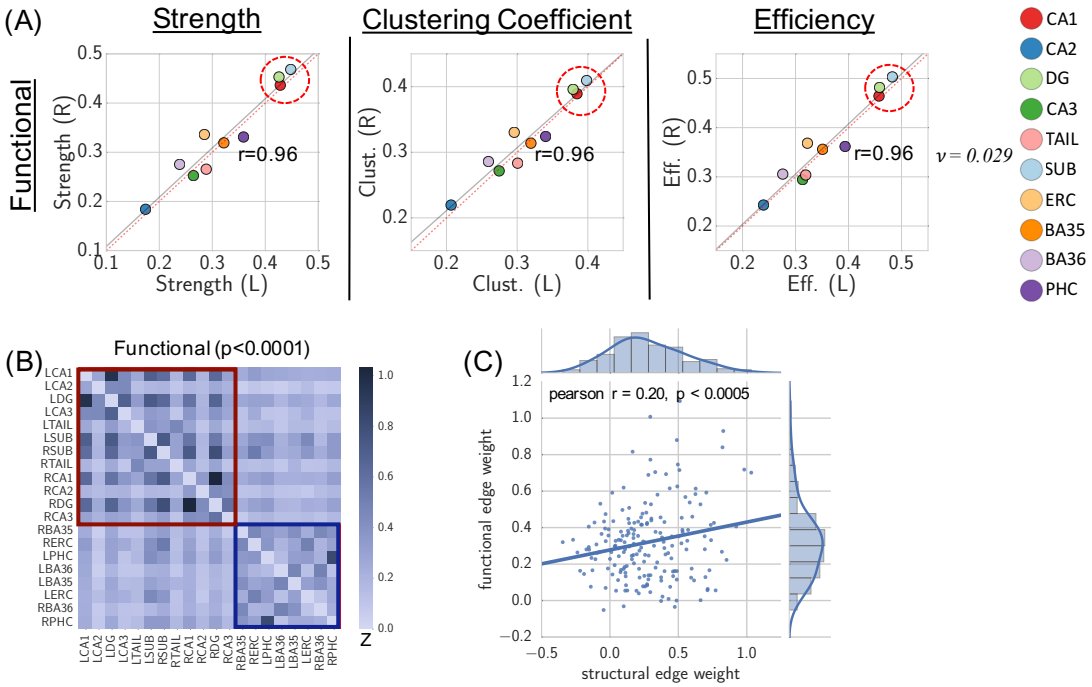

Supplementary Figure 3.2: Functional network findings on images with no global signal regression: (A) functional symmetry across node-level metrics, (B) modular organization, and (C) structure-function correlation. We find significant functional symmetry ($\nu = 0.029$), significant modular organization identical to our original analysis, and significant structure function correlation (r=0.20), revealing that our findings are robust to the choice of global signal regression.

(A)

Subregion	L Vol Mean	L Vol SD	R Vol Mean	R Vol SD
CA1	846.8	174.6	800.5	160.1
CA2	24.78	6.893	29.09	11.08
CA3	109.6	21.49	86.97	25.08
DG	574.5	89.84	735.2	118.6
TAIL	322	80.42	295.2	64.16
SUB	830.5	92.05	866	94.16
ERC	605.3	76.48	601.6	77.89
BA35	650	80.17	591.3	111.1
BA36	1843	269.2	1669	223.2
PHC	1126	207.4	1060	258.5
HIPP	2708	337.4	2813	338
MTL	6932	730.1	6735	661.8

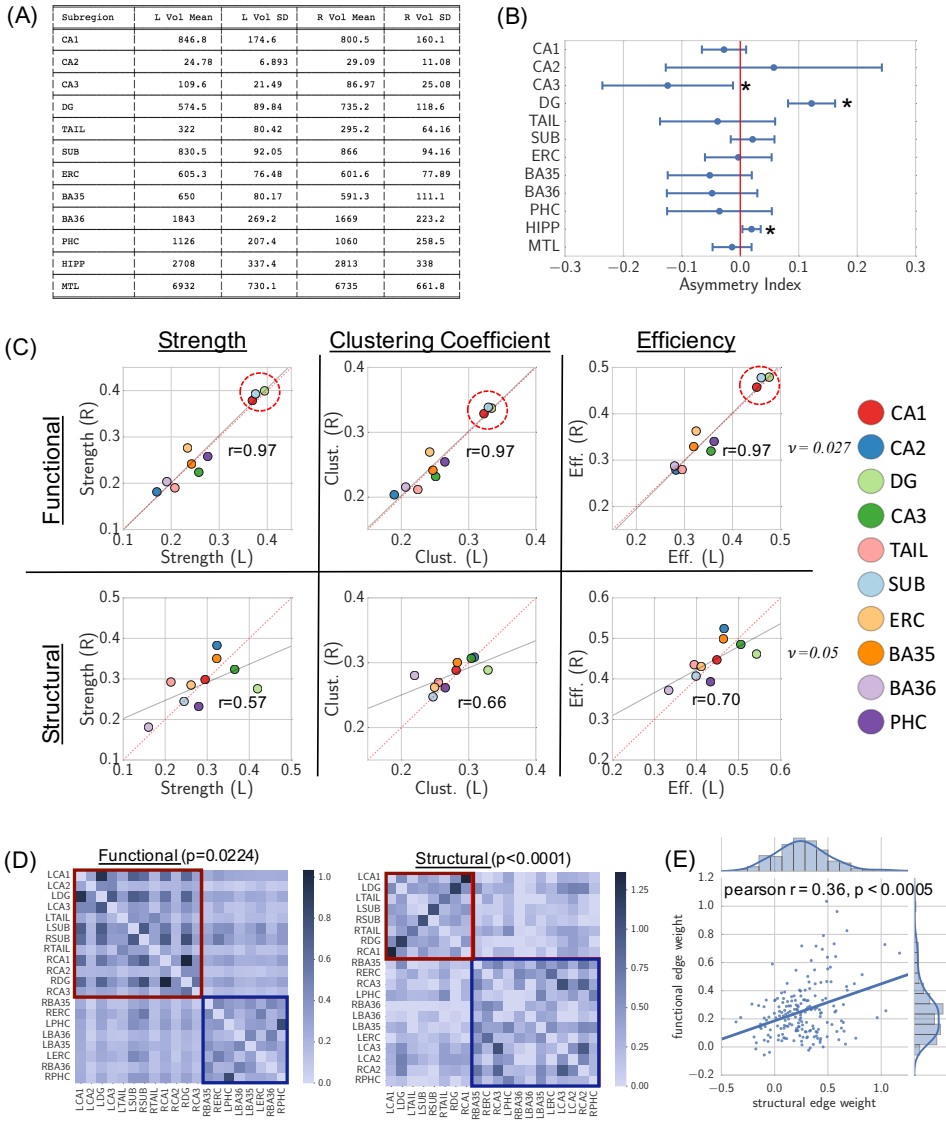

Supplementary Figure 3.3: Structural and functional analyses replicated after replacing manual segmentations with corresponding automated segmentations: (A) subregion volumes, (B) subregional volumetric symmetry, (C) network symmetry, (D) modular organization, and (E) structure-function correlation. Similar to our primary analysis, we find significant volumetric asymmetry in DG, CA3, and hippocampus. Also, we find significant functional symmetry ($\nu = 0.029$), structural symmetry ($\nu = 0.05$), significant functional and structural modular organization identical to our original analysis, and significant structure function correlation (r=0.36), revealing that our findings are robust to the choice of segmentation approach.

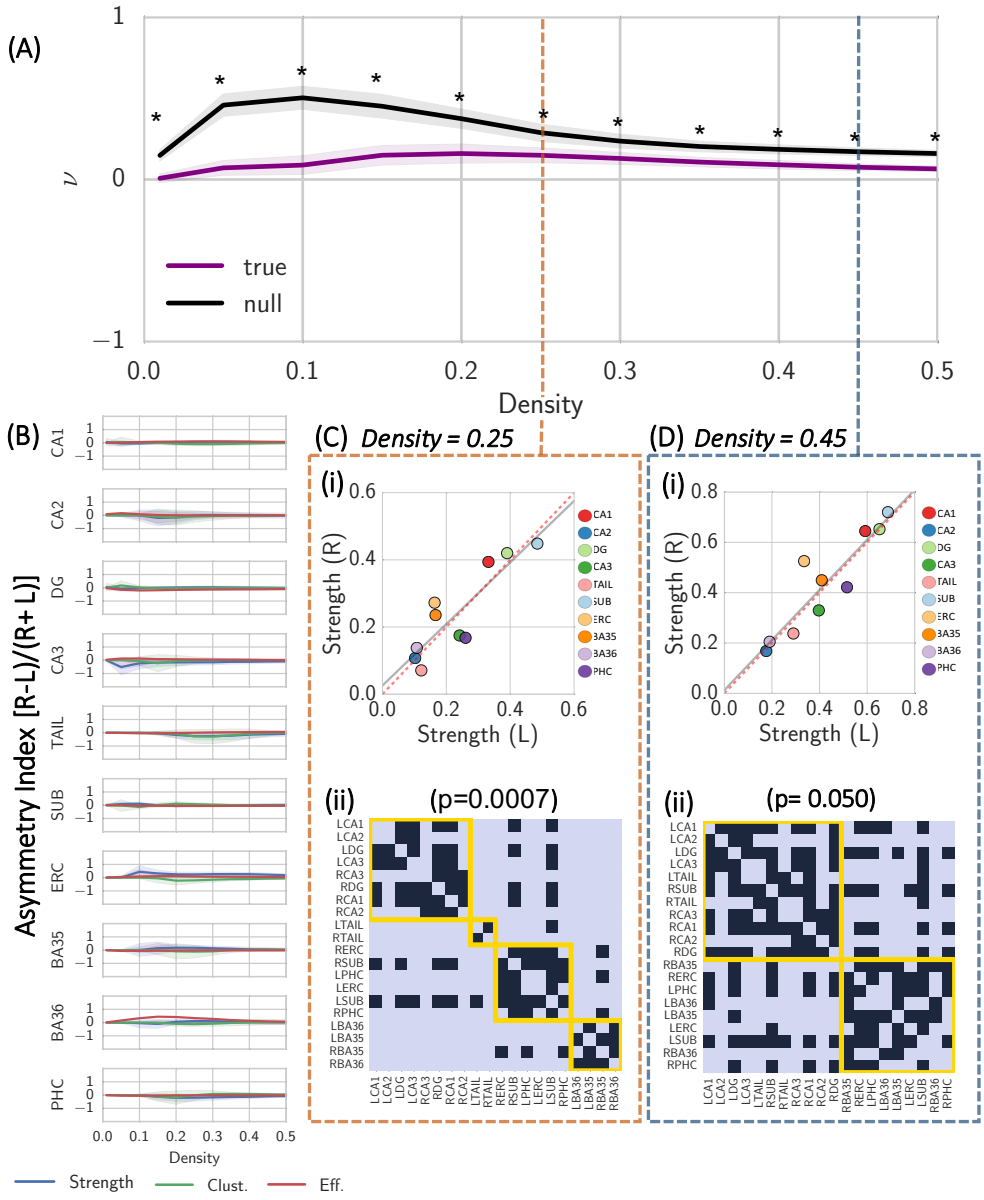

Supplementary Figure 3.4: Functional binary network findings: (A) Network asymmetry across 1%-50% density range compared with null network asymmetry, significant across entire density range (*p < 0.05). (B) subregion level asymmetry indices for connectivity strength, clustering coefficient, and local efficiency. Envelopes represent standard deviation. For two example densities of (C) 25% and (D) 45%, we report (i) left-right correlation in connectivity strength and (ii) modular organization. We find a strong degree of functional symmetry, as well as significant modular organization which emphasizes strong interhemispheric connectivity and a hippocampal-parahippocampal delineation.

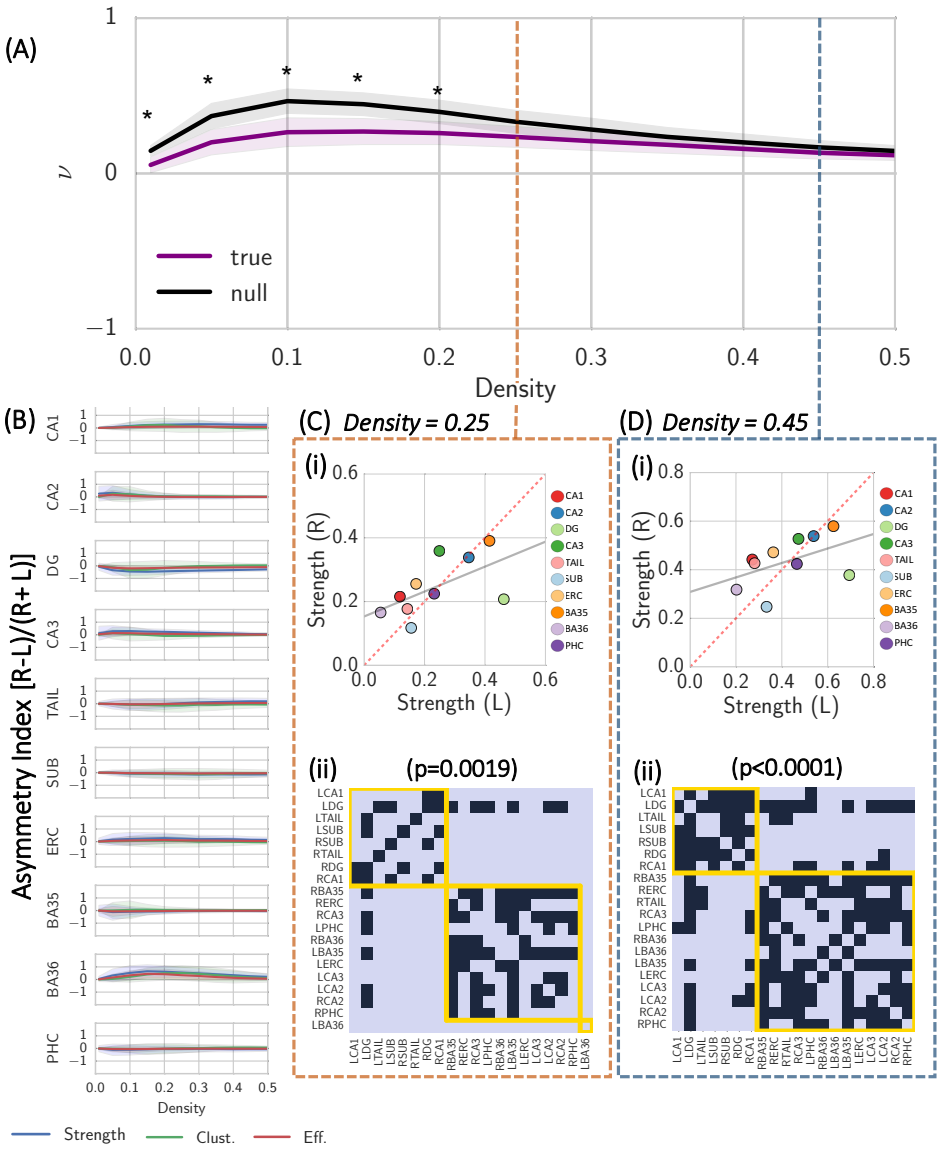

Supplementary Figure 3.5: Structural binary network findings: (A) Network asymmetry across 1%-50% density range compared with null network asymmetry, significant across densities less than 25% (*p < 0.05). (B) subregion level asymmetry indices for connectivity strength, clustering coefficient, and local efficiency. Envelopes represent standard deviation. For two example densities of (C) 25% and (D) 45%, we report (i) left-right correlation in connectivity strength and (ii) modular organization. We find a strong degree of structural symmetry, as well as significant modular organization which emphasizes strong interhemispheric connectivity and a hippocampal-parahippocampal delineation.

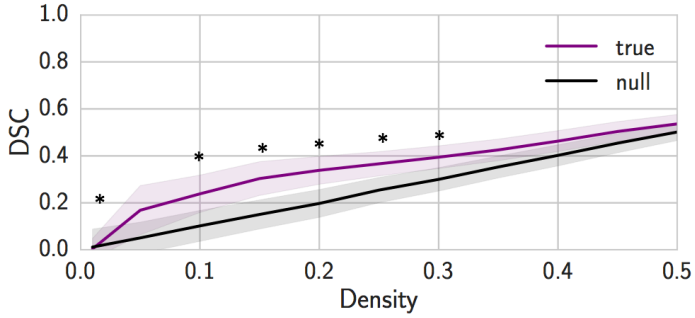

Supplementary Figure 3.6: Dice Similarity Coefficient (DSC) between functional and structural networks, compared with the DSCs expected from a null distribution. Envelopes represent standard deviations. DSC is significantly greater than chance (*p < 0.05) for most thresholds up to 30%.

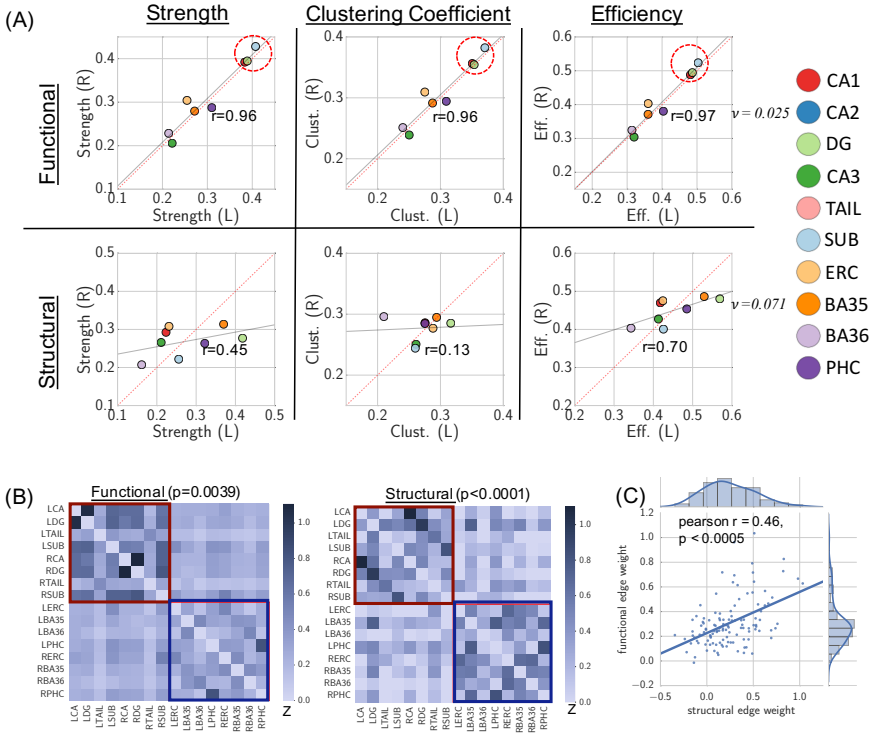

Supplementary Figure 3.7: Structural and functional analyses replicated after merging CA2/3 subregions with CA1: (A) network symmetry, (B) modular organization, and (C) structure-function correlation. We find significant functional symmetry ($\nu = 0.025$), structural symmetry ($\nu = 0.069$), significant modular organization identical to our original analysis, and significant structure function correlation (r=0.47), revealing that our findings are robust to CA2/3 signal.

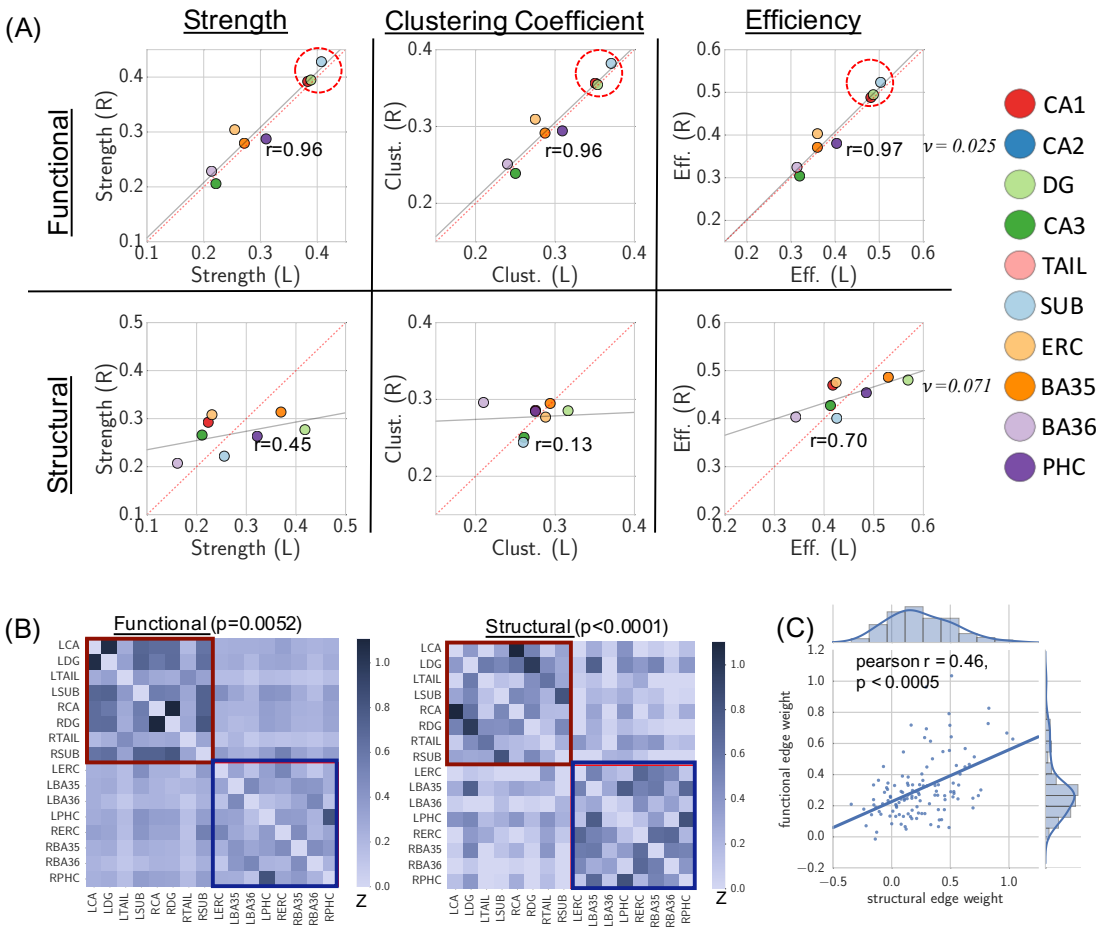

Supplementary Figure 3.8: Structural and functional analyses replicated after removing CA2/3 subregions: (A) network symmetry, (B) modular organization, and (C) structure-function correlation. We find significant functional symmetry ($\nu = 0.025$), structural symmetry ($\nu = 0.071$), significant modular organization identical to our original analysis, and significant structure function correlation (r=0.46), revealing that our findings are robust to CA2/3 signal.

Chapter 4: Using MRI to uncover medial temporal network asymmetry in temporal lobe epilepsy

Now that we have established an understanding of MTL network topology in healthy adults, we can ask: how are these MTL networks disrupted in unilateral mesial temporal lobe epilepsy (TLE)? In this chapter, I apply the knowledge and methods gained in Chapter 3 to characterize MTL network abnormalities in TLE. I demonstrate how MTL functional network-based properties can serve as biomarkers for TLE and distinguish TLE subtypes. Given the asymmetric nature of this disease, I focus on asymmetry-based analyses.

Reference: Shah P, Bassett DS, Wisse LEM, Detre JA, Stein JM, Yushkevich PA, Shinohara RT, Elliott MA, Das SR, Davis KA. Structural and functional asymmetry of medial temporal subregions in unilateral temporal lobe epilepsy: a 7T MRI study. *Under Review* at Human Brain Mapping.

4. 1 Abstract

Mesial temporal lobe epilepsy (TLE) is a common neurological disorder affecting the hippocampus and surrounding medial temporal lobe (MTL). While prior studies have analyzed whole-brain network distortions in TLE patients, the functional network architecture of the MTL at the subregion level has not been examined. In this study, we utilized high-resolution 7T T2-MRI and resting-state BOLD-fMRI to characterize volumetric asymmetry and functional network asymmetry of MTL subregions in unilateral medically-refractory TLE patients and healthy controls. We subdivided the TLE group into mesial temporal sclerosis patients (TLE-MTS) and MRI-negative nonlesional patients (TLE-NL). Using an automated multi-atlas segmentation pipeline, we delineated ten MTL subregions per hemisphere for each subject. As expected, we found significantly different patterns of volumetric asymmetry between the two groups, with TLE-MTS exhibiting volumetric asymmetry corresponding to decreased volumes ipsilaterally in all hippocampal subfields. We also found significantly different patterns of functional network asymmetry in the CA1 subfield and whole hippocampus, with TLE-NL patients exhibiting asymmetry corresponding to increased connectivity ipsilaterally and TLE-MTS patients exhibiting asymmetry corresponding to decreased connectivity ipsilaterally. Our findings provide initial evidence that functional neuroimaging-based network properties within the MTL can distinguish between TLE subtypes. High resolution MRI has potential to improve localization of underlying brain network disruptions in TLE patients who are candidates for surgical resection.

4.2 Introduction

Mesial temporal lobe epilepsy (TLE) is the most common type of localization-related epilepsy, affecting approximately one in 1000 people worldwide [4,153,154]. Approximately 30% of TLE patients do not respond to medical therapy and are candidates for surgical removal of the seizure-generating area [155]. Accurate seizure localization prior to surgery is crucial in order to maximize chances of seizure freedom and minimize post-surgical cognitive deficits. While approximately two-thirds of TLE patients have mesial temporal sclerosis (MTS) identified on structural MRI (TLE-MTS), the remaining one-third have normal-appearing ("nonlesional") clinical MRI scans (TLE-NL). Lateralization and localization of seizure onset zone in these patients can be difficult, since other neuroimaging and electrophysiology-based tests are often inconclusive, precluding surgical resection. In nonlesional patients who do undergo surgery following invasive localization procedures such as intracranial EEG, post-surgical outcomes are still substantially worse than in patients with well-defined lesions on MRI [10,11]. Thus, there remains a pressing clinical need to establish non-invasive neuroimaging biomarkers for nonlesional TLE. Furthermore, with the recent emergence of highly targeted therapeutic options such as laser ablation [1] and neurostimulation [2], precise localization of the seizure onset zone will become increasingly valuable for guiding therapy.

It has become widely accepted that the pathophysiology of localization-related epilepsy extends beyond focal lesions to alter the properties of brain networks

[14,15,139]. As a result, researchers have begun to employ graph theoretical methods to characterize network aberrations in neuroimaging data from TLE patients [156,157]. Many of these studies focus only on TLE-MTS [158,159] or consider TLE as a single entity without distinguishing between TLE-MTS and TLE-NL groups [160–166]. However, there is growing evidence that TLE-MTS and TLE-NL may be distinct disorders with distinct underlying pathophysiology and with different network manifestations [167–171]. These findings suggest that the TLE-MTS and TLE-NL subtypes should be studied separately, to better understand their differences and to promote the discovery of biomarkers specific to TLE-NL.

Most prior work using neuroimaging methods to examine changes in network topology in TLE have focused on whole-brain networks. However, findings from a range of investigative approaches provide initial evidence that network distortions within the MTL itself play a fundamental role in TLE. For example, rodent models of TLE reveal aberrant mossy fiber connections from the granule cell layer to the stratum moleculare of the dentate gyrus (DG); according to the recurrent excitation hypothesis, the resulting DG hyperexcitability may cause seizures [172]. Another example is that histopathology of resected tissue in TLE-MTS patients reveals heterogeneous patterns of atrophy and astrogliosis in the hippocampus and surrounding medial temporal regions [154,172]. From a clinical management standpoint, the extent of resection of various MTL subregions is directly related to seizure control [173]. In fact, 20% of TLE patients with hippocampal resection still experience seizures originating from remaining MTL

structures [174]. These findings suggest that the entire MTL subregional network may be implicated in seizure activity, and that understanding this network could improve diagnosis and treatment.

In this study, we used 7 tesla (7T) MRI to probe fine-grained structure and function within the MTL. Compared to standard clinical MRI, 7T MRI can produce higher resolution images with higher signal-to-noise and contrast-to-noise ratios, facilitating visualization and segmentation of small brain structures with exquisite anatomical detail [175,176]. Moreover, since the first 7T MRI scanner was approved by the U.S. Food and Drug Administration in late 2017, there is a need to develop tools maximizing the clinical utility of 7T data as it becomes more readily available. Building on our previous analyses of intra-MTL subregional connectivity in healthy adults [177], we employed an automated multi-atlas pipeline on sub-millimeter 7T T2-weighted MRI to segment MTL subregions in TLE patients and healthy controls. In addition to subject-specific subregional volumetric analyses, we applied graph theoretical methods to 7T resting-state BOLD-fMRI data to characterize subject-specific functional MTL subregional networks. We focused on asymmetry-based metrics, as structural and functional asymmetry indices have previously been used to aid in seizure lateralization [159,178–183], and are robust to confounds such as age and gender [184,185]. We hypothesized that asymmetry-based metrics would reveal distinct patterns of abnormalities in the TLE-NL and TLE-MTS patients. Our preliminary findings provide

insight into MTL functional connectivity in temporal lobe epilepsy, particularly in cases in which standard clinical MRI is unremarkable.

4.3 Methods

4.3.1 Subjects

We recruited 29 medically-refractory patients with suspected temporal lobe epilepsy undergoing pre-surgical evaluation. To minimize heterogeneity in this diverse patient population, we excluded subjects with the following characteristics: neocortical rather than mesial temporal onset, dual pathology, extra-temporal lesions, bilateral disease or ambiguous laterality, neoplasms, and other neurological co-morbidities. Seizure laterality, mesial temporal origin, and lesional status were determined via a combination of MRI and PET imaging, scalp EEG, intracranial EEG, seizure semiology, and epileptologists' clinical notes, and confirmed by an epileptologist for this study (author K.D.). Our final dataset consisted of 13 patients with unilateral drug-resistant TLE, including 9 TLE-NL and 4 TLE-MTS (**Table 4.1**), along with 24 healthy control subjects [186]. All studies were conducted under an approved Institutional Review Board protocol of the University of Pennsylvania.

LATERALITY	LESIONAL STATUS	GENDER	AGE (y)	AGE at ONSET (y)	DRUG TRIALS
Right	MTS	F	41	5	OXC, PB, PHT, TPX, LTG
Right	MTS	F	55	13	CBZ, GBP, LEV, TPX
Left	NL	M	48	5	GBP, LTG, LEV, PB, PHT, PRE, ZNS
Left	MTS	F	61	1	CBZ, LTG, LCM, LEV, PB, PHT, PRM, TPM, ZNS
Left	NL	F	47	41	CBZ, CLB, CNZ, LTG, LCS, LEV, OXC, PHT, PRE, TPX, ZNS
Left	MTS	F	47	unknown	CLB, GBP, LCM, LEV, OXC, PB, PHT, TIG
Left	NL	F	46	0	PB, OXC, LCM, LTG, LEV, TPX, ZNS
Left	NL	F	56	25	LEV, OXC, LTG, TPX, ZNS, LCM
Left	NL	M	39	36	LEV, LTG, LZP, ZNS
Right	NL	M	36	5	PB, CBZ, VPA, CZP, LTG, LEV
Left	NL	F	32	29	LTG, TPX, ZNS, LEV, OXC
Left	NL	F	37	15	GBP, TPX, LEV, LCM
Left	NL	F	45	24	LTG, ZNS

Table 4.1: Demographic and clinical information for TLE patients included in this study. **Legend:** VPA: valproic acid; ZNS: zonisamide; OXC: oxcarbazepine; CBZ: carbamazepine; CLZ: clonezapam; CZP: clorezepate; LTG: lamotrigine; TPX: topiramate; LEV: leviteracetam; GBP: gabapentin; PB: phenobarbital; PHT: phenytoin; LZP: lorazepam; LCM: lacosamide; PRE: pregabapentin.

4.3.2 Image Acquisition

Whole-brain images were acquired using a 7.0-T whole-body MRI scanner (Siemens Medical Systems) with a 32-channel phased-array head coil (Nova Medical Inc.). For all subjects, we obtained 0.4x0.4x1.0 mm^3 MTL-tailored 7T T2-weighted structural variable-flip angle turbo spin-echo MRI (0.4 × 0.4 mm in plane resolution, 1 mm slice thickness, 224 coronal slices, TR = 3000 ms, TE = 388 ms, 6.16 ms echo

spacing) with oblique coronal slices oriented perpendicular to the long axis of the hippocampus and 0.8x0.8x0.8 mm^3 T1-weighted MPRAGE (176 axial slices, TR = 2800 ms, TE = 4.4 ms, TI = 1500 ms, flip angle = 7°). We also obtained 2 mm^3 isotropic resting state BOLD-fMRI using a multiband, gradient-echo echoplanar (EPI) sequence (64 axial slices, TR = 1 s; TE = 23.6 ms, MB factor = 4, 420 volumes; 7 minutes) and a B0 field-map sequence (TR1= 1 s, TR2 = 100 ms, TE1 = 3.24 ms, TE2 = 5.37 ms).

4.3.3 MTL Segmentation

To generate MTL segmentations for our dataset, we utilized a multi-atlas automated segmentation pipeline derived from the Automated Segmentation of Hippocampal Subfields (ASHS) algorithm [75] as described and validated in our previous work [177]. The atlas dataset included structural MRI acquired with the protocol described in *Section 2.2*, and manual expert segmentations of 10 subregions per hemisphere as follows: hippocampal subfields (CA1, CA2, CA3, DG), hippocampal tail, subiculum, and cortical regions of the parahippocampal gyrus (entorhinal cortex, parahippocampal cortex, and perirhinal cortex divided into BA35 and BA36) (**Figure 4.1**). The hippocampal tail was defined as the most posterior aspect of the hippocampus in which individual subfields could not be discriminated; given the heterogeneity of this region across subjects in terms of size and composition, we excluded it from statistical analyses. We assessed all subjects' images and automated segmentations via rigorous visual inspection to ensure segmentation quality (by authors P.S., L.W.).

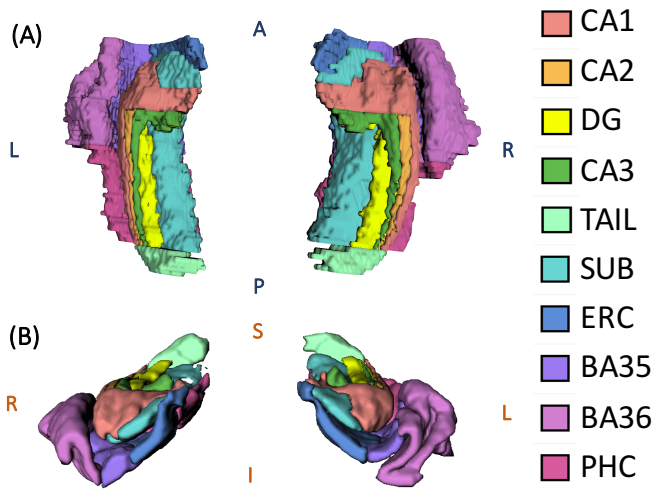

Figure 4.1: MTL segmentation from randomly chosen healthy adult rendered in 3D: (A) superior and (B) anterior 3D views. DG = dentate gyrus, SUB = subiculum, ERC = entorhinal cortex, BA35+BA36 = Brodmann areas 35 & 36 (perirhinal cortex), and PHC = parahippocampal cortex.

Representative segmentations from three subjects – one healthy control, one TLE-NL patient, and one TLE-MTS patient – are shown in **Figure 4.2**. As illustrated, we observed grossly normal MTL architecture in healthy controls and TLE-NL patients including clearly visible hippocampal digitations [187,188], and distortion of hippocampal architecture in TLE-MTS.

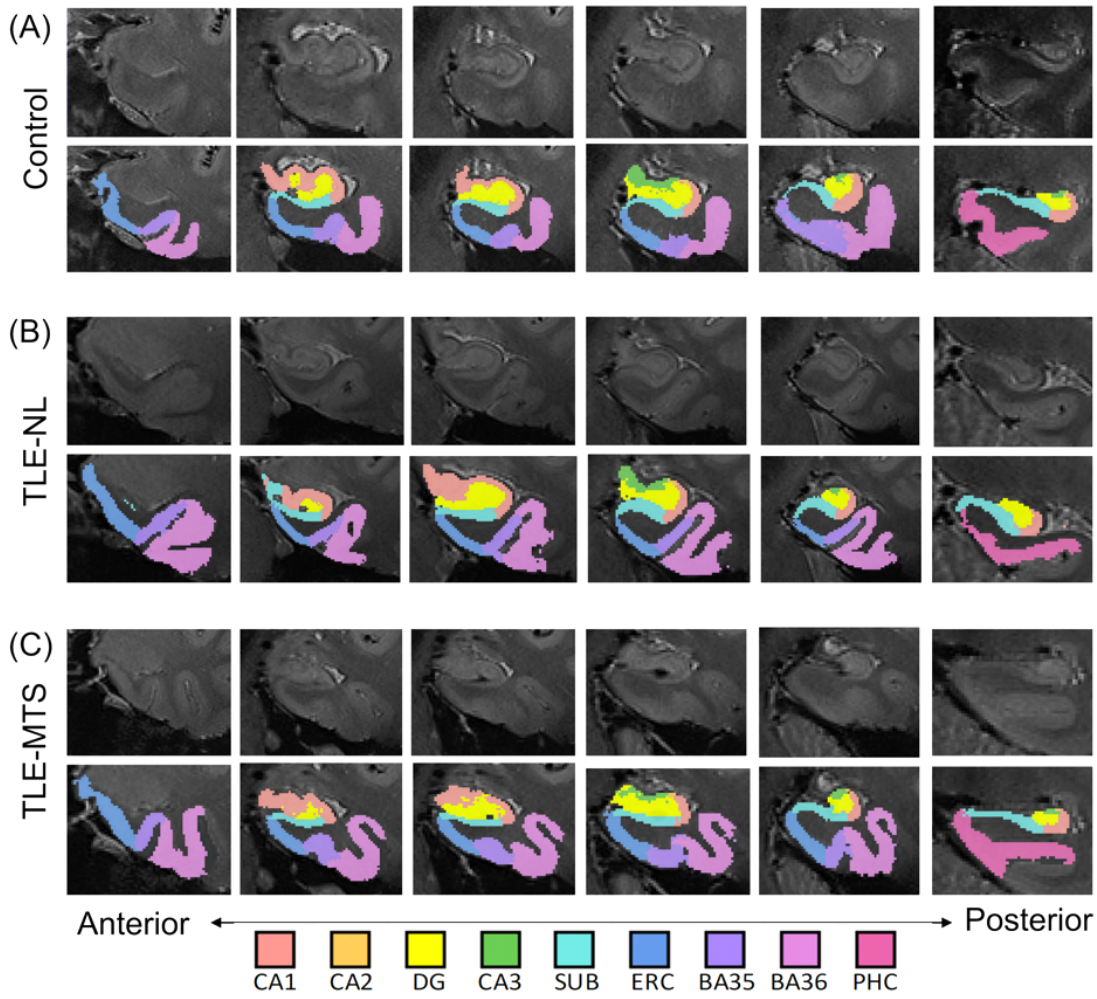

Figure 4.2: T2-weighted MRI coronal slices and corresponding automated segmentations overlaid onto left MTL in a representative (A) healthy control subject, (B) left-sided TLE-NL subject, and (C) left-sided TLE-MTS subject. High-resolution 7T MRI reveals grossly normal MTL architecture in controls and TLE-NL patients including clearly visible hippocampal digitations, and distortion of hippocampal architecture in TLE-MTS.

4.3.4 MTL Volumetric Asymmetry from Structural MRI

For TLE-MTS and TLE-NL, we computed volumetric asymmetry indices for each MTL subregion. We also computed an asymmetry index for the hippocampus

proper (CA1 + CA2 + CA3 + DG) to facilitate comparison of our findings to prior literature on whole hippocampal volumetry in TLE-MTS, and since this is the region of interest in the ILAE classification scheme for TLE-MTS [189]. Volumetric asymmetry indices were defined as [*(Contralateral – Ipsilateral)/(Contralateral + Ipsilateral)]*. To account for the presence of inter-hemispheric asymmetries in healthy controls, these indices were subsequently normalized via a *z*-score transformation with respect to the corresponding distribution of asymmetries in healthy controls [190]

4.3.5 MTL Functional Network Asymmetry

We describe our preprocessing pipeline for the resting-state BOLD-fMRI data in detail in our previous work [177]. Briefly, we applied EPI distortion correction using *B0* maps, six-parameter rigid body motion correction [81], coregistration and resampling of the fMRI data to the high-resolution structural MRI space [82], band-pass filtering to 0.008 - 0.08 Hz, linear regression to factor out effects of global, mean white matter and mean cerebrospinal fluid signals [83], as well as 12-parameter motion regression [85,86]. To construct functional connectivity matrices for each subject, we calculated the Pearson correlation coefficient between the average residual time-series signals for all pairs of MTL subregions [88]. We subsequently thresholded these matrices to remove negative weights [96] and applied a Fisher *r-z* transform for variance stabilization [89]. In these networks, the MTL subregions served as network nodes, while the strength of correlation between subregions served as network edges. Next, we computed three local network metrics that have proven particularly useful in describing important dimensions of

variation in brain networks – connectivity strength (k_i), clustering coefficient (c_i), and efficiency (e_i) – largely due to their sensitivity to the markers of small-world architecture [17,93,100,104,106,191] (See **Supplementary Information** for details). Modifying our previously described global network asymmetry metric $\boldsymbol{v}$ [177] to allow for subregion-level analysis and to account for directionality in asymmetry, we defined a local lateralized network asymmetry index, $\boldsymbol{l(i)}$, as the mean of the asymmetry indices for each subregion $\boldsymbol{i}$ across the three network metrics. Formally,

$$l(i) = \frac{1}{3}\left[\left(\frac{k_{i+N/2} - k_i}{k_{i+N/2} + k_i}\right) + \left(\frac{c_{i+N/2} - c_i}{c_{i+N/2} + c_i}\right) + \left(\frac{e_{i+N/2} - e_i}{e_{i+N/2} + e_i}\right)\right], \qquad \textit{(Eq. 4.1)}$$

where the first *N/2* nodes correspond to the MTL subregions contralateral to seizure onset and the last *N/2* nodes correspond to the analogous MTL subregions ipsilateral to seizure onset. Intuitively, the variable $l(i)$ served as a simple summary metric of local intra-MTL functional network asymmetry. Like a standard asymmetry index, $l(i)$ can range from 0 to 1. We also computed the hippocampal network asymmetry as the weighted average of $l(i)$ over all regions in the hippocampus proper (CA1, CA2, CA3, DG), weighed by each region's bilateral volume. As in the volumetric asymmetry analysis, we normalized these indices via a *z*-score transformation with respect to the corresponding distribution of asymmetries in healthy controls.

4.3.6 Statistical Analysis

Statistical analyses were performed using nonparametric permutation-based tests (10,000 iterations) to avoid assumptions about the underlying distributions of the data.

Analyses were performed separately for each asymmetry modality (structural and functional). To characterize the difference in MTL subregional asymmetry between TLE-MTS and TLE-NL, we performed two-sample, two-tailed permutation tests for each subregion, using difference in group means as the test statistic. Additionally, within the regions for which there was a difference between TLE-MTS and TLE-NL, we performed one-sample two-tailed permutation tests to determine if the subregional asymmetries were significantly different from zero.

4.3.7 Software

Image processing, network analyses, and statistical analyses were implemented using SPM [120], FSL [121], ANTs [122], the Brain Connectivity Toolbox [96], and custom python scripts available publicly at https://github.com/shahpreya/MTLnet.

4.4. Results

4.4.1 MTL Volumetric Asymmetry

At the group level, we observed significant differences in volumetric asymmetries between TLE-MTS and TLE-NL in CA1, CA2, CA3, DG, and subiculum, as well as the whole hippocampus ($p < 0.05$, two-tailed two-sample permutation test) (**Figure 4.3a, Supplementary Table 4.1**). Laterality analysis indicated that there was significant positive asymmetry (contralateral volume > ipsilateral volume) within all of these regions

in TLE-MTS and within the whole hippocampus in TLE-NL (two-tailed one-sample permutation test) (**Figure 4.3a**).

At the individual patient level, we found that 4 of 4 TLE-MTS patients presented with positive volumetric asymmetries (contralateral > ipsilateral) in all hippocampal subfields (CA1, CA2, CA3, DG), subiculum, and BA35; 3 of those 4 patients also had positive volumetric asymmetries in the entorhinal cortex. The patterns of subregional asymmetry in individual TLE-NL patients were much more heterogeneous, with only 2 of 9 patients exhibiting positive asymmetries (contralateral > ipsilateral) across all hippocampal subfields, though 7 of 9 patients exhibited whole-hippocampal positive asymmetry. Subject-level volumetric asymmetry heat maps (**Supplementary Figure 4.1a)** and group-averaged volumetric asymmetries mapped onto MTL segmentations (**Figure 4.3b**) illustrate these patterns.

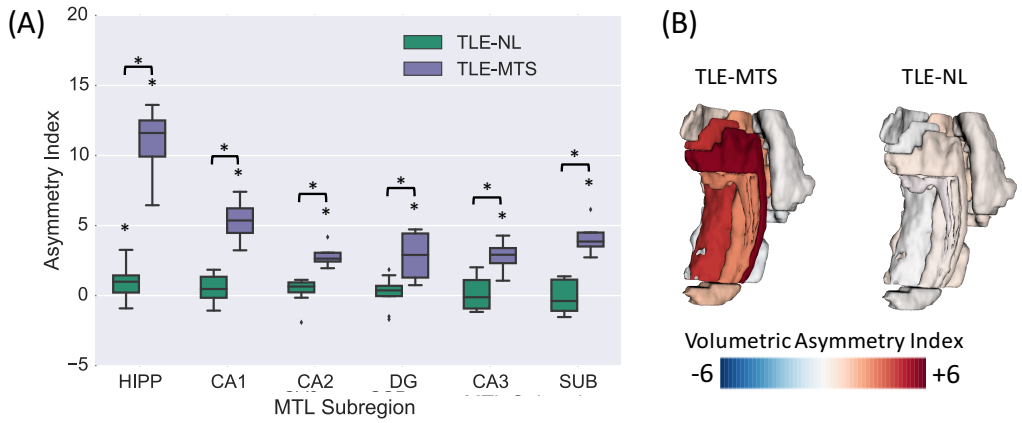

Figure 4.3: MTL volumetric asymmetry analyses. (A) Normalized volumetric asymmetries in TLE-NL and TLE-MTS patients (*$p < 0.05$) in hippocampal ROIs. (B) Visualization of mean volumetric asymmetries overlaid onto MTL segmentation for each TLE group.

4.4.2 MTL Functional Network Asymmetry

At the group level, we found significant differences in functional network asymmetries between TLE-MTS and TLE-NL in CA1 and the whole hippocampus ($p < 0.05$, two-tailed two-sample permutation test) (**Figure 4.4a, Supplementary Table 4.1**). Laterality analysis indicated that within the CA1 and the whole hippocampus, there was significant positive asymmetry (contralateral > ipsilateral) in TLE-MTS and significant negative asymmetry (ipsilateral > contralateral) in TLE-NL (two-tailed one-sample permutation test) (**Figure 4.4a**).

At the individual patient level, we found that 4 of 4 TLE-MTS patients presented with positive functional network asymmetry values (contralateral > ipsilateral) in the CA1 and BA35 subregions, whereas patterns of functional network asymmetry in the remaining MTL subregions were heterogeneous. In contrast, we found that 8 of 9 TLE-NL patients exhibited negative functional network asymmetry values (ipsilateral > contralateral) in the whole hippocampus, with the majority of TLE-NL patients also having negative functional network asymmetry in individual subfields CA1 (7/9), CA2 (8/9), CA3 (8/9), and DG (7/9). Subject-level functional asymmetry heat maps (**Supplementary Figure 4.1b)** and group-averaged functional network asymmetries mapped onto MTL segmentations (**Figure 4.4b**) illustrate these patterns.

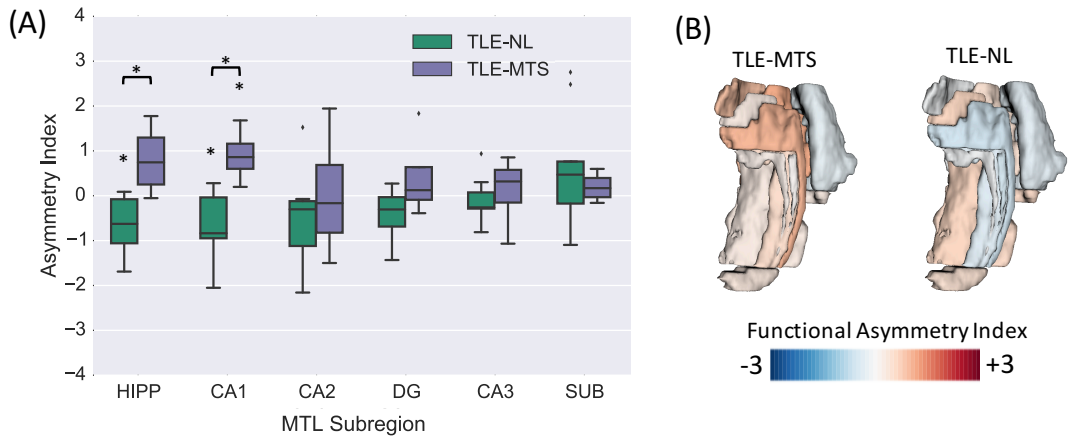

Figure 4.4: MTL functional asymmetry analyses. (A) Normalized functional asymmetries in TLE-NL and TLE-MTS patients (*$p < 0.05$) in hippocampal ROIs. (B) Visualization of mean functional asymmetries overlaid onto MTL segmentation for each TLE group.

4.5 Discussion

The goal of this study was to develop an approach to explore MTL subregional asymmetry-based metrics in TLE, and characterize differences between TLE-NL and TLE-MTS. First, we performed automated segmentation of MTL subregions on 7T MRI data from TLE-MTS and TLE-NL patients as well as healthy controls. Next, we computed subregional volumetric asymmetries from T2-weighted MRI and functional network asymmetries from resting-state BOLD fMRI. We found that patterns of volumetric and functional asymmetry were different between the two TLE subtypes. Notably, we found distinct patterns of functional asymmetry in the CA1 subfield and whole hippocampus, with TLE-NL patients exhibiting negative (ipsilateral >

contralateral) functional network asymmetry, and TLE-MTS patients exhibiting positive (contralateral > ipsilateral) functional network asymmetry.

4.5.1 Asymmetry-based findings

We found that TLE-MTS patients exhibited positive volumetric asymmetry (i.e. contralateral connectivity was greater than ipsilateral) in the whole hippocampus, and multiple hippocampal subfields. These findings are consistent with our knowledge that MTS is associated with histological patterns of neuronal loss and gliosis which can be limited to Ammon's horn (CA subfields of the hippocampus) or extend to the dentate gyrus and extra-hippocampal MTL subregions [154,192]. Additionally, our findings corroborate a hippocampal subfield neuroimaging study at 4T which revealed ipsilateral atrophy in CA1, CA2, and combined CA3&DG subfields in TLE-MTS, but did not reveal significant atrophy in TLE-NL [30]. Our findings are also consistent with another recent study at 3T that revealed volume reduction in multiple hippocampal subfields in TLE-MTS but not TLE-NL [193]. Consistency with prior studies validates our approach of applying automated segmentation algorithms to 7T structural MRI to characterize expected patterns of asymmetry in TLE-MTS.

We also observed that TLE-MTS patients exhibited statistically significant positive functional network asymmetry in the CA1 subregion. This observation corroborates prior resting state fMRI findings of reduced ipsilateral functional connectivity within the MTL in TLE studies in which all [159] or most [194,195] patients

had MTS. In contrast, TLE-NL patients exhibited significant negative functional network asymmetry (i.e. ipsilateral connectivity was greater than contralateral) in the whole hippocampus and in CA1, and this trend was present for all hippocampal subfields. While further work is necessary to provide a mechanistic explanation for this observation, studies using intracranial recordings indicate that epilepsy is characterized by increased synchronization in the epileptic zone both ictally [153,196–198] and interictally [199,200]. Therefore, an increase in ipsilateral functional network connectivity relative to the contralateral side could indicate greater synchronization of the seizure onset region with the remaining MTL network, even during the interictal state. The localization of functional network asymmetry to CA1, along with our previous finding that CA1 is a functional hub within the MTL network [177], support the hypothesis that CA1 is a key player in the TLE-NL network and could be a target for ablation or stimulation.

The different patterns of asymmetry in TLE-MTS and TLE-NL indicate that these two TLE subtypes have distinct phenotypes. Our findings add to a growing body of literature suggesting that MRI-negative TLE may have a different pathophysiology than TLE-MTS and is not simply an early variant [167–171]. These differences suggest that future studies would do well to separate these subtypes in group-level analyses to further characterize their differences and avoid confounding effects.

4.5.2 Methodological Considerations and Limitations

Our findings in TLE-MTS patients should be interpreted with caveats. First, since MTS is associated with loss of normal internal hippocampal architecture due to neuronal cell loss and gliosis [201,202], as well as hyperintensity on T2-weighted images [153,203], segmentation boundaries in TLE-MTS patients are inherently less reliable than in subjects with normal MTLs. These observations suggest that the volumes computed from these patients have an intrinsically higher degree of uncertainty. A related consequence is that segmented subregions include gliotic and sclerotic tissue, which may be functionally inactive. Such altered tissue functionality could explain decreased ipsilateral functional hippocampal connectivity in MTS patients. Since the presence of distorted MTL architecture is a fundamental property of MTS, it cannot be avoided. However, we did visually inspect all subjects' segmentations to confirm that they were consistent with our knowledge of MTL architecture. Moreover, since our segmentations are automated, they are free from human bias.

It is important to note that the differences in functional connectivity between TLE groups and controls were subtle, and that our sample size was modest. Therefore, our findings should be corroborated on larger datasets across multiple institutions, scanners, and protocols. We also note that there is considerable heterogeneity inherent to epilepsy patient data, including potential confounding factors such as duration of epilepsy, number of drug trials, cause of epilepsy, laterality, etiology, and seizure frequency. While we attempted to minimize confounds by limiting our dataset to subjects with clearly defined

mesial temporal origin and no extra-mesial abnormalities, we emphasize that our study is exploratory. Nonetheless, our approach paves the way for future studies in larger cohorts and in combination with other modalities. Additionally, our methodology can be applied to other disorders in which hippocampal asymmetry has been implicated, such as schizophrenia [204], Alzheimer's disease [205], and semantic dementia [206].

4.5.3 Conclusion

This study presents preliminary data characterizing intra-MTL structural and functional asymmetry in TLE and has important implications for our understanding of MTL topology in both normal and pathological human brains. We hope these results will encourage further research on the utility of MTL subregional asymmetry features for precise localization of abnormalities in TLE, allowing for more targeted therapies. While further validation in larger datasets is needed along with comparison to other modalities, our study highlights the promise of combining high-resolution imaging, automated segmentation techniques, and network analytical approaches in order to uncover brain network abnormalities that were previously invisible.

4.6 Supplementary Information

4.6.1 Mathematical definitions and intuitive descriptions of network metrics

As described in the main text, we characterized the MTL networks as graphs, comprised of nodes and edges. Such graphs can display heterogeneous structure that is important for the system's function [207]. While a number of graph statistics have been

defined to understand this heterogeneous structure, many of them are correlated with one another, especially in brain networks [94,95]. It is useful to choose a set of graph statistics that describe important dimensions of variation in brain networks but that are not necessarily redundant. Historically, measures that have proven particularly useful in characterizing brain graphs include the connectivity strength, clustering coefficient, and network efficiency [17], largely due to their sensitivity to the markers of small-world architecture [93]. We therefore computed local connectivity strength, clustering coefficient, and network efficiency for the functional networks. Because the most widely-applied definitions for these metrics require non-negative edge weights [96], and because the meaning of negative correlations is not well understood [97–99], we set negative edge weights to zero. We define the network metrics used in this study below.

Connectivity Strength: The local connectivity strength *k(i)* at node *i* for a weighted network with a set of nodes, *N*, is the sum of the weights of all connections to node *i* as follows:

$$k_i = \frac{1}{N}\sum_{j \in N} w_{ij} , \qquad \textit{(Eq. S4.1)}$$

where w_{ij} is the edge weight between node *i* and node *j*.

Clustering Coefficient: The local clustering coefficient *c(i)* at node *i* can be conceptualized as the likelihood that the neighbors of *i* are interconnected. One way in which to quantify this concept for weighted networks is:

$$c_i = \frac{2}{k_i(k-1)} \sum_{j,h \in N} \left(\widetilde{w}_{ij} \widetilde{w}_{ih} \widetilde{w}_{jh} \right)^{1/3}, \qquad \textit{(Eq. S4.2)}$$

where the weights are scaled by the largest weight in the network, i.e. $\widetilde{w}_{ij} = w_{ij}/max(w_{ij})$ [100].

Network Efficiency: The local network efficiency *e(i)* is often thought of as a measure of the capacity of node *i* to transfer information throughout the network [101,102], although for caveats in this interpretation, see also Rubinov and Bassett, 2011. It can be defined as follows [104]:

$$e_i = \frac{1}{N-1} \sum_{i \neq j \in N} \frac{1}{L_{ij}}, \qquad \textit{(Eq. S4.3)}$$

where L_{ij} is the shortest weighted path length between node *i* and node *j*, where the length of each edge is given by the reciprocal of the edge weight, $1/w_{ij}$.

4.6.2 Supplementary Figures

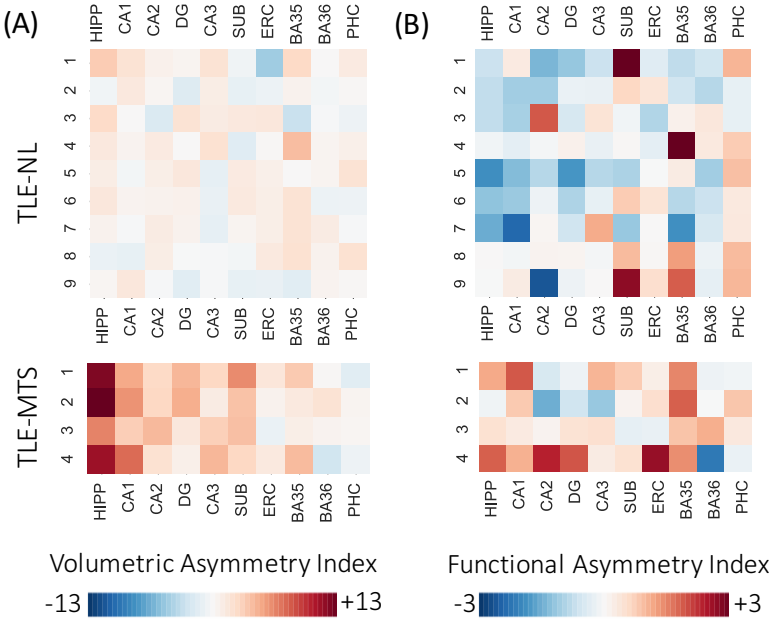

Supplementary Figure 4.1: Individual subject level heat maps of (A) volumetric and (B) functional network asymmetries for the whole-hippocampus and for individual MTL subregions in TLE-NL patients and TLE-MTS patients.

	z-scored Volumetric Asymmetry			z-scored Functional Network Asymmetry		
Subregion	**TLE-MTS (mean +/- SD)**	**TLE-NL (mean +/- SD)**	***P***	**TLE-MTS (mean +/- SD)**	**TLE-NL (mean +/- SD)**	***p***
HIPP	10 +/- 2.7	0.98 +/- 1.2	*	0.8 +/- 0.71	-0.66 +/- 0.58	*
CA1	5.3 +/- 1.5	0.45 +/- 0.89	*	0.9 +/- 0.53	-0.62 +/- 0.70	*
CA2	2.9 +/- 0.8	0.36 +/- 0.89	*	0.02 +/- 1.27	-0.54 +/- 0.98	n.s
DG	2.8 +/- 1.7	0.18 +/- 1.12	*	0.42 +/- 0.84	-0.4 +/- 0.52	n.s
CA3	2.8 +/- 1.2	0.28 +/- 1.19	*	0.11 +/- 0.72	-0.11 +/- 0.48	n.s
SUB	4.1 +/- 1.2	-0.06 +/- 1.06	*	0.19 +/- 0.29	-0.53 +/- 1.2	n.s
ERC	0.6 +/- 0.93	-0.10 +/- 1.78	n.s	0.78 +/- 1.13	-0.09 +/- 0.48	n.s
BA35	2.4 +/- 1.36	0.94 +/- 2.01	n.s	0.99 +/- 0.30	0.34 +/- 1.15	n.s
BA36	-0.01 +/- 1.6	0.18 +/- 0.51	n.s	-0.29 +/- 1.0	-0.38 +/- 0.38	n.s
PHC	-0.04 +/- 0.75	0.50 +/- 0.93	n.s	0.18 +/- 0.45	0.49 +/- 0.54	n.s

Supplementary Table 4.1: Table of volumetric and functional asymmetry values for each subregion. *p <0.05; n.s: not significant (two sample, two-tailed permutation test).

Chapter 5: Using intracranial EEG to map brain networks

Recordings from iEEG can capture brain signals from epilepsy patients with high spatial and temporal resolution. In Chapters 5 and 6, I demonstrate quantitative, subject-specific approaches to mapping brain networks using iEEG. In this chapter, I introduce the utility of iEEG in mapping brain function. Specifically, this chapter presents a collaborative work in which we develop an iEEG-based method for individualized spatiotemporal mapping of language networks in epilepsy patients.

Reference: Williams ST, Shah P, Piai V, Gatens H, Krieger AM, Lucas TH, Litt B. Electrocorticography reveals spatiotemporal neuronal activation patterns of verbal fluency in patients with epilepsy. *Submitted to Brain and Language*.

5.1 Abstract

Verbal fluency tests are commonly used to evaluate cognitive dysfunction in a variety of neurologic and psychiatric diseases, however the neuroanatomic substrates underlying performance of these tasks are incompletely understood. Intracranial EEG (iEEG) provides a unique opportunity to investigate temporal activation patterns during cognitive and motor tasks with high spatial and temporal precision. We studied cortical and subcortical high gamma activity patterns in seven patients undergoing pre-surgical evaluation for intractable epilepsy as they completed a verbal fluency task. We characterized spatiotemporal changes in high gamma activity associated with overtly produced utterances in a standard letter- and category-motivated free recall format. Recordings demonstrated robust changes in high gamma activity during pre-utterance, peri-utterance and post-utterance timeframes associated with cognitive search and speech production processes. The differences between letter and category fluency varied in timing and location across subjects. We interpret the spatial and temporal findings in this group of subjects during different components of language production, and propose a model of verbal fluency based on these and prior observations. Given that activation patterns beyond the primary language and motor cortices are heterogeneous across subjects, we recommend that invasive strategies to improve language in patients with neurological disorders will need to be individualized.

5.2 Introduction

Verbal fluency testing is a commonly used tool to evaluate cognitive dysfunction in a variety of neurologic and psychiatric diseases. Patients are typically given a criterion and instructed to verbally produce as many fitting exemplars as they can within a 60 second timeframe. The most common criteria are categories (e.g. animals, supermarket items) wherein exemplars should be members of the designated category, or letters (e.g. F, A, S) wherein exemplars should begin with the designated letter. Inability to produce an adequate number of exemplars in the category-motivated condition indicates a semantic verbal fluency deficit and can be seen in frontal or temporal lobe lesions, schizophrenia, dementias and left temporal lobe epilepsy [208–210]. Letter-motivated (phonemic) fluency deficits are seen in frontal lobe lesions, left frontal lobe epilepsy, dementias and attention deficit hyperactivity disorder [209–211].

Verbal fluency tasks differ from other word production tasks (e.g. picture naming, verb generation or sentence completion) in that prior to lexical selection, there is a prerequisite conceptual preparation step that depends on successful free (or internally constrained) recall of the word to be generated. It is reported that subjects tend to produce exemplars in clusters of semantically or phonemically related items. The underlying cognitive search process is postulated to include two major components: identification of clusters of exemplars fitting a given sub-criterion, and execution of an overarching control function, possibly in left inferior frontal gyrus, that switches among sub-criteria once a particular cluster has been exhausted [212–214].

Despite the widespread use of this test in clinical practice, there is limited understanding of the neurophysiologic processes underlying its performance. Positron-emission tomography (PET) studies before and during letter-cued verbal fluency tasks have demonstrated increased metabolism primarily in bitemporal regions [215,216]. Using functional magnetic resonance imaging (fMRI), activation has been demonstrated in the bilateral superior and left inferior frontal gyrus, medial prefrontal cortex, left insula and the right cerebellum [217–219]. Letter-motivated fluency may depend more heavily on the left inferior frontal gyrus (in particular BA44) by comparison to category-driven tasks, while left occipitotemporal cortex demonstrates the reverse affinity [220–222]. In addition to neocortical regions, bilateral hippocampi show increased BOLD activity and increased connectivity to semantic language networks in category- but not letter-cued verbal fluency [223].

In contrast to fMRI findings, similar comparisons using near infrared spectroscopy (NIRS) suggest greater activation in the prefrontal regions bilaterally during letter-motivated fluency, and in the left (inferior) frontal regions during category-motivated fluency tasks [224]. The reasons for this distinction are not clear, but may relate to differences in methodology, task difficulty, age or sex of the subjects included, all of which may influence the observed activation patterns [225,226]. These neuroimaging modalities provide important insights to the neuroanatomical substrates underlying verbal fluency tasks, but they lack the resolution necessary to probe the temporal dynamics of cognitive subprocesses supporting verbal fluency tasks.

One study did use magnetic source imaging (MSI) to investigate temporal activation patterns of selected cortical regions in a paced version of the verbal fluency test [227]. The authors noted earlier activation in precentral and supplementary motor regions compared to inferior frontal or insular regions. Their results also suggested a peak in inferior frontal gyrus/anterior insula activity at about 600 milliseconds after letter stimuli, which was not present after categorical stimuli. To our knowledge, no study to date has examined the spatial and temporal neuronal activation patterns associated with generation of exemplars in the self-paced verbal fluency test commonly administered in clinical practice. While this test is difficult to administer in an fMRI environment due to confounders of movement artifact, it can be administered while patients are undergoing intracranial electrocorticographic (ECoG) monitoring. High gamma power derived from ECoG recordings is a useful metric for examining the physiological patterns underlying cognitive processes with excellent spatial and exquisite temporal resolution. This measure has previously been used to elucidate patterns in auditory processing [228], word repetition [229], picture naming, verb generation [230] and other processes. The technique allows investigators to probe neuronal functions with the same temporal resolution within which related cognitive functions are postulated to occur. Gamma oscillations have been investigated in a free recall memory paradigm, and shown to predict successful memory formation during encoding and to distinguish true from false memories at recall [231,232]. However, no study to date has investigated the

spatiotemporal dynamics of the verbal fluency task, which combines a free recall format with long-term memory and language production processes, in real time.

We used high gamma activity as measured on ECoG to investigate the functional language network architecture during an overt, self-paced verbal fluency task in patients with epilepsy. We postulated that individual responses would be associated with pre-utterance activation in the precentral and inferior frontal region, and post-utterance activation in the superior temporal gyrus, as has been demonstrated in prior studies of speech production. We further expected that distinctions between the category fluency condition and the letter fluency condition would exist primarily during timeframes attributable to cognitive search. Based on our observations, we propose a model for word production during this frequently used but incompletely understood test of cognitive function.

5.3 Methods

5.3.1 Patients

We studied seven patients undergoing pre-surgical intracranial EEG monitoring for drug-resistant epilepsy. Subdural strip, grid, and in some cases depth electrodes were implanted in locations based on clinical necessity. The study was approved by the Institutional Review Board of the University of Pennsylvania, and all subjects provided informed consent prior to participating.

Electrodes for each subject were localized by co-registering post-operative CT with post-operative MRI, and subsequent transformation into MNI152 space. The Harvard-Oxford Atlas provided through the FMRIB Software Library [233] was used to assign an anatomical cortical or subcortical label to each electrode contact. Electrode localizations were confirmed by visual inspection by a trained neuroradiologist.

5.3.2 Task Procedures

Participants were presented with either a category or a single letter and instructed to overtly produce as many words as possible fitting that category or starting with that letter in a 60 second period. Stimuli were presented verbally to ensure comprehension. Participants were instructed to avoid repeating words and to keep eyes closed during the entire task. To reduce distraction and frustration, patients were allowed to 'pass' to end blocks early in cases where they had exhausted all the words they could think of. Six category stimuli and six letter stimuli were presented to each subject, interspersed with resting blocks during which participants were requested to remain quiet with eyes closed for 60 seconds (**Figure 5.1**). Stimuli were selected based on those commonly referenced in the verbal fluency literature. The following category stimuli were chosen: animals, fruits, tools, supermarket items, vehicles and body parts. The following letter stimuli were chosen: F, A, S, C, P, L. The stimuli were presented in varying orders for each subject, such that there were no two resting blocks in succession, and that there were no more than two task blocks of the same condition (letter or category) in succession. The

entire procedure, including rest blocks, instructions and clarifications, typically occurred over 20-25 minutes for each subject.

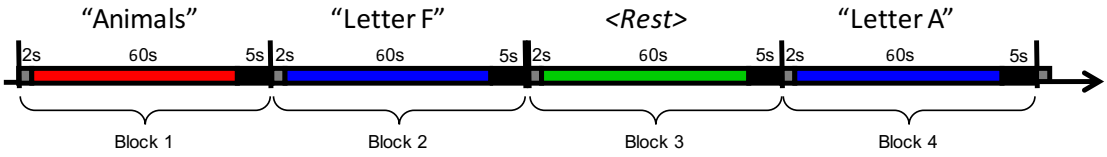

Figure 5.1: Stimulus presentation paradigm. Subjects were instructed to lay quietly with eyes closed. Six CATEGORY blocks (indicated in red), 6 LETTER blocks (blue), and 6 REST blocks (green). Stimuli were presented orally to ensure comprehension, and delivered in varying order such that no two rest blocks were sequentially together, and that there were no more than two task blocks of the same type. For each stimulus, subjects were given 60 seconds to overtly produce as many exemplars as possible fitting the stimulus criterion, avoiding proper names and repetitions. To minimize frustration and distraction, subjects were allowed to 'pass' to end blocks early if they felt they had exhausted their mental lexicon.

5.3.3 EEG Collection and Behavioral Recording

Electrocorticography (ECoG) data were sampled at 500 to 1000 samples/second using a 128 channel Natus XLTek data acquisition machine. Data were subsequently exported in EDF format, deidentified and uploaded to the International Epilepsy Electrophysiology Portal (ieeg.org) for annotation, review and analysis. Overt verbal responses were recorded digitally and audio files were manually synchronized to the EEG recording. Audio files were transcribed manually using Audacity (http://www.audacityteam.org/) and the resulting annotations marking the onset of each utterance were merged with the EEG recording in the international electrophysiology portal (ieeg.org) using proprietary MATLAB scripts.

5.3.4 EEG Analysis

Intracranial EEG recordings were visually inspected and segments containing artifact, seizures or epileptiform discharges were discarded. We utilized common average referencing to reduce effects of correlated noise in the signal and spatial bias from the reference electrode. Data in category-driven and letter-driven blocks were then organized into 2-second epochs associated with each word utterance, ranging from 1.25 seconds pre-utterance to 0.75 seconds post-utterance. To reduce overlap of signal from adjacent words, we removed epochs containing words with onset less than 1 second following or less than 0.5 seconds prior to another word. We also organized resting blocks into non-overlapping 2s epochs to establish a baseline. Next, we utilized a Thomson multitaper method to compute spectral power using a time-halfbandwidth power of 7 and 13 Slepian tapers. For semantic and phonemic conditions, the time-varying power spectrum was computed across each epoch, using 200ms overlapping windows with 10ms spacing. For the rest condition, we computed the mean power spectrum across the entire epoch. The resulting spectra were averaged across the gamma frequency range of 70-110 Hz, and subsequently log-transformed. To allow for consistent scaling across channels, we then normalized the time-varying gamma powers in the semantic and phonemic conditions by the rest period power as follows:

$$t = \frac{x - \mu_{rest}}{\sigma_{rest}}, \qquad \textit{(Eq. 5.1)}$$

where *t* is the normalized gamma power, *x* is the original gamma power, and μ_{rest} and σ_{rest} are the mean and standard deviation of the gamma power in the rest condition, respectively.

5.3.5 Statistical Analyses

We performed our analyses individually within each subject to account for the distinct sampling patterns dictated by each subject's clinical requirements, the likelihood that each subject would have unique network topologies subserving cognitive function, and the spatial precision with which high gamma activity is often observed [230,234]. We sought to answer two key questions: (1) What are the key spatiotemporal patterns of activity during self-paced verbal fluency utterances compared with rest? (2) What brain regions exhibit a difference in activity between semantic and phonemic verbal fluency tasks during key phases of word production? To answer question 1, we categorized each channel's high gamma activity plot by its earliest time of activation with respect to utterance onset. We set a threshold at $t = 1.96$ for the log-normalized high gamma power to be considered significantly different from rest. Although arbitrary, we chose this threshold to correspond to the quantile of the normal distribution that has a two-sided probability in the tail of 5%.

To investigate the timing of task-specific differences in neuronal activation patterns, we computed differences in early (-850ms to -600ms), immediate pre-utterance (-250ms to 0ms), immediate post-utterance (0-250ms) and late post-utterance (400-

600ms) high gamma activity between conditions for each subject. These timeframes were selected with a goal of capturing salient differences between phonemic and semantic conditions at relevant timeframes based on prior models of word production (e.g., Indefrey et al. 2011). The early timeframe was postulated to reflect cognitive search, pre-utterance to reflect some components of word planning, immediate post-utterance to reflect articulatory motor processing and late activity to reflect auditory feedback. Actual mean differences between conditions in each time frame were compared to the distribution of mean differences determined by random permutation of epochs across conditions. We used 10,000 permutations and for each subject, identified channels that had a significant difference in gamma activity during semantic vs. phonemic tasks in early, pre, post and late periods, using the false discovery rate at 0.05 across channels to adjust for multiple comparisons. A more detailed description of the EEG statistical analysis can be found in Appendix 1 of the **Supplementary Information**.

5.4 Results

5.4.1 Subjects and behavioral task performance

We recruited seven (7) patients for this study. **Figure 5.2** summarizes the subject population and electrode coverage maps. There were 5 left hemisphere-predominant implants and 2 right-predominant implants, with a median of 114 (range 80-122) electrode contacts per participant. All participants were right handed by self-report and left-hemisphere dominant for language. There were 5 men and 2 women, and the median

age was 46 years (range 34-57 years). Five of the subjects had seizures recorded with mesial temporal onset (2 right, 2 left, 1 bilateral).

	1	2	3	4	5	6	7
Sex	M	M	M	F	F	M	M
Age in years (Onset age)	57 (48)	47 (15)	34 (18)	43 (24)	57 (12)	46 (44)	37 (34)
SOZ	Left mesial temporal	Left temporal (MTL + lateral)	Left STG	Right temporal	Bitemporal	Right frontal lesion	Right mesial temporal
Treatment	L LITT	L posterior inferior temporal lesion	None	R LITT	RNS	None	R ATL + lesionectomy
Outcome	ILAE 2 (15 mo)	ILAE 1 (21 mo)	N/A	ILAE 5 (8 mo)	ILAE 5 (18 mo)	N/A	ILAE 1 (10 mo)
Electrode Placement	Left grid, strips, mesial depths	Left grid, strips Left mesial temporal depths	Left grid	Left grid, strips Right strips Bilateral mesial temporal depths	Left grid, strips Right strips Bilateral mesial temporal depths	Right grid, strips, depths, stereo	Right grid, strips, depths

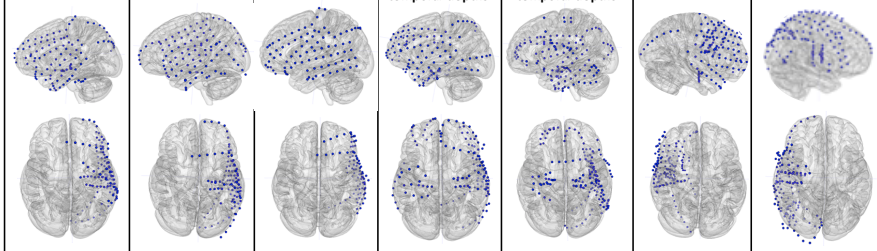

Figure 5.2: Clinical profiles and electrode placement. All participants were right handed by report and had onset of seizures after primary language development. Seizure onset zones are documented as identified during implant admission. Blue dots superimposed on grey brains indicate electrode localizations. *ATL: anterior temporal lobectomy; CT: Computed Tomography; ILAE: International League Against Epilepsy (Wieser et al, Epilepsia 2001); LITT: laser interstitial thermal therapy; MRI: magnetic resonance imaging; MTL: mesial temporal lobe; RNS: responsive neurostimulation; SOZ: Seizure onset zone; STG: superior temporal gyrus*

Table 5.1 and **Supplementary Figure 5.1** summarize behavioral task performance. Because subjects were allowed to 'pass' to end blocks earlier than 60 seconds, we used production rate (number of correct exemplars per minute) as a surrogate for task performance. Overall, there was a broad range of performance with lower scores on phonemic (letter-cued) verbal fluency tasks ($p = 0.012$ by paired sample *t*-test).

Patients with mesial temporal lobe involvement of their epilepsy tended to perform worse than those without mesial temporal involvement in both category-driven and letter-driven tasks. The two women in the study, the only subjects with bilateral mesial temporal lobe epilepsy, also appeared to perform worse than the men. However, the sample sizes of individual subgroups were too low to support formal statistical evaluation by sex, epilepsy type or laterality.

Subject	Letter (exemplars/min)	Category (exemplars/min)
1	12.3	10.8
2	7.7	13.1
3	15.6	20.5
4	5.3	10.2
5	7.1	11.8
6	15.5	26.6
7	7.8	12.9
Mean (SE)	**10.2 (1.6)**	**15.1 (2.3)**

Table 5.1: Behavioral task performance. Mean production rate of correct exemplars uttered per 60 seconds under category-based (semantic) and letter-based (phonemic) verbal fluency conditions. All subjects underwent 6 blocks each of semantic verbal fluency, phonemic verbal fluency and rest (silent, cognitive function unconstrained) in pseudorandomized order.

5.4.2 Spatiotemporal activation patterns associated with word utterances

Figure 5.3 and **Figure 5.4** depict mean (with 95% confidence intervals) high gamma activity patterns at selected electrodes in the letter-motivated and category-motivated conditions for subjects 1 and 6, respectively. Activity exceeding the t =1.96 threshold relative to resting baseline is identified by colored bars across the top of each

graph. Regions of elevated high gamma activity at selected time intervals are shown for all subjects individually in **Supplementary Figure 5.2**. Dynamic videos of the pooled activation maps are also provided in the online supplementary information.

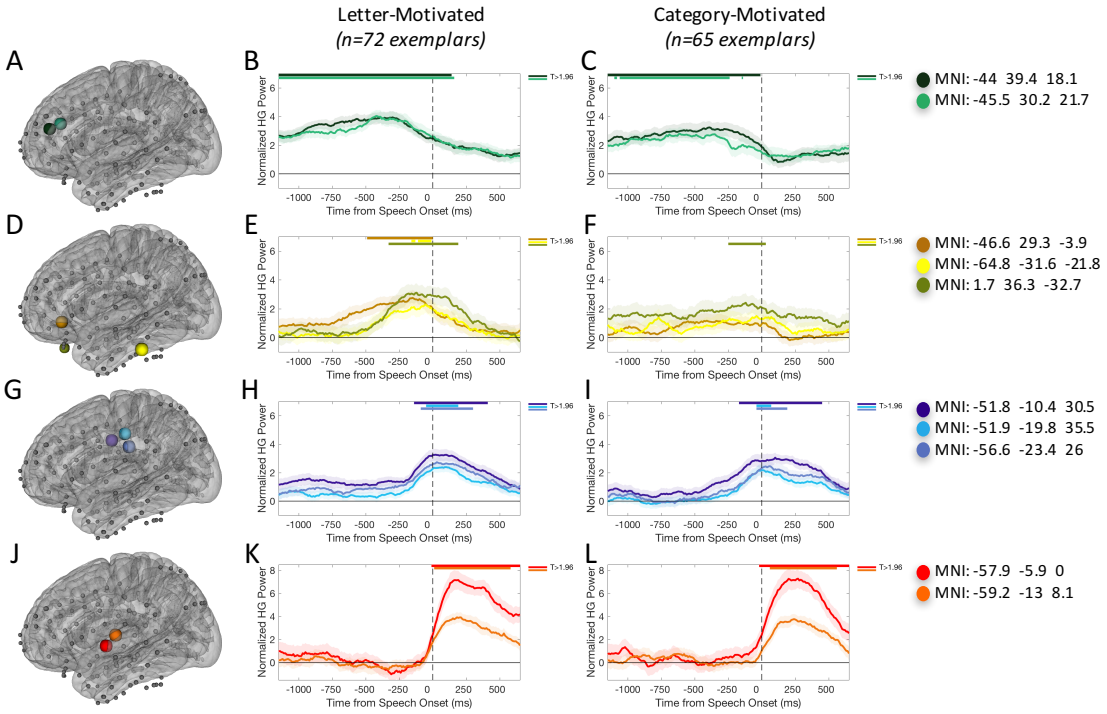

Figure 5.3: Temporal activation patterns at selected electrodes with suprathreshold high gamma activity at varying times with respect to speech utterance onset for subject 1. High gamma power is log-normalized to resting power at each electrode contact. Activity exceeding the t =1.96 threshold relative to resting baseline is identified by colored bars across the top of each summary graph. Panels A-C illustrate patterns for electrodes active more than 750ms prior to speech onset. Activity during this timeframe, which is earlier than canonical speech production processes are expected to occur, may thus represent cognitive search. Panels D-F show tracings with peak activity within 600ms prior to speech onset, corresponding to a timeframe previously ascribed to word planning (phonological and phonemic encoding). This occurs in distributed regions of prefrontal and posterior temporal cortices, and was seen only in left hemispheric implants. Panels G-I depict activity of peri-Rolandic electrodes, which begins rising 200-300ms prior to speech onset and peaks 50-250ms after onset, likely representing articulatory motor planning. Panels J-L show posterior temporal activity that peaks 400-500ms after utterance onset, possibly representing auditory feedback processing.

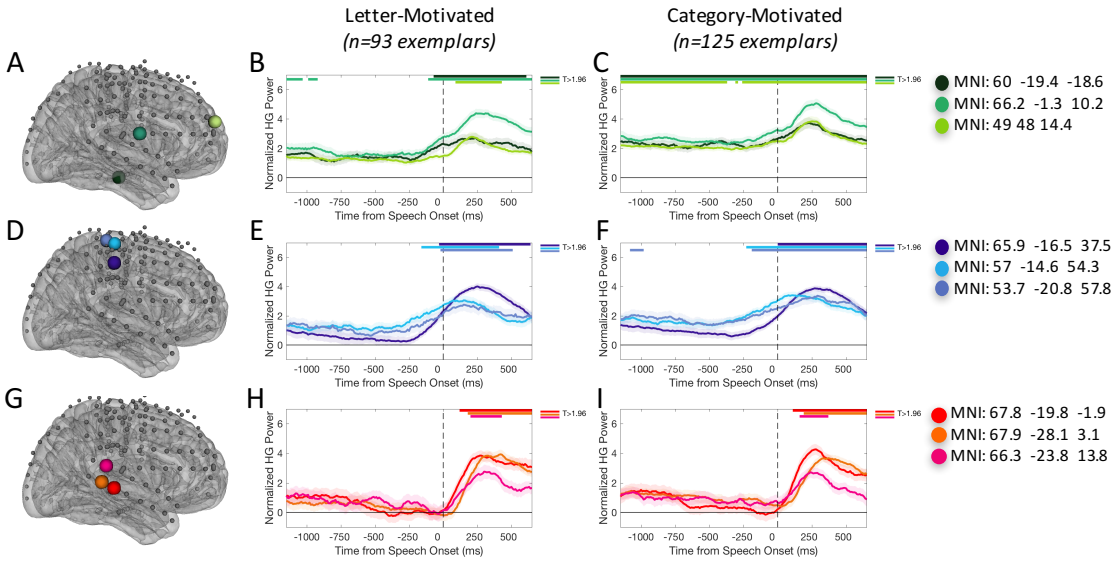

Figure 5.4: Temporal activation patterns at selected electrodes with suprathreshold high gamma activity at varying times with respect to speech utterance onset for subject 6. High gamma power is log-normalized to resting power at each electrode contact. Activity exceeding the t =1.96 threshold relative to resting baseline is identified by colored bars across the top of each summary graph. Panels A-C illustrate patterns for electrodes active more than 750ms prior to speech onset. Activity during this timeframe, which is earlier than canonical speech production processes are expected to occur, may thus represent cognitive search. Panels D-F depict activity of peri-Rolandic electrodes, which begins rising 200-300ms prior to speech onset and peaks 50-250ms after onset, likely representing articulatory motor planning. Panels G-I show posterior temporal activity that peaks 400-500ms after utterance onset, possibly representing auditory feedback processing.

Many electrode contacts showed no significant difference in high gamma activity from resting baseline. Among those that did show task-related fluctuations, we observed four principal patterns of activation common across subjects. Early (more than 750ms prior to speech onset) suprathreshold activity was present primarily in prefrontal regions, but also in parietal and subtemporal areas. Activity in these contacts typically diminished to subthreshold levels but remained qualitatively high with respect to resting activity (see

Figure 5.3, panels A-C and **Figure 5.4**, panels A-C). Early prefrontal activity was seen in both left and right hemispheric implants, although in right-sided implants it only reached suprathreshold levels in category fluency.

In a subgroup of electrode contacts there was also high gamma activity that peaked between 600ms prior to speech onset and 100ms after onset. This occurred in distributed areas of inferior frontal, orbitofrontal and temporal cortex, in keeping with prior models of word planning processes (lexical selection, phonological planning, syllabification). Interestingly, the electrodes that demonstrated this activity for letter fluency overlapped but were not exactly congruent with those demonstrating the same activity patterns for category fluency.

Electrodes in peri-Rolandic sensorimotor cortex demonstrated high gamma activity that reached suprathreshold levels less than 100ms prior to speech onset and peaked within 300ms after onset. This pattern is consistent with oromotor activation at the time of speech onset and is similar to observations in prior studies of overt reading, picture naming and verb generation tasks [230,235]. It was observed in both right and left hemispheric implants. Interestingly, in the right hemispheric implants a subset of peri-Rolandic electrodes demonstrated suprathreshold activity even at the early pre-utterance timepoints (i.e. 750ms or more prior to speech onset) for category fluency.

By contrast to prefrontal and peri-Rolandic electrodes, contacts over the posterior temporal and inferior parietal regions typically showed no significant difference from resting activity in the pre-utterance period. After speech onset, activity in these regions

rose dramatically to peak at 300-400ms post utterance. This pattern has also been observed in prior studies of speech production and may reflect auditory feedback processing in response to the subjects' own speech [230,234,235].

5.4.3 Comparison of patterns for category- and letter-motivated utterances

We used permutation testing to identify electrodes demonstrating significant differences in high gamma activity between letter and category conditions at specified epochs with respect to speech onset. See **Supplementary Figure 5.3** for illustration of electrodes meeting criteria for statistical significance at $p<0.05$, corrected for multiple comparisons. We observed considerable variability across subjects in the regions that appeared to activate differentially. In subjects 1-3, letter-motivated exemplars tended to elicit a more robust response than category-motivated exemplars in the regions sampled (mean 14.7% of electrodes with increased activity for letter fluency in the epochs examined, compared with 3.8% of those with increased activity for category fluency, $p = 0.075$). This was most prominent in the immediate pre-utterance timeframe (0-250ms prior to utterance onset), involving 66% of all differentially active electrodes for these subjects. Subjects 4, 5 and 7 demonstrated sparse differences in the regions sampled. Subject 6, who was the only subject without temporal lobe involvement of his epilepsy, demonstrated robust increases for category fluency throughout the regions sampled in all timeframes except immediately post-utterance (5.7% of electrodes with significant difference during this epoch by comparison to mean 38.3% with significant differences for other epochs; $p < 10^{-10}$ across epochs by Cochran's Q, corrected for multiple

comparisons). Of note, subjects 3 and 6, whose epileptic networks were limited to neocortical regions, demonstrated the largest percentage of cortical regions with significant differences between letter-based and category-based fluency (mean 45.3% of electrodes demonstrating differences for these two subjects, compared to 7% of subjects with mesial temporal lobe epilepsy), however limited group size precludes formal statistical comparison.

5.5 Discussion

This study demonstrates that overt, self-paced verbal fluency tasks can be successfully performed and evaluated using intracranial electroencephalography. Although several language paradigms have been implemented using iEEG, ours is the first study to investigate the high-resolution spatiotemporal activation patterns associated with spontaneous utterances in a free recall paradigm. Though the number of subjects in this study is small, our findings provide an interesting complement to existing verbal fluency literature, which averages neurophysiologic signals over several seconds at a time. Our observations have implications for current models of language production, and potentially for invasive strategies to improve language function. Below we interpret our findings, breaking them down into specific elements of the speech production process, and offer a possible explanatory model for how words are produced in the context of verbal fluency paradigms.

5.5.1 Spatial and temporal dynamics of spontaneous utterances

5.5.1.1 Conceptual and lexical retrieval processes

As previously discussed, verbal fluency tasks differ from other language production tasks in that the prerequisite conceptual preparation step depends on a memory search for acceptable exemplars. Studies of picture naming and verb generation suggest that subsequent sub-processes involved in word production (e.g. lexical selection, articulatory preparation) occur over the 600ms prior to articulation. We thus examined the time period earlier than 600ms prior to speech onset, positing that during this timeframe, subjects are actively engaged in cognitive search without significantly involving canonical lemma selection or articulation processes.

During this 'search' timeframe, we observed gamma activation including the superior and middle frontal regions across subjects on both category and letter fluency tasks. This activity was seen more prominently in left hemispheric implants during letter fluency, whereas category fluency did elicit 'search' timeframe activation in right frontal regions as well. Our findings are consistent with fMRI studies of verbal fluency tasks demonstrating increased blood oxygen level dependent (BOLD) activity in prefrontal cortex during these paradigms compared to rest or rote recitation [218,219,222]. By contrast, we did not see consistent involvement of the left inferior frontal gyrus, across subjects, as is reported in fMRI and PET literature on phonemic verbal fluency. While this may be partly due to incomplete electrode coverage in this region for some subjects, varying functional network architecture across individuals may also contribute. This may

be of particular significance in individuals with epilepsy, who are expected to have variation in functional and anatomic localization due to aberrant plasticity as a result of epileptiform activity, or the underlying cause of their seizures [236]. Of note, however, none of our subjects had seizure onset zones in the left frontal region.

Many of the areas active during the cognitive search timeframe showed a subtle decrease in high gamma activity 200-300ms prior to speech onset, but remained active throughout the remaining peri-utterance timeframe. This may signify that networks involved in conceptual search continue their function even while suitable exemplars are identified and speech production processes are launched in parallel. An alternative explanation is that the lexical search and speech production processes engage overlapping anatomical regions. Although the latter explanation seems less likely given that tasks involving only the latter processes (e.g. auditory word repetition or reciting well-known lists) do not typically result in extensive prefrontal activation [237,238], it is supported by the fact that in category fluency, a subset of the 'search'-active electrodes in our study demonstrated further *increases* in activity during later timeframes with respect to speech onset. In summary, our findings suggest that conceptual search processes employ prefrontal activation, and that these processes may continue in parallel with subsequent word planning and speech production processes.

5.5.1.2 Lexical selection and phonological encoding

Left hemispheric implants showed focal increases in high gamma activity that peaked less than 600ms prior to speech onset with a decline before or during articulation. These peaks occurred in distributed areas including left inferior frontal, middle frontal, inferior parietal and posterior temporal regions. Prior studies of word generation suggest that word planning (lexical selection, phonological and phonemic encoding) occurs during this timeframe (i.e. 200-400ms post-stimulus, assuming an average response latency of 600ms) [239]. Our observations are consistent with this model, and additionally suggest involvement of the middle frontal gyrus (MFG). Assuming a semantic network architecture is invoked during verbal fluency task execution [212,240], one might ascribe the MFG activation to lexical selection processes occurring during this timeframe. However, the MFG activity is notably more robust in the letter-motivated condition, wherein selection among competing potential exemplars with similar or overlapping meanings is unlikely to be a major component. A previous study found high gamma perturbations in the left MFG during word production tasks with visual stimuli and concluded that this region serves as a temporal perceptual information storage space [241]. We thus propose that in this subject the MFG also participates in the lexical selection subtask. Ideally a comparison to a task that isolates these sub-processes within the same subject would shed light on this picture, however real-time signal analysis to identify such needs was not available at the time of our recording.

Interestingly, the regions active during presumed word planning timeframes for letter fluency overlapped partly but not completely with those active for category fluency. We learn from this that the implementation of the two tasks may differ not only in the search mechanisms, but perhaps also in the cortical areas involved in word planning and production. Further studies with larger subject numbers and dedicated task paradigms would be useful to clarify this unintuitive implication.

5.5.1.3 Articulatory planning and execution

Starting at 200-300ms prior to utterance onset, we observed increases in high gamma activity in spatially precise but distributed areas of peri-Rolandic cortices. This activity was seen in both right and left implants and likely represents articulatory planning and motor activation. These findings are remarkably consistent with those observed in overt picture naming and verb-generation paradigms, as well as during syllable production [230,242]. Interestingly, subject 8 demonstrated a parallel pattern of activation in the temporo-parietal-occipital (TPO) junction, consistent with prior observations suggesting a 'subsystem' within Wernicke's area engaged in the motor act of speech in some subjects [230,243,244].

5.5.1.4 Feedback processing

In the post-utterance timeframe, we consistently observed dramatic high gamma activity increase in the posterior temporal and inferior parietal regions. This activity was seen bilaterally. Edwards et al. observed similar patterns in a picture naming and verbal

fluency tasks, and suggested it was a form of self-monitoring [230]. Using fMRI, Birn and colleagues [222] saw decreased activity in the posterior superior temporal regions during verbal fluency compared to an automatic speech task, suggesting that activity in this region is not a primary auditory phenomenon. Our observations may represent a correlate to the N400 event-related potential that typically occurs when subjects listen to natural speech, words and sentences [245,246]. We propose that posterior temporal activation in this context represents a combination of auditory feedback and semantic processing, noting that in several electrodes there is a difference between levels of activation induced by phonemic versus semantic stimuli. Such a hypothesis could be further evaluated with a dedicated task evaluating post-utterance activation compared with activation patterns during passive listening to words or hearing unexpected noises within subjects.

5.5.2 Category-motivated versus letter-motivated verbal fluency

We expected the earliest time period (more than 600ms prior to utterance onset) to demonstrate the most robust differences between semantic and phonemic verbal fluency because these two conditions require slightly different search strategies but presumably similar lexical selection and speech production processes [212]. Surprisingly, we found statistically significant differences across the peri-utterance timeframe. The epoch demonstrating the most widespread areas of differential activation across subjects was immediately pre-utterance (less than 250ms prior to speech onset). This suggests that

speech production processes specific to letter- or category-motivated verbal fluency occur most robustly in the period immediately prior to speech onset, or they are more differentially "jittered" with respect to speech onset. The latter explanation would be expected given that letter and category fluency tasks differ in level of difficulty, as a whole and as a function of the specific letter or category stimuli used. On the other hand, examples of processes that may be condition-specific and occur in this timeframe include pre-speech self-monitoring (e.g., internal self-monitoring, performing a last minute 'check' to validate that an exemplar to be uttered fits the stimulus criteria) or late parallel conceptual activation (e.g. invoking a word meaning *in response to* an orthographically or phonemically-driven lexical selection process). Further studies with larger datasets may shed light on these processes by examining the semantic and linguistic properties of exemplars associated with differential activation in the late pre-utterance timeframe.

Subject 6 was the only participant to demonstrate widespread increases in semantic verbal fluency across nearly all regions sampled. These were present during search, pre-utterance and late timeframes, but were less prominent during the immediate post-utterance epoch. In the late post-utterance timeframe (more than 250ms after utterance onset) the same subject also had widespread increases in response to category-motivated stimuli. This pattern was very different from those observed in other subjects. His relatively high performance in this task, as well as an epileptic network far removed from more classically localized language-generating regions, argue that he may represent a normal variant pattern. His network might also represent a different cognitive strategy

for completing the verbal test, for example relying more heavily on visualization during category-cued verbal fluency and/or self-monitoring of language output. Interestingly, the two patients with the highest performance in both letter and category fluency demonstrated the most widespread areas of difference between category and letter fluency. These also were the two patients without evidence of mesial temporal involvement in their seizures. Although the sample sizes are too small for formal statistics, this does beg the question of whether specialization contributes to performance and whether mesial temporal lobe epilepsy undermines this specialization, e.g., because of epilepsy-related plasticity or because of impaired memory retrieval due to mesial temporal dysfunction. The caveat is that electrodes were placed according to clinical necessity, so we got for example only 2 right hemisphere implants – it is thus impossible to assess the activity of the alternate hemisphere for these patients. Our lack of findings for the patients with lower performance could have been because all of their significant differences were in the contralateral hemisphere.

5.5.3 Potential contribution of the medial temporal region

The task employed in this study is fundamentally a free recall paradigm, and as such one might expect prominent activation of the medial temporal lobe. We did not see evidence of such activation in most subjects. We noted, however, that the two highest performing subjects did not have mesial temporal involvement of their epilepsy, and of these the one subject that had mesial temporal recordings did show significant activation of the mesial temporal region on task compared to rest. An additional subject was

recorded with a similar paradigm but fewer stimuli and demonstrated high performance in semantic but not phonemic verbal fluency. This was associated with increased high gamma activity in the left mesial temporal region (see supplemental data). Ad hoc analysis showed that this activity did not appear to vary substantially in the peri-utterance timeframe, but that the increase in high gamma activity was largely driven by speaking (as opposed to silent) periods of the recording, and that the activity returned to resting baseline levels between words. Other studies have also implicated hippocampal complex in language production tasks [212,247–250]. Most of these studies point to a role of the hippocampus in working memory necessary for maintaining contextual information for communication. Our observations, as well as those by Gleissner and Elger [250], suggest that in some people the hippocampus contributes to speech production independent of language context, and that inability to mount a functional gamma activity may underlie the impaired memory performance in epilepsy patients.

5.5.4 Toward a model of verbal fluency

Based on our findings, in combination with prior studies [222,226,239,251,252], we suggest a framework for understanding neurophysiologic processes underlying execution of the verbal fluency task (**Figure 5.5**). We propose that cognitive search processes occur nearly consistently throughout the task and employ distributed regions, most commonly prefrontal cortex. Phonemic (letter-motivated) and semantic (category-motivated) search employ overlapping, but not entirely equivalent networks that vary

across individuals. A periodic switch in search strategies is also dependent on frontal regions, although the precise localization (if one exists across subjects) is yet to be determined. When a suitable exemplar is identified, word planning processes occur by way of (possibly coordinated) activation of prefrontal cortex and superior temporal sulcus. This is followed by articulatory preparation, utilizing peri-Rolandic sensorimotor cortices bilaterally. Subsequent speech onset triggers auditory feedback processes in the posterior temporal and inferior parietal regions. We propose that lexical selection, articulatory preparation and auditory feedback occur in parallel with ongoing search activity in the prefrontal cortex, enabling identification and articulation of several exemplars in rapid succession.

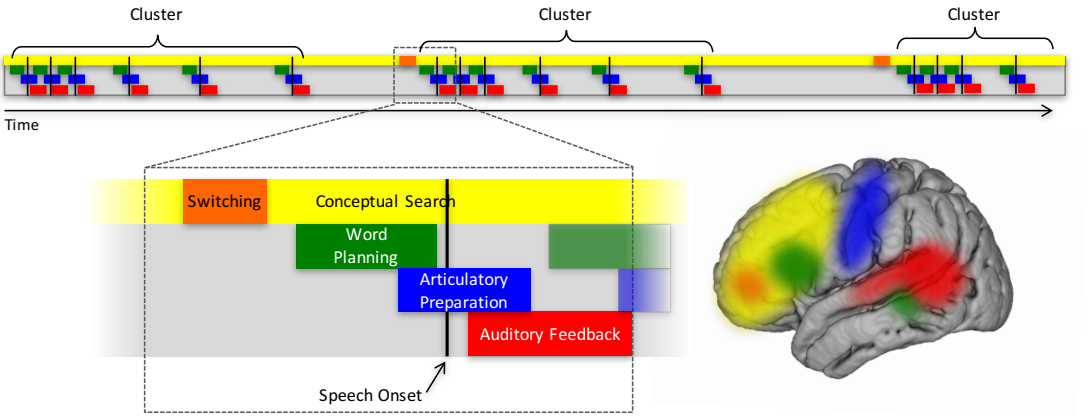

Figure 5.5: Proposed model for verbal fluency. Conceptual search processes occur on an ongoing basis and employ distributed areas including prefrontal cortex. Specific (but as yet undefined) frontal regions are likely involved in switching among subcategories for a given criterion/stimulus. Word planning may involve coordinated activity of prefrontal, inferior frontal, temporal and inferior parietal regions. Articulatory preparation occurs primarily in peri-Rolandic sensorimotor cortex. After speech onset, auditory feedback processing employs posterior superior temporal gyrus and inferior parietal regions. We propose that cognitive search processes are ongoing in parallel with lexical selection and speech production processes.

This model has several limitations and will most certainly be subject to revision as more is learned about the various sub-processes referenced above. For example, we have limited our model to neocortical activation patterns, and the impact of deeper structures (hippocampus, entorhinal cortex, insula etc.) is not addressed. Further, the question of whether lemma selection from a variety of competing concepts applies in both semantic and phonemic verbal fluency conditions has not been answered. However, our hope is to provide a framework for further discussion and refinement. Understanding the neurophysiologic processes contributing to verbal fluency will improve our interpretation of performance deficits seen in a spectrum of neurocognitive disorders affecting language and memory, and may offer new insights to potential therapeutic strategies.

5.5.5 Implications for invasive strategies to improve language function

Although currently envisioned devices for speech prostheses focus on enhancing function at the peripheral nerve and muscle coordination level, technology is being developed to replace or enhance cognitive functions related to memory and language production as well. These devices may address dysfunction in memory encoding and retrieval, lexical retrieval as well as phonological encoding and syllabification. Our findings suggest that successful implanted devices will require flexibility in their

architecture, at both a hardware and software level, and will need to be take on a form that allows for spatially distributed sampling.

5.5.6 Limitations

We studied spatiotemporal dynamics associated with verbal fluency in a small, consecutive, non-selected sample of patients. The size of our cohort, variable sampling of language networks (due to clinical necessity) and heterogeneity of brain pathology in our subjects are all limitations of this study. Prior studies demonstrate heterogeneity in functional language networks even among healthy normal subjects [225,227], and it makes sense that at least the same variability would be expected among patients with medically refractory epilepsy [236]. Additionally, spatial sampling in studies like ours is limited to structures where electrodes are implanted out of clinical necessity, which renders cross-subject comparisons difficult. Nonetheless, there are common themes that provide useful insight to the temporal dynamics of verbal fluency, such as early prefrontal activation, sensorimotor involvement in articulatory preparation and post-response temporoparietal activation. Further analyses using larger groups of patients may better explain our observations, place boundaries on the degree of individual variability in network architecture, and may even elucidate the differential effects of various types of epilepsy. Though electrocorticography experiments do not allow for a comparison to the general population, studies across a variety of seizure onset zone locations and underlying etiologies can improve signal to noise ratio and give insight to probable

mechanistic inferences. Additionally, modalities such as magnetoencephalography (MEG) may be of great utility here, provided that the brain regions to be sampled are close to the cortical surface and thus to MEG sensors. In these cases, comparison of patients with epilepsy and healthy normal controls, using similar language tasks, may be feasible.

Another contributor to noise in the spatiotemporal maps of this study is variability in timing across utterances. Changes in level of alertness or task engagement are known to affect variability and latency of reaction times [253]. In this study, we interpret our findings assuming the same overall timing of cognitive subprocesses related to word production for each subject, using prior findings in healthy normal subjects as a guide. However other studies utilizing high gamma activity have observed different reaction times across individuals and explored timing of activation patterns as a function of each subject's average reaction time. The free recall format of our paradigm limits our ability to formally assess a specific reaction time per se, although notably certain patterns of activation (e.g. post-response temporoparietal activity) appear relatively invariant. Nonetheless, it may be advantageous in future studies using similar formats to establish a baseline 'standard' average reaction time and 'normalize' temporal patterns to that standard for each individual subject.

The nature of our task paradigm did not allow systematic investigation of differences across letters or categories. Wang and colleagues [254] showed different electrocorticographic patterns in frequency and time domains for different categories in a

picture naming task and it is reasonable to expect such differences in category-based verbal fluency. This could be the subject of a further subanalysis, however it would likely be more successful with a larger number of subjects and possibly with repeated stimuli.

Several prior studies evaluating neurophysiologic signatures of verbal fluency utilize an automatic speech condition for comparison [217,222]. This technique could have provided more insight into the distinction between prefrontal search activity and the lexical selection subprocess. Further studies may be strengthened by including this third condition, as well as passive listening words, non-words and unexpected sounds to further dissect the auditory feedback processing activity in the posterior superior temporal region. Including these tasks was, however, outside the scope of the current study.

We make no assumptions regarding the contribution of clustering versus switching to the early prefrontal activation we observed. Given that we discarded utterances that were produced too closely together to be evaluated independently, our observations could represent predominantly search within a cluster or switching between clusters. To our knowledge there are currently no published studies investigating the timing of switching activities with regard to word clusters. We propose that a paradigm similar to the current study may provide an opportunity to clarify this.

5.5.7 Conclusions

In this study, we used high gamma activity on intracranial EEG to characterize the neuronal activation patterns associated with speech production in an overt, self-paced, letter- and category-motivated verbal fluency paradigm. The use of high gamma activity allows us to characterize human cognition with temporal resolution that exceeds functional MRI or PET, with good spatial resolution. Our approach differs from other iEEG studies in the nature of the language paradigm and in the self-paced nature of the task.

We observed high gamma increases in distributed prefrontal regions during the putative cognitive search timeframe, robust sensorimotor cortex increases during articulatory preparation and post-utterance temporoparietal activation consistent with auditory feedback processing. Our observations extend prior studies of stimulus-locked word generation with investigation of neuronal activation patterns associated with cognitive search. Variability in the differences between letter- and category-motivated verbal fluency likely reflects inter-individual heterogeneity in search strategies and conceptual representations. The underlying epileptic networks are almost certain to play a role and should not be ignored. Based on this work and others, we propose a model for the functional neuroanatomy of the verbal fluency task. We hope to thus contribute to the general understanding of this widely used but as yet incompletely understood neuropsychological evaluation tool.

5.6 Acknowledgements

This work was supported by NIH grants NS91006, NS080565, NS099348 and the Mirowski Family Foundation. Additionally, the authors would like to thank Jacqueline Boccanfuso for her help in IRB preparation and data conversion, as well as Drs. Nathan Crone, Robert Knight and Kathryn Davis for their advice and encouragement.

5.7 Supplementary Information

5.7.1 Detailed Description of Statistical Analyses

Analyses are done for each subject separately for each channel separately. For each stimulus we take a 2-second period of the EEG recording from 1250ms prior to 750ms after each response to that stimulus. We compute the high gamma activity (log-normalized to resting high gamma) at overlapping 200ms windows with 10ms steps in this period. We have multiple utterances for each stimulus and multiple stimuli (6 category stimuli and 6 letter stimuli). For the same stimulus type, category or letter, we aggregate across all utterances and stimuli to determine an average gamma activity at each of the 181 time points. Traces of this averaged activity over the 2-second period are demonstrated in figure 4. We consider activity to be significantly elevated above rest when the mean of the log-normalized activity is greater than 1.96 times the mean log of high gamma activity at rest in the same electrode. Although arbitrary, this threshold was used to correspond to the quantile of the normal distribution that has a two-sided probability in the tail of 5%.

To determine the times with respect to speech utterance onset at which individual electrodes show significant differences between high gamma activity for letter stimuli versus high gamma activity for category stimuli, we then selected four epochs within these 2-second periods and average the gamma activity in each of these four epochs. Epochs were selected based on prior literature to reflect timeframes relative to speech onset wherein salient language production processes are postulated to occur, without significant contribution of other processes:

- 600-850ms PRIOR TO speech onset for cognitive search
- 0-250ms PRIOR TO speech onset for word planning
- 0-250ms AFTER speech onset for articulatory motor activity, and
- 400-600ms AFTER speech onset for feedback processing

Now the unit of analysis is for each subject, for each electrode contact and for each epoch. If we focus on an epoch and electrode for a given subject, we then have two averages: one for the utterances corresponding to category and the other for the utterances corresponding to letter. We get an overall (two-sided) difference by taking the absolute value of the difference between these averages.

To get the reference distribution of the absolute difference we take all of the utterances in response to letters and all of utterances in response to categories. We randomly permute the labels of all of these utterances thereby keeping the number of utterances of each stimulus type the same but changing which utterances correspond to letters and which correspond to categories. We then, as with our original data, take the

averages of those that are letters and those that are categories and take the absolute value of this difference. This is done 10,000 times. Finally, we obtain a p-value (this is for each of the four epochs, for each of the electrode contacts and for each of the seven subjects) by identifying the fraction of the 10,000 permuted absolute values lie above the absolute value that we computed from the actual data.

The result is thus for each subject to have a p-value for each epoch and for each electrode contact. We focus on each epoch and hence have 6 P-values across the channels. We used an FDR to identify which channels of the 64 are significant. The resulting 28 FDR analyses (one for each of the seven individuals, one for each of the four blocks) is shown in Figure 5. The dots correspond to the electrodes that were found significant by this method. Even though the measure is two sided, we further distinguish the significant ones into those where the higher gamma activity is for letters (blue) and category (red).

We then wanted to see whether the extent to which electrodes met criteria for significant difference between phonemic and semantic conditions varied across the four epochs. Since the electrodes are the same across the 4 blocks, the data are paired and hence we used the Cochran's Q test. We labeled each electrode within each epoch as yes or no. We then calculated Cochran's Q for every subject to determine whether electrode activation patterns were consistent over the 2-second period. Low p-values allow us to reject the null hypothesis that letter/category differences are relatively stable at the electrode level from epoch to epoch.

5.7.2 Supplementary Figures

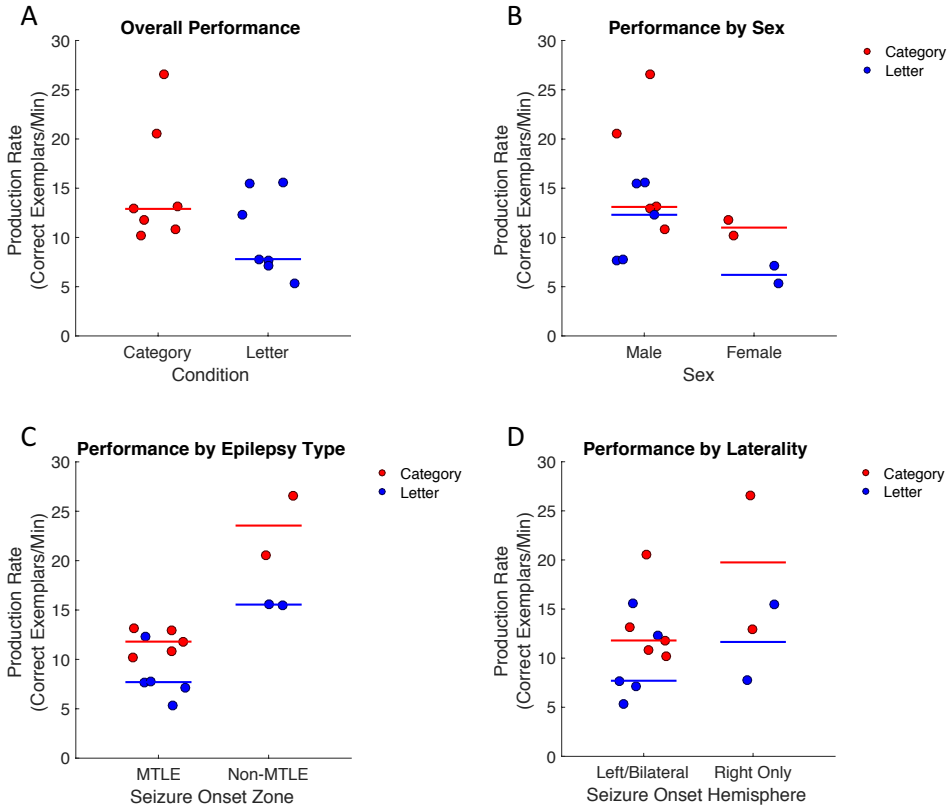

Supplementary Figure 5.1: Behavioral Task Performance. Behavioral performance metrics, as indicated by number of correct exemplars per 60 seconds. Phonemic production rates indicated by blue dots, semantic production rates by red dots. A. Overall production rates were lower in letter-motivated fluency ($p = 0.012$ by paired sample T-test) B. The two women in the study had generally lower production rates than the 5 men in both letter and category fluency. C. The two subjects without mesial temporal lobe involvement of their epilepsy had higher production rates than those others. D. There was no difference between performance of patients with epilepsy involving the left hemisphere and those without left hemisphere involvement. *MTLE: mesial temporal lobe epilepsy.*

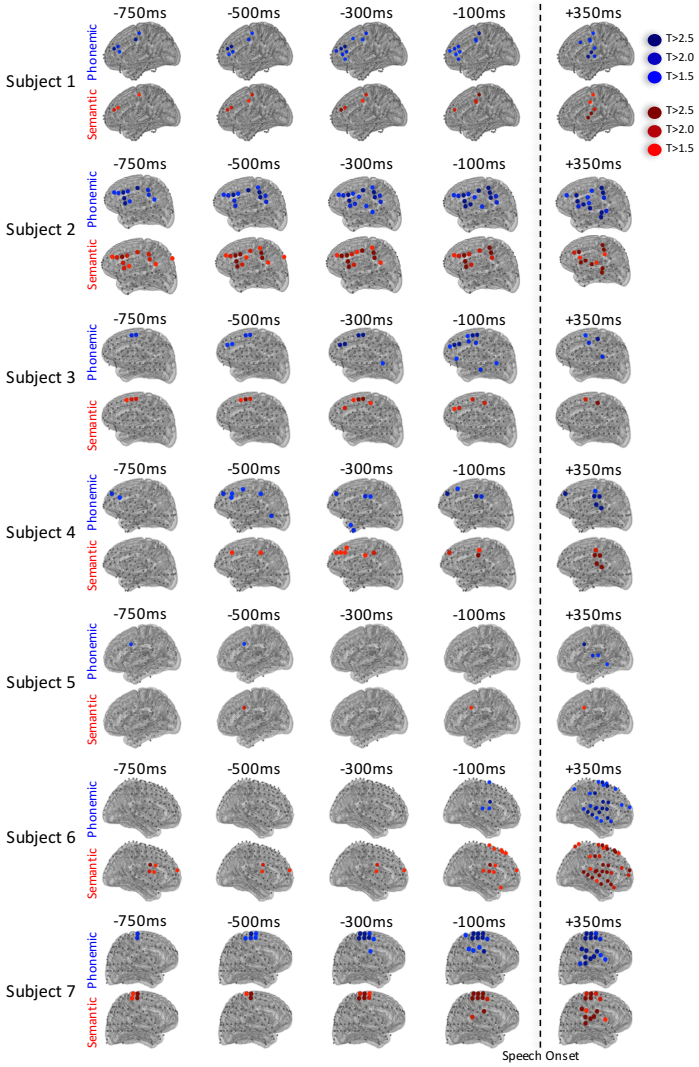

Supplementary Figure 5.2: Temporal progression of high gamma activity patterns (all subjects). Log-normalized high gamma activity patterns at selected time points for all subjects, averaged across exemplars for each condition. Light, medium and dark blue [red] tones indicate contacts where letter [category] fluency resulted in 1.5, 2.0 and greater than 2.5 times the high gamma recorded during rest. Speech onset was at 0ms (indicated by dashed line). Early activity was seen in prefrontal regions (this was not seen for phonemic verbal fluency in the two right hemispheric implants, nor was it seen for semantic verbal fluency in two of the five left hemispheric implants), with subsequent involvement of peri-Rolandic and temporal cortex. After speech onset, robust posterior temporal/inferior parietal activations were present in almost all subjects independent of laterality of recording.

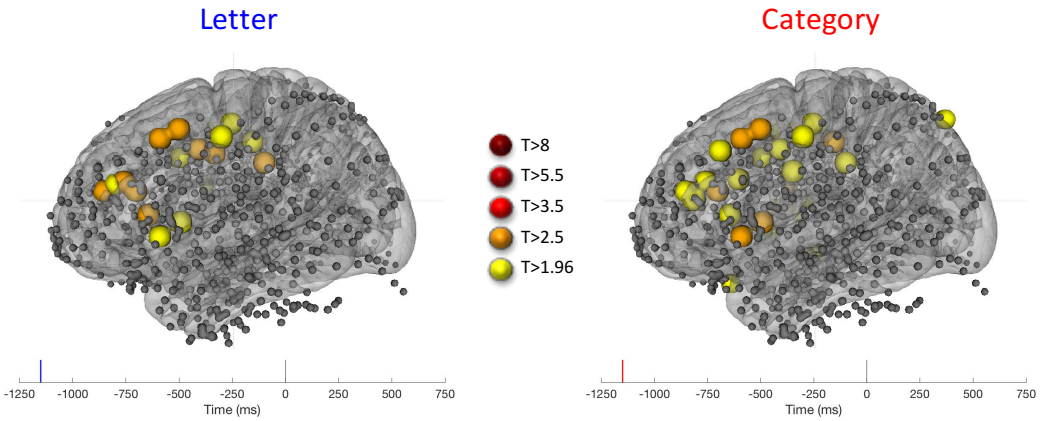

Supplementary Figure 5.3: Pooled high gamma activity patterns. Regions of significantly increased high gamma activity as a function of time for phonemic (letter-cued) and semantic (category-cued) verbal fluency utterances compared to rest, with electrode locations pooled across all subjects. Time 0ms indicates speech onset. Electrodes projected on standard MNI brain. Gray dots indicate electrodes where no significant increase in high gamma activity was observed. View videos online at https://drive.google.com/open?id=1UPHxJ3ssZgF5lNWBdbo72Em5gxtOneCM (Letter) and https://drive.google.com/open?id=1Qk9udgJU3MUC6f4OX7HgzM_gDgDjuPDp (Category).

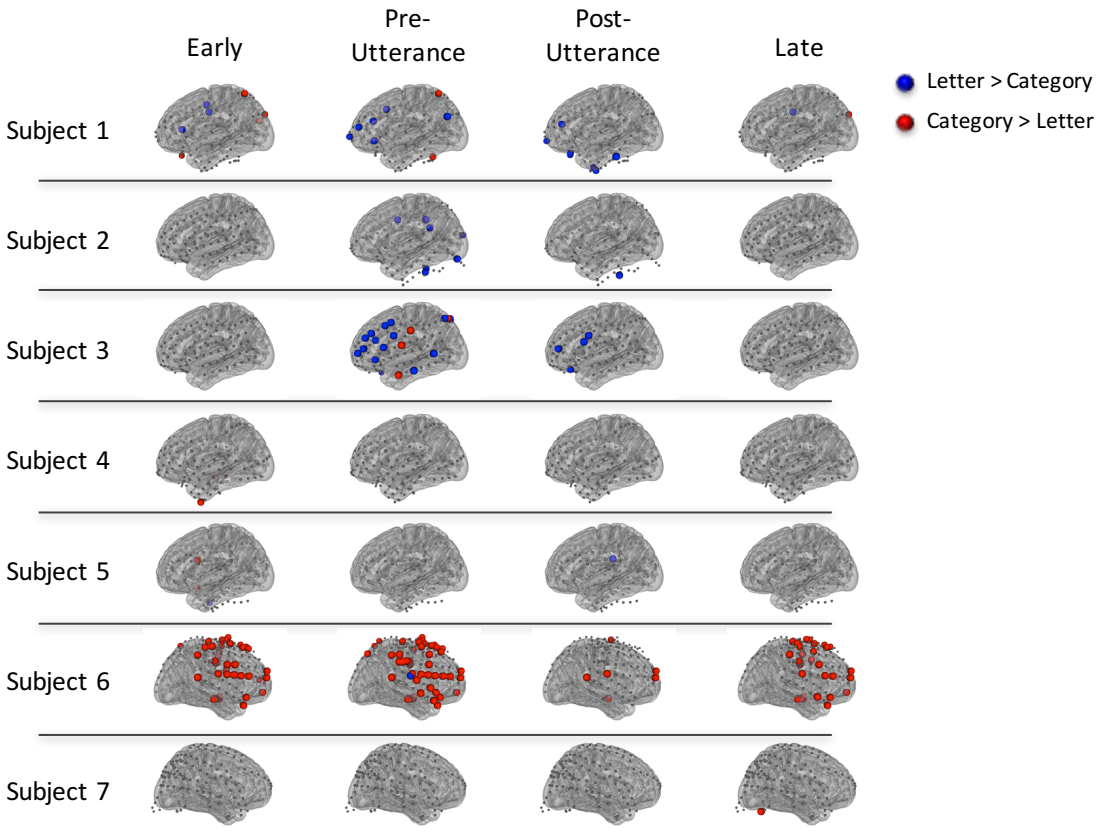

Supplementary Figure 5.4: Differences between letter and category verbal fluency across time. Electrodes with significant difference ($p<0.05$ by two-tailed permutation testing across conditions, corrected by false discovery rate across electrodes) between letter and category conditions for each subject during selected timeframes: Early (850ms to 600ms prior to utterance onset), Pre-Utterance (250ms to 0ms prior to utterance onset), Post-Utterance (0ms to 250ms after utterance onset) and Late (400ms to 600ms after utterance onset). Timeframes selected to coincide with the following periods of language processing: cognitive search, word planning, articulation and feedback. Blue dots indicate contacts where high gamma activity for letter-motivated utterances exceeded that for category-motivated utterances, red dots indicate the inverse. See supplementary text for details of statistical analysis. We found a broad range of patterns among the subjects studied, with evidence of semantic vs phonemic differences appearing in both hemispheres and during search, word planning, articulatory execution as well as auditory feedback timeframes. The two subjects without mesial temporal involvement (subject 3 and subject 6) demonstrated the largest disparity in letter-motivated and category-motivated fluency.

Chapter 6: Using intracranial EEG to localize epileptic networks

In this chapter, I explore the utility of interictal iEEG recordings in localizing epileptic networks, using data from drug-resistant patients who underwent surgical resection. By integrating iEEG network analysis with data from structural MRI and clinical reports, I characterize network connectivity inside and outside of the resected tissue in good and poor outcome patients. Extracting valuable information from interictal iEEG can ultimately reduce the need for prolonged implant times, thereby reducing patient morbidity.

Reference: Shah P, Bernabei J, Kini L, Ashourvan A, Bassett DS, Davis KA, Litt B. High interictal connectivity within resection zone is associated with favorable post-surgical outcomes in focal epilepsy patients. *Prepared for submission to Annals of Neurology.*

6.1 Abstract

Drug-resistant focal epilepsy patients are often candidates for surgical resection of epileptic brain regions. Accurate localization of these regions is necessary for post-surgical seizure freedom. While intracranial electroencephalography (iEEG) is the gold standard for localizing seizure networks, there is a clinical need for quantitative tools to maximize information gained from iEEG data while minimizing implant times and patient morbidity. To help achieve this goal, we evaluate the utility of interictal iEEG network analysis in identifying targets for surgical removal. We analyze interictal iEEG recordings and neuroimaging from 27 focal epilepsy patients treated via surgical resection. We generate interictal functional networks by calculating pairwise correlation of iEEG signals across different frequency bands. Using image coregistration and segmentation, we identify electrodes falling within the surgically resected tissue (i.e. resection zone), and compute connectivity metrics in relation to the resection zone. We further associate these metrics with post-surgical outcomes. Greater overlap between resected electrodes and highly synchronous electrodes is associated with favorable post-surgical outcomes. Furthermore, good outcome patients have significantly higher connectivity within the resection zone compared with poor outcome patients. This study suggests that spatially-informed interictal network synchrony measures can distinguish between good and poor outcomes. By capturing clinically relevant information during interictal periods, our work can ultimately reduce the need for prolonged invasive implants and provide fundamental insights into the pathology of an epileptic brain.

6.2 Introduction

Epilepsy is a common neurological disorder which affects over 50 million people worldwide [255]. Over one-third of epilepsy patients experience uncontrolled seizures despite medication [5]. Within this group, approximately 80% have localization-related epilepsy and are candidates for surgical removal of the seizure-generating region in the brain [256]. Accurate seizure localization is needed in these patients to maximize chances of seizure freedom and minimize memory deficits following surgery. With the recent development of more targeted alternatives to surgery such as laser ablation [1] and neurostimulation [2], precise localization is becoming increasingly valuable for guiding therapy.

Intracranial EEG (iEEG) can be incredibly valuable for localizing seizures, particularly in patients without clear lesions on clinical imaging [257]. In this approach, implanted subdural and depth electrodes record brain signals for up to several weeks, with the intent of capturing ictal events and identifying seizure onset regions. While iEEG is the gold standard for recording seizures at high spatial and temporal resolution, it has important limitations. For example, seizures are often provoked during the recording period via medication withdrawal and sleep deprivation; these provoked seizures may be fundamentally different than patients' stereotypical spontaneous seizures and could misinform localization attempts. Additionally, prolonged implantation and seizure provocation can lead to complications such as infection or hemorrhage. In some cases, seizures may not occur during the implant period, rendering the study inconclusive.

Clearly, there is a clinical need for reliable tools to map seizure networks while minimizing morbidity to the patient.

Recent evidence shows that seizures most commonly arise from abnormal brain networks rather than isolated focal lesions [14,258]. Therefore, in order to accurately map seizure networks, it is important to identify brain network abnormalities in epilepsy. Functional networks derived from correlations between iEEG signals show promise in highlighting seizure onset networks, distinguishing between focal and generalized seizures, and predicting outcomes [139,259,260]. While most previous iEEG network studies analyze ictal and preictal data, it is likely that interictal recordings are also informative for localizing epileptic networks. This notion is supported by recent studies demonstrating that ictal and interictal iEEG network subgraphs are topologically similar, and that patterns of high frequency activity propagation during seizures are recapitulated interictally [25,26]. Moreover, epileptic brain networks are fundamentally altered, as reflected by cognitive deficits and imaging abnormalities in many patients. These findings suggest that iEEG can provide valuable information without the need to capture seizure events.

In this study, we evaluate the utility of interictal network analysis in mapping seizure networks. While the ground truth identity of the seizure-generating network is inherently unknown, information about the surgical resection zone combined with outcome data can serve as a valuable proxy. Namely, if a patient has a good post-surgical outcome, a reasonable assumption is that the seizure network is contained in the resection zone; in

contrast, in poor outcome patients, the resection zone likely did not include the entirety or the seizure network. Therefore, we characterize network connectivity inside and outside of the resection zone in good and poor outcome patients. We hypothesize that patients with highly synchronous nodes removed are more likely to have good outcomes. This work can further our understanding of functional network topology in epileptic human brains, and ultimately reduce the need for prolonged implant times, thereby reducing patient morbidity.

6.3 Methods

6.3.1 Subjects

We retrospectively studied 27 adult patients undergoing pre-surgical evaluation for drug-resistant epilepsy at the Hospital of the University of Pennsylvania and the Mayo Clinic. All patients presented with focal onset seizures and were subsequent treated via surgical resection, with at least 1 year post-surgical outcomes as measured by Engel classification score and/or ILAE criteria. Patients were divided into good outcome (Engel I, or ILAE 1-2) and poor outcome (Engel II-IV or ILAE 3-6) groups. All patients gave consent to have their anonymized iEEG data publicly available on the International Epilepsy Electrophysiology Portal (www.ieeg.org) [261,262]. Clinical and demographic information is available in **Table 6.1**.

Subject	Age	Sex	Resected Region	Pathology	Outcome
1	21	M	LFL	MCD	Engel 1D
2	37	M	RTL	Dual Pathology	Engel 1B
3	28	F	RTL	MTS	Engel 1A
4	33	M	LFPL	MCD	Engel 1B
5	40	M	RFL	MCD	Engel 1C
6	25	F	LTL	Dual Pathology	Engel 1A
7	57	F	LTL	MTS	Engel 2D
8	54	M	LTL	MTS	Engel 2A
9	41	F	LTL	Gliosis	Engel 2B
10	56	F	RTL	MTS	Engel 1A
11	29	M	LPL	Not Available	Engel 2A
12	25	F	LTL	Gliosis	Engel 1C
13	24	M	LFL	Tumor/Vascular/Infection	Engel 1D
14	35	F	LTL	MTS	Engel 1D
15	48	F	RTL	Gliosis	Engel 1B
16	39	M	RTL	Tumor/Vascular/Infection	Engel 1A
17	45	F	LTL	MTS	Engel 1B
18	36	M	RTL	MTS	Engel 1A
19	40	F	RTL	MTS	Engel 1B
20	N/A	M	RFL	Gliosis	ILAE1
21	N/A	F	RFTL	Gliosis	ILAE4
22	N/A	M	RTL	N/A	ILAE4
23	N/A	M	LTL	Gliosis	ILAE5
24	N/A	M	RFL	Gliosis	ILAE5
25	N/A	F	LTL	Gliosis	ILAE5
26	N/A	M	LFPL	Gliosis	ILAE4
27	N/A	F	RTL	Gliosis	ILAE5

Table 6.1: Clinical and demographic patient information. Legend - L: Left; R: Right; TL: Temporal Lobe; FL: frontal lobe, FPL: fronto-parietal lobe, MTS: mesial temporal sclerosis; MCD: malformation of cortical development; N/A: not available

6.3.2 Intracranial EEG acquisition

Cortical surface and depth electrodes were implanted in patients based on clinical necessity. Electrode configurations (Ad Tech Medical Instruments, Racine, WI) consisted of linear cortical strips and two-dimensional cortical grid arrays (2.3 mm diameter with 10 mm inter-contact spacing), and linear depths (1.1 mm diameter with 10 mm inter-contact spacing). Continuous iEEG signals were obtained for the duration of each patient's stay in the epilepsy monitoring unit. For each subject, we obtained one clip of interictal data consisting of the first 6 hours of artifact-free recording at least 4 hours removed from any seizure event. Seizure events were determined by a board-certified epileptologist and consistent with clinical documentation.

6.3.3 Electrode and resection zone localization

Structural MRI scans were obtained from each patient three time points: pre-implant, post-implant, and post-resection. MRI data were collected on a 3T Siemens Magnetom Trio scanner (Siemens, Erlangen, Germany) using a 32-channel phased-array head coil. High-resolution anatomical images were acquired using a magnetization prepared rapid gradient-echo (MPRAGE) T1-weighted sequence (TR = 1810 ms, TE = 3.51 ms, flip angle = 9°, field of view = 240 mm, resolution = $0.94 \times 0.94 \times 1.0$ mm^3). Spiral CT images (Siemens, Erlangen, Germany) were obtained clinically for the purposes of electrode localization. Both bone and tissue windows were obtained (120 KV, 300 mA, axial slice thickness = 1.0 mm).

Electrodes were identified via thresholding of the CT image and labeled using a

semi-automated process. For all subjects, all images were registered to the pre-implant MRI space using 3D rigid affine registration, with mutual information as the similarity metric. Pre-implant MR images were diffeomorphically co-registered to post-resection MR images to identify the resection zone. Resection zones were segmented semi–automatically via the ITK-SNAP random forest classifier feature after hand-drawn training samples were provided on co-registered imaging (Kini et al., 2018, unpublished). The resection zone was dilated by 5% of the iEEG network in order to mimic effects of gliosis and scarring adjacent to surgically removed tissue [263]. All resection estimates were confirmed by a board-certified neuroradiologist. Using these resected regions along with the electrode localizations, we determined the identities of the electrodes present in the resection zone. Co-registration steps utilized Advanced Normalization Tools (ANTS) software [122,264].

6.3.4 Functional network analysis

Following removal of artifact-ridden electrodes, interictal iEEG clips were common-average referenced to reduce potential sources of correlated noise.[265] Next, each clip was divided into 1 s non-overlapping time windows in accordance with previous studies[139,26,266,267]. To generate a functional network representing broadband functional interactions between iEEG signals for each 1 s time window, we employed a method described in detail previously [26]. Namely, signals were notch-filtered at 60 Hz to remove power line noise, low-pass and high-pass filtered at 115 Hz and 5 Hz to account for noise and drift, and pre-whitened using a first-order

autoregressive model to account for slow dynamics. Functional networks were then generated by applying a normalized cross-correlation function ρ between the signals of each pair of electrodes within each time window. Next, to gain an understanding of iEEG networks across different frequencies, we generated functional networks across physiologically relevant frequency bands as described in detail in a previous study [139]. Specifically, multitaper coherence estimation was used to compute functional coherence networks for each 1 s window across four frequency bands: α/θ (5-15 Hz), β (15-25 Hz), low-γ (30-40 Hz), and high-γ (95-105 Hz). Both broadband and frequency-specific networks were represented as full-weighted adjacency matrices. In this model, each electrode serves as a node of the network, and connectivity between pairs of electrodes serve as edges. The networks were averaged across the full 6 hours to obtain one function network for each patient for each frequency band. A schematic of this pipeline is illustrated in **Figure 6.1**.

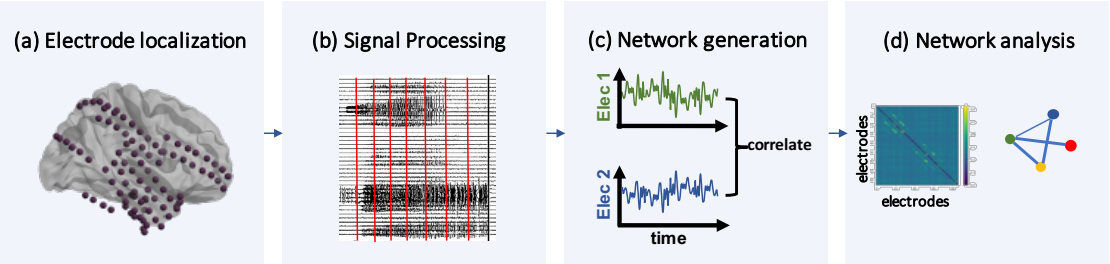

Figure 6.1: Schematic of subject-level iEEG network analysis pipeline. **(A)** Using structural imaging, we identify the location of electrodes on the brain surface and depths. **(B)** We process interictal iEEG signals and divide them into 1 s windows. **(C)** For each 1 s window, we generate a broadband functional connectivity network by computing correlation between iEEG signals across electrode pairs. We similarly compute frequency-specific networks using coherence between iEEG signals across electrode pairs. **(D)** We carry out node-level and edge-level network analysis on these resulting networks, in relation to the resection zone.

To quantify the degree of synchrony of each node in the network, we computed the nodal strength, which is defined for each node as the sum of the weights of all edges connected to that node [17,96]. We identified "highly synchronous nodes" as nodes with a strength at least 1 z-score above the mean. Next, we defined the *strength selectivity* of the resection zone (RZ) as the spatial overlap between the nodes within the resection zone and the highly synchronous nodes. Overlap was computed using the Dice Similarity Coefficient (DSC) which ranges from 0 to 1 and is defined as $DSC(A,B) = \frac{2\,|A \cap B|}{|A|+|B|}$, where A and B are two binary sets. We compared the strength selectivity for good and poor outcome patients across all frequency bands, and repeated the analysis for z thresholds ranging from 0 to 2. Furthermore, to assess what types of connections were contributing to the observed differences in strength selectivity in good vs. poor outcome patients, we

delineated the following three edge types: (i) connections between nodes within the RZ (RZ-RZ), (ii) connections between one node within the RZ and one node outside the RZ (RZ-OUT), and (iii) connections between nodes outside the RZ (OUT-OUT). For each subject, we computed the mean edge weights within each of these categories. We compared the mean edge weights between these three categories within both good and poor outcome patients. Furthermore, we computed differences in these categories between the two patient groups.

Given that neighboring electrodes are more likely to be highly correlated due to spatial proximity or due to common source measurements, we generated a spatially-constrained null model to ensure our findings were not a result of chance. To do this, for each patient with N resected electrodes, we sampled clusters of N spatially contiguous electrodes, using Euclidean distance to determine the closest electrodes. We repeated our edge-weight analysis after normalizing the RZ-RZ, RZ-OUT and OUT-OUT edge weights by the null distribution of edge weights for each category. Normalization was carried out by subtracting the mean and dividing by the standard deviation of the null values. Non-parametric Mann-Whitney U-tests were used for all pairwise comparisons in this study.

6.4 Results

We constructed spatial maps of nodal strength, along with the overlaid resection zone, for each individual patient (**Figure 6.2**). At the group level, we observed

significantly higher broadband and beta strength selectivity in good outcome patients vs. poor outcome patients, using a z threshold of 1 ($p < 0.05$, Mann-Whitney U test) (**Figure 6.3A**). Sweeping across a range of z thresholds from 0 to 2 revealed a trend of higher strength selectivity in good vs. poor outcome patients in all frequency bands, with significant differences for broadband ($z = 1$), beta band ($z = 0.5$ to $z = 1.25$) and low-gamma band ($z = 1.75$ to $z = 2$) (**Figure 6.3B**).

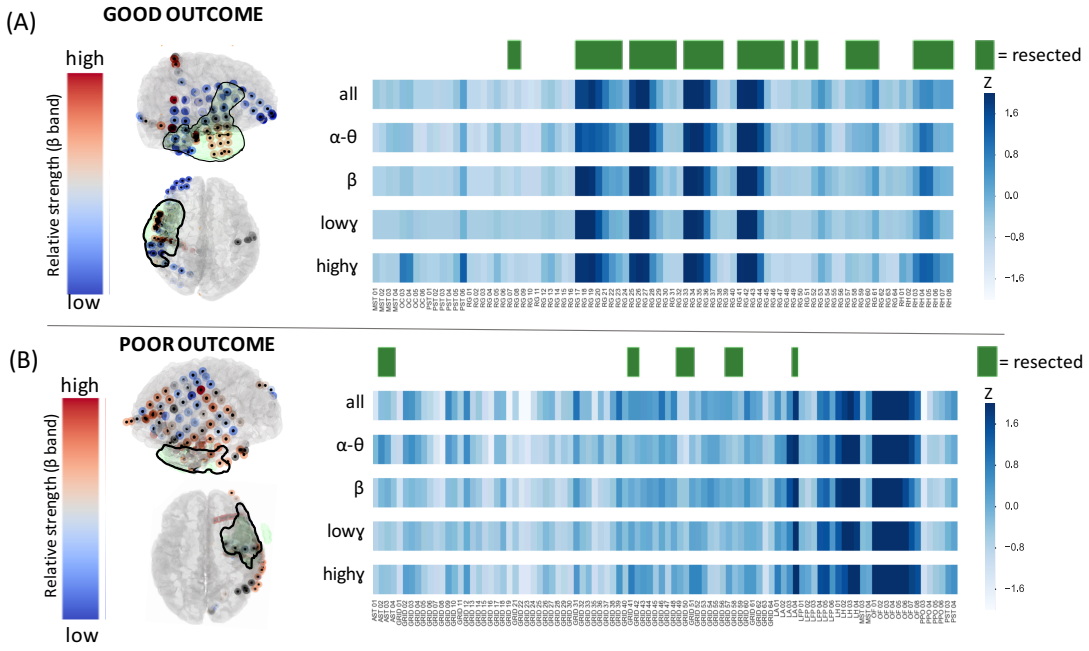

Figure 6.2: Patient-level strength selectivity analysis. For an example good outcome patient **(A)** and poor outcome patient **(B)**, we illustrate spatial maps of nodal strength (in the beta band), along with corresponding 2D heat maps of nodal strength in all frequency bands. Resection zones are highlighted in green.

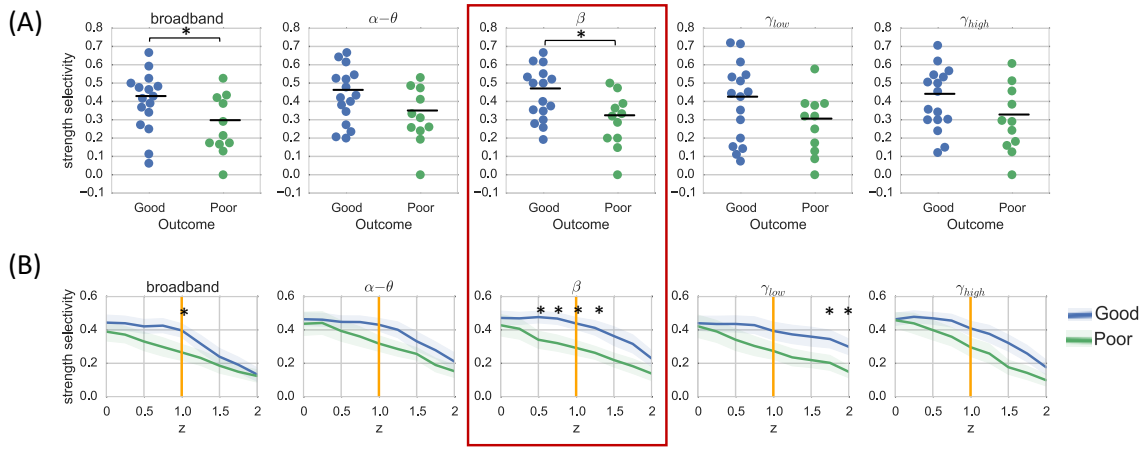

Figure 6.3: Group-level strength selectivity analysis. **(A)** Strength selectivity in all tested frequency bands with a *z* threshold of 1 reveals significantly higher broadband and beta strength selectivity in good outcome patients vs. poor outcome patients. (B) Sweep across multiple *z* thresholds from 0 to 2 reveals significant outcome-dependent differences in strength selectivity for broadband (z=1), beta band (z=0.5 to z=1.25) and low-gamma (z = 1.75 to z=2) networks (mean +/- standard error). Beta band strength selectivity distinguishes between good and poor outcome across the widest range of *z* thresholds (red box). *$p < 0.05$, Mann-Whitney *U* test.

Next, we sought to understand whether observed strength selectivity findings were due to connectivity within the resection zone, or connectivity between the resection zone and extra-resection regions. Since strength selectivity findings were most prominent in the beta band, we focused our edge-level analysis on the beta band networks, but repeated the analysis across all bands. We found that connections within the resection zone (RZ-RZ) were significantly stronger than RZ-OUT and OUT-OUT connections, and RZ-RZ connections were stronger in good outcome patients compared with poor outcome patients ($p < 0.05$) (**Figure 6.4**). These findings persisted across all frequency bands ($p < 0.05$). After normalization by a spatially-constrained null model, RZ-RZ connections were still significantly stronger in good outcome patients than poor

outcome patients ($p < 0.05$). While this trend was present in all frequency bands, it was statistically significant for beta, low-gamma, and high-gamma bands. Additionally, in both good and poor outcome patients, normalized RZ-RZ connections were stronger than RZ-OUT connections and RZ-OUT connections were stronger than OUT-OUT connections, with the additional finding of RZ-RZ > RZ-OUT in good outcome patients ($p < 0.05$). These findings also persisted across all frequency bands.

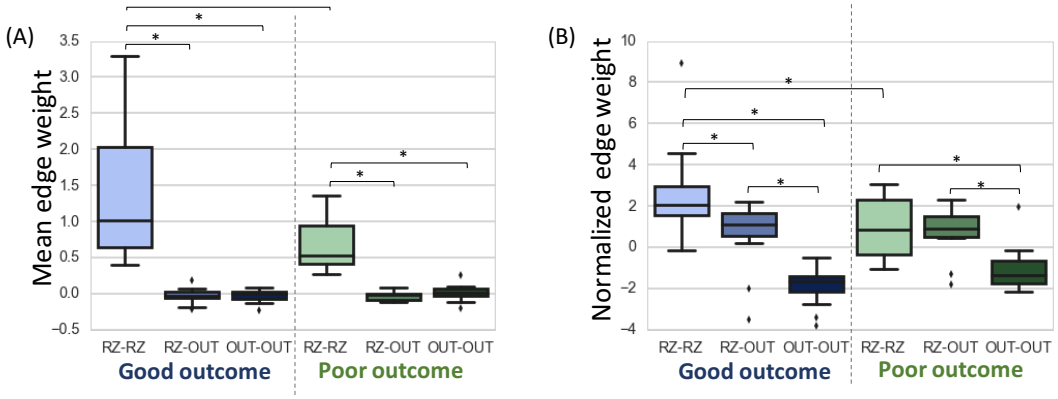

Figure 6.4: Edge-level analysis in relation to resection zone, shown for the beta band. (A) Connections within the resection zone (RZ-RZ) are significantly stronger than RZ-OUT and OUT-OUT connections, and RZ-RZ connections are stronger in good outcome patients compared with poor outcome patients. (B) After normalization by a spatially-constrained null model, RZ-RZ connections still significantly stronger in good outcome patients than poor outcome patients. Additionally, in both good and poor outcome patients, normalized RZ-RZ connections are stronger than RZ-OUT connections and RZ-OUT connections are stronger than OUT-OUT connections, with the additional finding of RZ-RZ > RZ-OUT in good outcome patients. *$p < 0.05$, Mann-Whitney *U* test.

Given similar findings across different frequency bands, we sought to directly probe the similarity of the frequency-specific function networks. Therefore, we correlated the edges of the mean functional networks for each pair of frequency bands, across all subjects. We found a high degree correlations across these networks (r=0.75-0.91), with

the highest correlations between neighboring frequency bands (e.g., alpha-theta vs. beta: r=0.91), and the lowest correlations between bands with larger frequency separation (e.g., alpha-theta vs. beta: r=0.75) (**Figure 6.5**).

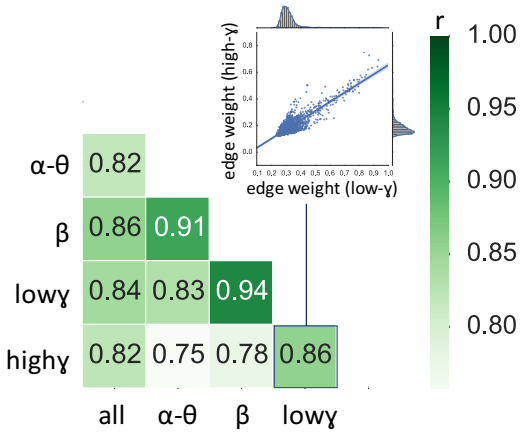

Figure 6.5: Matrix of similarity values between functional networks generated using different frequency bands. Similarity values were obtained by measuring Pearson correlation between edges in each pair of networks for each subject, and subsequently averaging these correlations across subjects. We observe strong correlations across all pairs of networks (r=0.75-0.91), with the highest correlations between neighboring frequency bands and the lowest correlations between bands with larger frequency separation. Inset shows an example scatter plot and correlation line of low-gamma edge weights vs high-gamma edge weights in one subject.

6.5 Discussion

In this study, we evaluated the association of interictal network synchrony within the resection zone on post-surgical outcomes in adult patients with drug-resistant focal epilepsy. We determined that high interictal strength selectivity is associated with better outcomes. This effect appeared to be driven by connectivity within the resection zone. Our findings suggest that interictal recordings can provide valuable information to identify putative seizure-generating regions. Employing quantitative tools on early

interictal recordings can maximize information gained from iEEG recordings while significantly reducing recording times.

6.5.1 High interictal connectivity within resection zone is associated with good outcomes

We defined the strength selectivity of the resection zone as a simple measure of overlap between electrodes in the resected region and highly synchronous electrodes as measured by *z*-scored node strength. We found that strength selectivity was higher in good outcome patients vs. poor outcome patients. The notion that removal of highly synchronous nodes would lead to favorable outcomes is consistent with our understanding that epilepsy is characterized by abnormal hypersynchronous neuronal firing [268]. Our findings contribute to a growing body of recent work aiming to identify epileptogenic networks and predicting outcomes based on node-level measures [259,269–274]. While most of this prior work uses ictal or pre-ictal recordings, we focused on deriving information from the earliest available interictal data. Moreover, unlike the majority of previous studies, we applied quantitative imaging methods and semi-automated segmentation techniques to delineate the resection cavity, rather than utilizing subjective clinical identification of electrodes that were resected or involved in seizure onset. Finally, we demonstrated the utility of our method using the simple, parameter-free metric of node strength, and explored our findings across a range of physiologically relevant frequency bands.

Although we observed a trend of increased strength selectivity in good outcome patients across a range of *z* thresholds using both broadband and frequency specific networks, the finding was mostly significant using beta band networks. While beta frequency oscillations are thought to be associated with long-range communication between brain regions [275], the role of oscillatory activity across different frequency bands is still complex, with known interactions between different frequencies [197,276,277]. Moreover, our direct analysis of network similarity across frequency bands indicated that the frequency-specific networks were highly correlated with each other. The high similarity may be due to our processing pipeline. Namely, we computed average networks across 6 hour periods, since we were interested in extracting information from stable functional networks. Kramer and coworkers have shown that while functional iEEG networks are highly variable on the order of seconds, stable network topology emerges after as little as 100 seconds, and persist across frequency bands [278]. Additionally, our group has previously shown that long-term interictal functional network connectivity, across all frequencies, can accurately predict structural connectivity derived from white matter tractography (Ashourvan et al., 2018, unpublished). Therefore, it is possible that long-term interictal functional networks are highly similar across different frequency because these networks converge to a representation of the underlying structural connectome.

Our edge-level analysis revealed that the majority of network synchrony is attributable to intra-resection connections. This finding is similar to previous analyses

illustrating that connectivity within the seizure onset zone is higher than both connectivity outside of the seizure onset zone and connectivity bridging seizure onset and non-seizure onset regions [267,279,280]. Our study examines connectivity within the resection zone, rather than the clinically identified seizure onset zone, and provides further validation using post-surgical outcomes. Of note, we found higher intra-resection zone connectivity in good vs. poor outcome patients. These analyses suggest that seizure-generating regions are functionally isolated from surrounding brain regions in focal epilepsy patients, and that removal of these functionally isolated regions improves patients' chances of a successful outcome.

Our finding that good outcome patients had higher intra-resection zone connectivity than poor outcome patients persisted following normalization by a spatially-constrained null model. Previous similar studies have generated null distributions by sampling N random electrodes from the network, where N is the number of electrodes in the region of interest (e.g. the resection zone) [269,272]. However, these models do not consider two key facts: (1) that neighboring electrodes are more likely to have higher functional connectivity due to structural connections or common source signals, and (2) that surgical practice necessitates removal of spatially contiguous brain regions rather than distant, randomly distributed electrodes. Our spatially constrained null model therefore provides a more realistic set of random resections with which to normalize our connectivity findings. Since this spatially-constrained null is more stringent than a

random resection-based null, it is likely that our intra-resection connectivity findings are truly significant and not simply due to spatial proximity.

6.5.2 Methodological Considerations and Limitations

One concern inherent to all iEEG data analysis is that the entire brain is not sampled, as electrode locations are based on clinical necessity. While spatial coverage is sparse to minimize patient morbidity, electrodes are placed with the intent of capturing regions hypothesized to be part of the seizure network. Therefore, the seizure network should still be captured, particularly in patients with good outcomes. However, it is possible that the seizure network is not adequately covered, particularly in poor outcome patients. Moreover, the spatial distribution and number of nodes in the network may impact the topological properties derived from the network. Recent efforts to map whole-brain iEEG may help circumvent this issue [281–283]. Furthermore, scalp EEG or MEG recordings, as well as data from functional and structural neuroimaging such as MRI and PET, could complement our intracranial analysis and allow for spatial sampling of the whole brain.

Another limitation of this study is that the resection cavity may include more than what was necessary to resect. For example, patients with temporal lobe epilepsy often have a stereotyped anterior temporal lobectomy procedure entailing removal of both temporal neocortex and mesial temporal structures, even if only one of those areas is involved in the epileptic network. Therefore, further validation of our approach will be

carried out utilizing data from patients with laser ablations, which target a smaller region of tissue.

We demonstrated a framework for mapping interictal functional networks using simple measures of network synchrony on a moderately sized dataset. In order to bring this framework to clinical practice, the next step is to generate a suite of multimodal network-based features and assess the ability of these features to predict candidate targets for surgical removal, using large multi-institutional datasets. By sharing our data, code, and analysis approach, we hope to facilitate translation of quantitative seizure mapping tools to clinical practice.

6.5.3 Conclusion

We determined that high interictal connectivity within the resection zone is associated with favorable post-surgical outcomes in drug-resistant focal epilepsy patients. Ultimately, our study can be translated to clinical practice, allowing for automated and optimized seizure localization with reduced need for prolonged invasive implants.

7. Acknowledgements

This work was supported by National Institutes of Health grants 1R01NS099348 and K23-NS073801. We also acknowledge support by the Thornton Foundation, the Mirowski Family Foundation, the ISI Foundation, the John D. and Catherine T. MacArthur Foundation, the Sloan Foundation, and the Paul Allen Foundation.

Chapter 7: Merging neuroimaging and electrophysiology

In this chapter, I develop a pipeline to facilitate combined analysis of MRI and iEEG. Methods which merge data from neuroimaging and electrophysiology can help us better understand the relationship between the structural and functional epileptic networks. In order to probe brain connectivity as directly as possible at the highest resolution, I utilize high angular resolution diffusion MRI (HARDI) to derive structural connectivity networks, and iEEG to derive functional connectivity networks. I characterize relationships between these two modalities across time, frequency, and space. Specifically, I quantify structure-function coupling during seizure evolution and identify structural connections contributing to this coupling.

Reference: Shah, P, Ashourvan A, Mikhail F, Pines A, Kini L, Shinohara RT, Bassett DS, Litt B, and Davis KA. Local structural connectivity directs seizure spread in focal epilepsy. bioRxiv (2018): 406793. *Under Review* at *Brain*

7.1 Abstract

How does the human brain's structural scaffold give rise to its intricate functional dynamics? This is a central challenge in translational neuroscience, particularly in epilepsy, a disorder that affects over 50 million people worldwide. Treatment for medication-resistant focal epilepsy is often structural – through surgery, devices or focal laser ablation – but structural targets, particularly in patients without clear lesions, are largely based on functional mapping via intracranial EEG (iEEG). Unfortunately, the relationship between structural and functional connectivity in the seizing brain is poorly understood. In this study, we quantify structure-function coupling across preictal and ictal periods in 45 seizures from 9 patients with unilateral drug-resistant focal epilepsy. We use High Angular Resolution Diffusion Imaging (HARDI) tractography to construct structural connectivity networks and correlate these networks with time-varying broadband and frequency-specific functional networks derived from coregistered iEEG. Across all frequency bands, we find significant increases in structure-function coupling from preictal to ictal periods. We demonstrate that short-range structural connections are primarily responsible for this increase in coupling. Finally, we find that spatiotemporal patterns of structure-function coupling are stereotyped, and a function of each patient's individual anatomy. These results suggest that seizures harness the underlying structural connectome as they propagate. The relationship between structural and functional connectivity in epilepsy may inform current and new therapies to map and alter seizure spread, and pave the way for better-targeted, patient-specific interventions.

7.2 Introduction

Epilepsy is a neurological disorder characterized by recurrent, unprovoked seizures. It affects over 50 million people worldwide [255] and will afflict approximately 1 in 26 people during their lifetime [284]. The most common subtype is *focal* or localization-related epilepsy, in which seizures arise from a specific region in the brain [7]. Patients with localization-related epilepsy often experience uncontrolled seizures despite medication, leading to neurological and psychiatric co-morbidities, deterioration in quality of life, and up to an eleven-fold increase in mortality rate [4,6].

Recent evidence shows that seizures most commonly arise from abnormal brain networks rather than isolated focal lesions [14,258]. As a result, researchers are applying graph theoretical methods from the rapidly growing field of network neuroscience to identify brain network abnormalities in epilepsy, in the hope of finding targets for therapeutic interventions. In this approach, investigators map whole-brain structural and functional networks, or "connectomes", by characterizing connectivity between brain regions based on multi-modal neuroimaging data [16,17,96]. Structural brain networks are most commonly derived from diffusion tensor imaging (DTI) tractography [19]. Functional brain networks are most commonly derived from correlations in signal fluctuations across multiple recording sites from modalities such as resting state functional MRI (fMRI) [285,286], magnetoencephalography (MEG) [287], and electroencephalography (EEG) [288]. These approaches reveal a wide variety of network disruptions in epilepsy patients, both structurally [289–291] and functionally

[20,162,292]. While still nascent, this work shows promise for clinical applications, as network-based measures may serve as biomarkers for predicting seizure onset and spread [139,270,293,294], cognitive impairments [291,295], and outcome following surgical therapy [259,269,272].

Most studies of epileptic networks focus solely on either structural or functional connectivity. However, it is commonly understood that the two are tightly linked. In fact, there is great interest in the neuroscience community in elucidating the relationship between brain structure and function. Recent evidence shows that structural and functional brain networks are correlated at multiple temporal and spatial scales, that structural connectivity constrains functional connectivity, and that functional connectivity can modulate structural connectivity via mechanisms of plasticity [116,117,132,296–303].

Given the robust coupling between structure and function in healthy brains, disruptions in structure-function coupling can serve as biomarkers of neurological disease, including in epilepsy. For example, Zhang et al. (2011) report that the degree of coupling between resting state fMRI networks and DTI tractography networks is lower in idiopathic generalized epilepsy patients compared with healthy controls, and is negatively correlated with epilepsy duration. Using a similar approach, Chiang et al. (2015) report decreased structure-function coupling in patients with left temporal lobe epilepsy compared with healthy subjects. These two studies employ resting-state fMRI, which characterizes the static, interictal functional epileptic network. However, little is known

about the correlation between structural and functional connectivity during seizures. How does structure-function coupling change over the course of seizure evolution? And which particular connections drive these changes? Clinically, it is well understood that focal seizures often quickly spread to distant brain regions, but the relationship of this spread to underlying structure has not been quantified. Understanding where seizures are generated and how they spread has been hampered by sparsely sampled intracranial EEG and lesion-negative clinical brain images, and yet remains vital for planning surgical treatments for epilepsy.

In order to address these questions, we study structure-function coupling in 45 seizures from 9 drug-resistant localization-related epilepsy patients undergoing routine evaluation for epilepsy surgery. To construct time-varying functional connectivity (FC) networks, we utilize clinical recordings from intracranial EEG (iEEG), an invasive method that captures electrical activity from the brain in the form of aggregate local field potentials, at high spatial and temporal resolution [257,306]. To construct structural connectivity (SC) networks, we analyze High Angular Resolution Diffusion Imaging (HARDI), an advanced diffusion imaging method that can produce robust tractography results in regions of crossing white matter pathways [307]. Below we characterize relationships between these two modalities across time, frequency, and space. We hypothesize that there would be an increase in structure-function coupling during the progression from preictal to ictal states, as seizures spread along structural pathways. Our findings shed light on the pathophysiological processes involved in seizure dynamics,

which can ultimately inform new approaches for clinical intervention. We detail these investigations below.

7.3 Materials and Methods

7.3.1 Subjects

We studied nine patients undergoing pre-surgical evaluation for drug-resistant epilepsy at the Hospital of the University of Pennsylvania. Seizure localization was determined via comprehensive clinical evaluation, which included multimodal imaging, scalp and intracranial video-EEG monitoring, and neuropsychological testing. This study was approved by the Institutional Review Board of the University of Pennsylvania, and all subjects provided written informed consent prior to participating.

7.3.2 Intracranial EEG acquisition

Cortical surface and depth electrodes were implanted in patients based on clinical necessity. Electrode configurations (Ad Tech Medical Instruments, Racine, WI) consisted of linear cortical strips and two-dimensional cortical grid arrays (2.3 mm diameter with 10 mm inter-contact spacing), and linear depths (1.1 mm diameter with 10 mm inter-contact spacing). Continuous iEEG signals were obtained for the duration of each patient's stay in the epilepsy monitoring unit. Signals were recorded at 500 Hz. For each clinically identified seizure event, a board-certified epileptologist precisely annotated the onset time, termination time, seizure type, and electrodes recording artifact signals.

Seizure onset times were defined by the earliest electrographic change (EEC) [308]. Seizure types were classified using ILAE 2017 criteria [309] as focal aware (previously known as simple partial), focal impaired awareness (previously known as complex partial), or focal to bilateral tonic-clonic (previously known as complex partial with secondary generalization). Furthermore, the onset time of bilateral spread was noted for focal to bilateral tonic-clonic seizures. All annotations were verified and consistent with detailed clinical documentation. To ensure consistency and validity of the captured seizures, we discarded seizures that contained substantial artifacts in all electrodes, events that were very short (< 15 seconds), or those that occurred during sleep. De-identified iEEG recordings are available online on the International Epilepsy Electrophysiology Portal (www.ieeg.org, IEEG Portal) [261,262].

7.3.3 Image acquisition

Prior to electrode implantation, MRI data were collected on a 3T Siemens Magnetom Trio scanner (Siemens, Erlangen, Germany) using a 32-channel phased-array head coil. High-resolution anatomical images were acquired using a magnetization prepared rapid gradient-echo (MPRAGE) T1- weighted sequence (TR = 1810 ms, TE = 3.51 ms, flip angle = 9°, field of view = 240 mm, resolution = $0.94 \times 0.94 \times 1.0$ mm^3). High angular resolution diffusion imaging (HARDI) was acquired with a single-shot EPI multishell diffusion-weighted imaging sequence (116 diffusion sampling directions, *b*-values of 0, 300, 700 and 2000 s/mm^2, resolution = 2.5 x 2.5 x 2.5 mm^3 resolution, field

of view = 240 mm). Following electrode implantation, spiral CT images (Siemens, Erlangen, Germany) were obtained clinically for the purposes of electrode localization. Both bone and tissue windows were obtained (120 KV, 300 mA, axial slice thickness = 1.0 mm).

7.3.4 Region of interest selection

A brain network consists of nodes representing regions of interest (ROIs) within the brain, and edges representing the strength of connectivity between these ROIs. In order to carry out direct quantitative comparisons of structural and functional networks, it was necessary to establish a one-to-one correspondence between functional network nodes and structural network nodes. We therefore determined the location of each electrode in Montreal Neurological Institute (MNI) space and assigned each electrode to its nearest structural region of interest (ROI). Structural ROIs were defined by an upsampled version of the Automated Anatomical Labeling Atlas [310,311], which consisted of 600 roughly equally sized (ROI sizes averaging 2.14 +/- 0.28 cm^3) anatomically constrained regions covering the entire brain with the exception of the cerebellum. We chose this atlas (AAL-600) because it has ROIs of the same order of resolution as iEEG, obeys gross anatomical boundaries, and has successfully been used in prior studies to evaluate structural and functional connectivity patterns in the brain [116,117].

To determine electrode MNI coordinates, electrodes were first identified via

thresholding of the CT image and labeled using a semi-automated process. Each patient's CT and T1-weighted MRI images were aligned using 3D rigid affine registration, with mutual information as the similarity metric. The T1-weighted MRI images were then aligned to the standard MNI brain using diffeomorphic registration with the symmetric normalization (SyN) method [312]. The resulting transformations were used to warp the coordinates of the electrode centroids into MNI space. Co-registrations and transformations were carried out using Advanced Normalization Tools (ANTS) software [122,264], and the accuracy of each step was confirmed via visual inspection. In our final framework, electrodes served as nodes of the functional networks and the associated structural ROIs served as nodes of the structural networks.

7.3.5 Structural network generation

Diffusion-weighted images were skull-stripped via the FSL brain extraction tool and underwent eddy current and motion correction via the FSL eddy tool [313]. Next, DWI susceptibility distortions were mitigated using the structural T1-weighted image as follows: T1-weighted images were registered to the b0 image from the DWI scans using FSL FLIRT boundary-based registration [314], T1-weighted images were contrast inverted and intensity matched to the DWI image, and finally the DWI scans underwent nonlinear transformation to the T1-weighted scan [315]. Following these preprocessing steps, DSI-Studio (http://dsi-studio.labsolver.org) was used to reconstruct the orientation density functions (ODFs) within each voxel using generalized q-sample imaging with a

diffusion sampling length ratio of 1.25 [316]. Deterministic whole-brain fiber tracking was performed using an angular threshold of 35 degrees, step size of 1 mm, and quantitative anisotropy threshold based on Otsu's threshold [317]. The fiber trajectories were smoothed by averaging the propagation direction with 20% of the previous direction. Tracks with length shorter than 10 mm or longer than 400 mm were discarded, and a total of 1,000,000 tracts were generated per brain. Deterministic tractography was chosen based upon prior work indicating that deterministic tractography generates fewer false positive connections than probabilistic approaches, and that network-based estimations are substantially less accurate when false positives are introduced into the network compared with false negatives [50].

Subject-level AAL-600 atlases were generated in DWI space by applying the previously generated registration transformations from MNI to T1-weighted space and from T1-weighted space to DWI space. Finally, structural networks were generated by computing the number of streamlines connecting each pair of structural ROIs identified in Section *2.4*. The distribution of mean streamline lengths between each pair of structural ROIs for each patient is illustrated in **Supp. Figure 7.1**. Streamline counts were subsequently log-transformed to improve normality of the distribution, as is common in prior studies [134,318–320].

7.3.6 Functional network generation

Each seizure event consisted of an ictal period spanning the time between seizure onset (EEC) and termination, and an associated preictal period of equivalent duration immediately prior to seizure onset. Following removal of artifact-ridden electrodes, intracranial EEG signals for each seizure event were common-average referenced to reduce potential sources of correlated noise [265]. Next, each event was divided into 1 s non-overlapping time windows in accordance with previous studies [26,139,266,267].

To generate a functional network representing broadband functional interactions between iEEG signals for each 1 s time window, we carried out a method described in detail previously [26]. Namely, signals were notch-filtered at 60 Hz to remove power line noise, low-pass and high-pass filtered at 115 Hz and 5 Hz to account for noise and drift, and pre-whitened using a first-order autoregressive model to account for slow dynamics. Functional networks were then generated by applying a normalized cross-correlation function ρ between the signals of each pair of electrodes within each time window, using the formula:

$$\rho_{xy}(k) = \underset{\tau}{argmax}\left[\frac{1}{T}\sum_t \frac{(x_k(t)-\bar{x}_k)(y_k(t+\tau)-\bar{y}_k)}{\sigma_{x_k}\sigma_{y_k}}\right], \qquad \textit{(Eq. 7.1)}$$

where x and y are signals from two electrodes, k is the 1 s time window, t is one of the T samples during the time window, and τ is the time lag between signals, with a maximum lag of 250 ms. Next, to gain an understanding of the frequency dependence of SC-FC relationships, we generated functional networks across physiologically relevant frequency bands as described in detail in a previous study [139]. Specifically, multitaper

coherence estimation (time-bandwidth product of 5, 8 tapers) was used to compute functional coherence networks for each 1 s window across four frequency bands: α/θ (5-15 Hz), β (15-25 Hz), low-γ (30-40 Hz), and high-γ (95-105 Hz). Both broadband and frequency-specific networks were represented as full-weighted adjacency matrices for each 1 s window in each seizure event.

7.3.7 Structure-function coupling analysis

To quantify the relationship between structure and function in the epileptic brain, we computed the Pearson correlation coefficient between the edges of each SC network and the edges of each broadband FC network, followed by Fisher *r-z* transformation for variance stabilization [89]. This led to a time series of SC-FC correlations for each seizure event in each subject. To better understand the frequency-dependence of SC-FC coupling, we repeated the same analysis using the frequency-specific functional networks.

Next, to understand the extent to which the resulting SC-FC time series evolve similarly within each subject, we computed the Euclidean distances between these time series for all pairs of seizure events. Importantly, we first time-normalized the time series for each seizure event to span 200 evenly spaced time bins (100 preictal and 100 ictal). Next, for each seizure event, we generated a single vector consisting of the SC-FC time series for all six frequency bands: broadband, α/θ, β, low-γ, and high-γ. Euclidean

distances were then computed between all pairs of vectors, comprised of pairs belonging to the same patient and pairs belonging to different patients.

Finally, we wished to assess which edges in the structural network were responsible for the changes in SC-FC correlation between preictal and ictal periods. We therefore first computed a mean ictal and mean preictal broadband functional network for each subject by averaging across seizures events and across windows within each time period. Next, we carried out a virtual edge resection approach, in which we removed an edge from the network and computed the change in SC-FC correlation, $\Delta z(i)$, as follows:

$$\Delta z(i) = N[z - z^i], \qquad \textit{(Eq. 7.2)}$$

where z is the SC-FC correlation, z^i is the SC-FC correlation following removal of edge i, and N is the number of edges in the network. We performed this calculation for both preictal and ictal time periods. Since we were specifically interested in edges that statistically contribute to the increase in SC-FC correlation during seizures, we defined a measure of *contribution*, $\sigma(i)$, for each edge i in which a structural connection exists on the increase in SC-FC correlation during seizures as follows:

$$\sigma(i) = \left[\Delta z_{ictal}(i) - \Delta z_{preictal}(i)\right], \qquad \textit{(Eq. 7.3)}$$

where $\Delta z_{ictal}(i)$ and $\Delta z_{preictal}(i)$ are the relative changes in SC-FC correlations following removal of edge i during the ictal and preictal periods, respectively.

We defined *contributors* of SC-FC correlation during seizures as structural edges with $\Delta z_{ictal}(i) > 0$ and $\sigma(i) > 0$. This is because we wanted to identify regions that positively contributed to SC-FC correlation ictally, and more so ictally than preictally.

To better understand the properties of contributor edges, we computed the lengths of both the contributor edges and non-contributor edges, in terms of both streamline length and physical Euclidean distance. The purpose of this analysis was to determine whether the increased SC-FC correlation during seizures was due to long- or short-range connections.

A summary of our patient-level SC-FC analysis pipeline is illustrated in **Figure 1**.

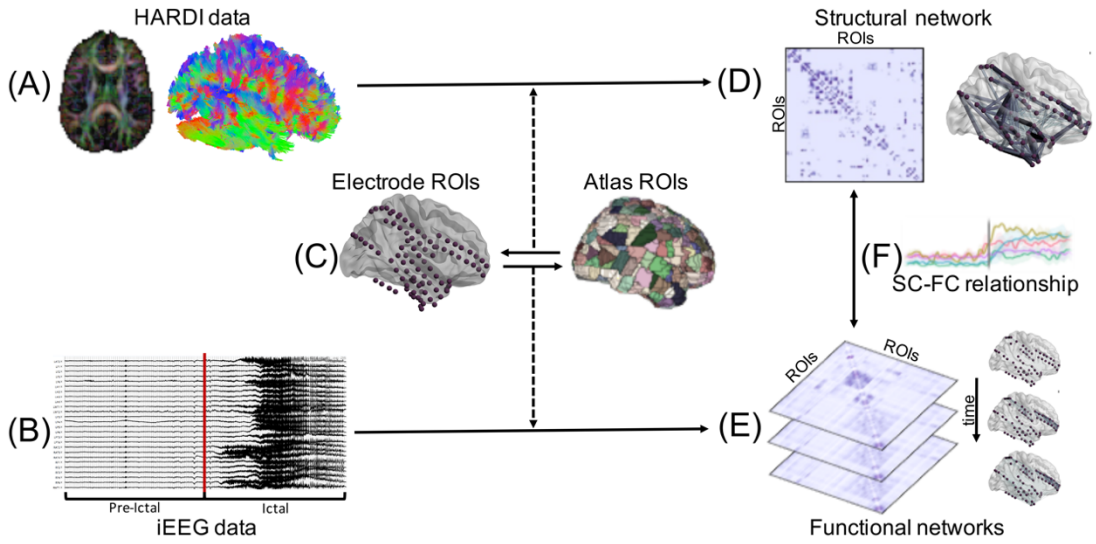

Figure 7.1: Summary of patient-level SC-FC analysis pipeline. **(A)** HARDI pre-processing and whole-brain tractography was carried out. **(B)** iEEG data were pre-processed and seizures were annotated, with each seizure event consisting of an ictal period and an associated preictal period of equivalent duration. **(C)** Regions of interest (ROIs) were selected via a one-to-one spatial correspondence between electrode centroids and atlas regions. **(D)** The structural connectivity (SC) network was generated using log-normalized streamline counts between atlas ROIs associated with each electrode location. **(E)** Time-varying broadband functional connectivity (FC) networks were generated for each 1s time window by computing correlation between iEEG signals across electrode pairs. Frequency-specific FC networks were similarly computed using coherence between iEEG signals across electrode pairs. **(F)** SC-FC relationships were quantified across time, frequency, and space (see **Methods** for details).

7.3.8 Statistical analyses

To determine whether the SC-FC correlations were significantly greater than chance, for each 1 second window we generated a null distribution of correlations via random permutation of the functional network edges (10,000 permutations). We then compared the mean SC-FC correlations during ictal and preictal periods with the null correlations. Next, to determine whether there was a significant increase in SC-FC correlation between preictal and ictal periods, we computed the difference between the mean ictal *z* and the mean preictal *z* for each seizure event. We modeled these paired differences using a linear mixed effects model with subject assignment as the random effect, and determined whether the difference was significantly greater than zero using the parametric bootstrap method (1000 bootstrapped samples), which is robust to small sample sizes [321,322]. To assess whether the findings were robust to our choice of non-ictal period, we repeated the above analysis substituting the preictal periods with interictal periods of equivalent duration that were at least 6 hours away from seizure activity (Note: data from these interictal periods were verified via visual inspection to be artifact-free and were processed as in *2.5*). To further compare findings during preictal and interictal periods, we also carried out the above statistical analysis to determine significant differences between mean preictal *z* and mean interictal *z*. To assess the degree of intra-subject similarity of SC-FC evolution, we compared the between-subject Euclidean distances (described in *2.6*) to the within-subject Euclidean distances and

tested the significance of the difference using permutational multivariate analysis of variance (PERMANOVA) (999 permutations) [323].

To characterize the properties of edges that contribute to the increase in SC-FC correlation during seizures, we computed the mean length of all contributor edges and the mean length of all non-contributor edges for each subject. Edge length was computed using two metrics: mean streamline length, and Euclidean distance. We compared the mean contributor and non-contributor edge lengths using a paired *t*-test. Furthermore, to assess the relationship between edge contribution and edge length among the contributor edges, we classified contributor edges into "low", "medium", and "high" contribution levels for each subject using tertiles. The edge lengths in these three categories were compared using paired *t*-tests. Finally, given prior knowledge that structural connection weights decrease with Euclidean distance [324–327], we repeated all analyses after removing the effect of Euclidean distance from the structural networks using linear regression.

7.4 Results

7.4.1 Clinical data

A total of 45 clinical seizures (mean duration 71 s +/- 44 s), were recorded across the 9 patients (mean age 40.2 +/- 11.8; 5 female). All seizures had focal onset, and were characterized as focal aware, focal impaired awareness, or focal to bilateral tonic-clonic. Patient demographic and clinical details are detailed in **Table 7.1**.

Subject #	Age	Gender	Outcome	Localization	Seizures recorded (#)	Treatment
1	48	F	IA	RTL	FBTC (3)	ATL + hippocampectomy
2	39	M	IB	RTL/DNET	FBTC (2)	ATL + hippocampectomy
3	45	F	IA	LTL	FIAS (1), FBTC (3)	ATL + hippocampectomy
4	36	M	IB	RTL	FAS (1), FIAS (5)	ATL + hippocampectomy
5	40	F	IA	RTL	FIAS (5)	ATL + hippocampectomy
6	50	M	N/A	Bilateral PVH	FIAS (4)	N/A
7	24	M	1B	RTL	FIAS (6)	ATL + hippocampectomy
8	58	F	N/A	BTL	FIAS (5)	N/A
9	22	F	1A	LTL	FIAS (10)	Laser ablation

Table 7.1: Patient demographic and clinical information. Post-surgical outcome was based on Engel classification score (scale: I–IV, seizure freedom to no improvement). M: male, F: female, RTL: right temporal lobe, LTL: left temporal lobe, BTL: bilateral temporal lobe, DNET: dysembryoplastic neuroepithelial tumor, PVH: Periventricular heterotopia, FIAS: focal impaired awareness seizure, FAS: focal aware seizure, FBTC: focal to bilateral tonic-clonic, ATL: anterior temporal lobectomy.

7.4.2 SC-FC coupling using broadband functional connectivity

To assess the overall temporal patterns of SC-FC coupling changes during seizures, we first quantified SC-FC correlations using broadband functional connectivity networks. For each individual seizure event, we determined the degree of SC-FC coupling, as measured by z (**Figure 7.2A**). For all seizures in all subjects, SC-FC coupling was significantly greater than chance during interictal, preictal and ictal periods ($p < 0.05$, permutation-based testing; **Figure 7.2B**). While the temporal progression of SC-FC changes was subject-specific (**Figure 7.2C**), there was a consistent increase between preictal and ictal periods (**Figure 7.2D**). Per-seizure paired differences in mean z values reveal significantly greater SC-FC correlation during ictal periods than preictal periods ($p = 0.023$, linear mixed effects analysis with subject as random effect). This

effect was maintained when substituting preictal periods with randomly chosen interictal clips of equivalent duration at least 6 hours away from seizure activity ($p = 0.021$). It was also maintained after regressing out the effect of distance ($p < 0.05$, **Supplementary Figure 7.2**). Moreover, there were no significant differences between preictal and interictal period SC-FC correlation values ($p = 0.70$).

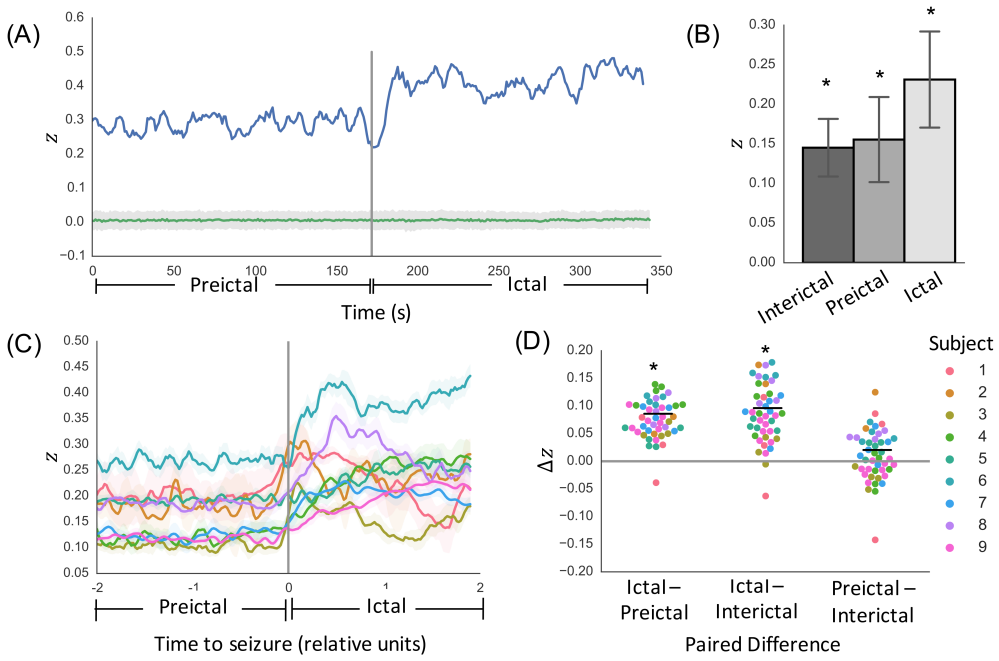

Figure 7.2: SC-FC analysis using broadband functional connectivity. **(A)** Temporal dynamics of SC-FC correlation as measured by Fisher's *z* for one example seizure in one patient, along with permutation-based null distribution of *z* values (mean +/- standard deviation). **(B)** Per-seizure *z* values during interictal, preictal, and ictal periods reveal SC-FC correlations significantly greater than chance across all periods ($p < 0.05$). **(C)** Temporal dynamics of SC-FC correlation across all subjects (mean +/- standard deviation across seizures in each subject). For visualization purposes only, time courses were normalized to span 200 evenly spaced time windows (100 preictal and 100 ictal) and smoothed with a 5-window moving average filter. **(D)** Per-seizure paired differences in mean *z* values reveal significantly greater SC-FC correlation during ictal periods than preictal periods ($p = 0.023$). This effect holds when substituting preictal periods with interictal periods ($p = 0.021$), with no significant difference between preictal and interictal period SC-FC correlation values ($p = 0.70$).

7.4.3 Frequency-specific SC-FC analysis

Next, to better understand the frequency dependence of the observed increase in SC-FC coupling during seizures, we repeated the SC-FC coupling analysis across four frequency bands (α/θ, β, low-γ, and high-γ). Similar to the previous analysis, we found that the extent of SC-FC coupling was significantly greater than chance at all time points during preictal and ictal periods ($p < 0.05$, permutation-based testing) for all frequency bands (**Figure 7.3A**). Moreover, while the preictal SC-FC was lower in higher frequency bands (**Figure 7.3B**), the increase in SC-FC coupling between preictal and ictal periods was significant across all frequency bands (α/θ: $p < 0.05$; β: $p < 0.05$; low-γ: $p < 0.05$; high-γ: $p < 0.05$) (**Figure 7.3B, 7.3C**). This finding was upheld after regressing out the effect of distance (**Supplementary Figure 7.2**). Similar to the findings with broadband functional connectivity, the findings were consistent when substituting preictal periods with interictal periods (α/θ: $p < 0.05$; β: $p < 0.05$; low-γ: $p < 0.05$; high-γ: $p < 0.05$), and there were no significant differences between preictal and interictal period SC-FC correlation values (α/θ: $p < 0.05$; β: $p < 0.05$; low-γ: $p < 0.05$; high-γ: $p < 0.05$) (**Supplementary Figure 7.3**).

We noted that while the increase was significant across all frequency bands, there were subject-specific frequency-dependent changes in SC-FC correlation. For example, subject 4 exhibited particularly salient increases in SC-$FC_{high\text{-}\gamma}$ coupling, while subject 6 had only moderate increases in SC-$FC_{high\text{-}\gamma}$ coupling but higher increases in SC-FC_{β} and SC-$FC_{low\text{-}\gamma}$ (**Figure 7.3C**, **Supplementary Figure 7.4**). To quantify this subject-specific

effect, we determined the most salient frequency band for each subject by identifying the band with the maximum mean increase in SC-FC coupling across seizure events (**Figure 7.3D**).

Finally, we characterized the within-subject similarity of the SC-FC time courses across all frequency bands. Using Euclidean distance as a measure of dissimilarity, we determined that the SC-FC time courses were significantly more similar within-patient than between-patient ($p<0.001$, $R^2=0.50$, permutational MANOVA) (**Figure 7.3E**), indicating that the temporal dynamics of SC-FC coupling is stereotyped in each patient across seizure events.

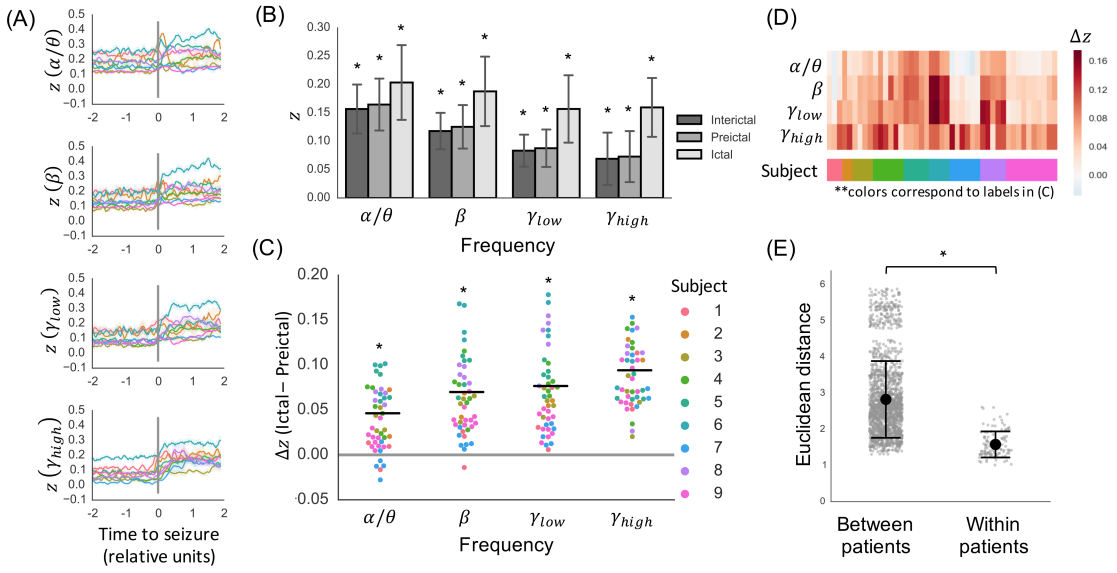

Figure 7.3: Frequency-specific SC-FC analysis. **(A)** Temporal dynamics of SC-FC correlation as measured by Fisher's *z* in alpha/theta, beta, low gamma, and high gamma frequency bands (mean +/- standard deviation across seizures in each subject, following interpolation to normalize ictal and preictal durations). **(B)** Per-seizure *z* values during interictal, preictal, and ictal periods (mean +/- S.D.) are significantly greater than chance ($p < 0.05$, permutation-based testing). **(C)** The increase in SC-FC correlation between preictal and ictal periods is further illustrated using paired differences for each individual seizure ($p < 0.05$, linear mixed effects analysis with subject as random effect). **(D)** Heatmap illustration highlights that frequency-dependent changes in SC-FC correlation are subject-specific. **(E)** Seizures within subjects evolve similarly, as evidenced by higher between-patient Euclidean distances between SC-FC correlation time courses compared to within-patient distances ($p<0.001$, $R^2=0.50$, permutational MANOVA).

7.4.4 SC-FC sub-analysis in focal to bilateral tonic-clonic seizures

As previously noted, the temporal progression of SC-FC changes was subject-specific (**Figure 7.2C, Figure 7.3A**). More specifically, we observed that in patients who experienced focal to bilateral tonic-clonic (FBTC) seizures (subjects 1-3), there was a drop in SC-FC coupling after the initial rise following seizure onset. Analysis of the individual SC-FC time courses in these seizures revealed that the drop corresponded with

onset of BTC activity (**Figure 7.4A**). Furthermore, quantitative analysis revealed significantly greater SC-FC correlation during pre-BTC ictal periods than preictal periods ($p < 0.05$), as well as significantly greater SC-FC correlation during pre-BTC ictal periods than post-BTC ictal periods ($p < 0.05$) (**Figure 7.4B**). To focus on the relationship between structure and function prior to the onset of generalized hypersynchronous activity, we limited the ictal periods to the periods prior BTC onset for the subsequent virtual edge resection analysis.

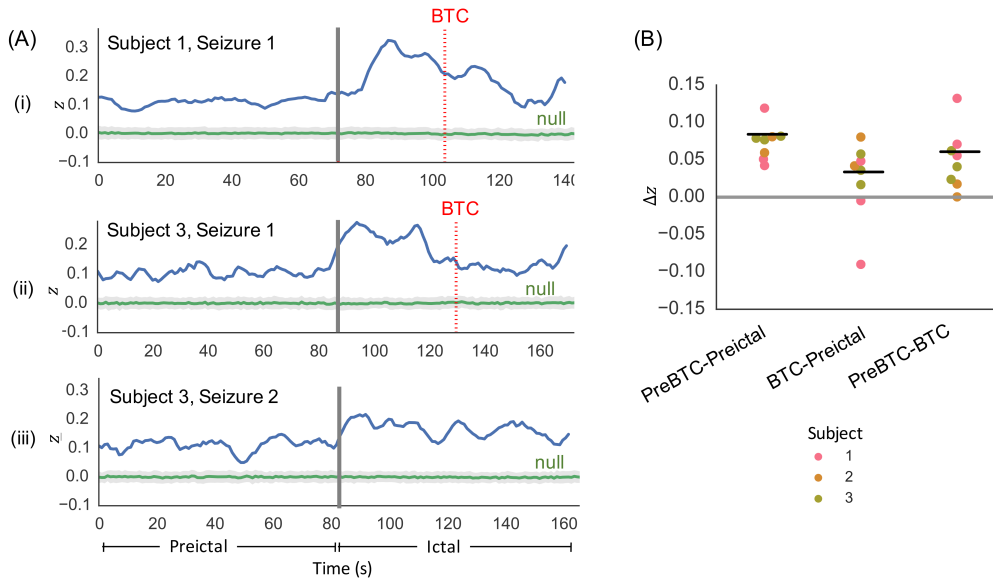

Figure 7.4: Assessment of SC-FC coupling in focal to bilateral tonic-clonic seizures. (**A**) Illustration of SC-FC coupling in two focal to bilateral tonic-clonic seizures, one from Subject 1 and one from Subject 3, reveals decrease in SC-FC coupling following bilateral tonic-clonic (BTC) onset (BTC onset indicated by dotted red line). For comparison, SC-FC coupling time course from a focal impaired awareness seizure in Subject 3 (without BTC) does not illustrate the same decrease. (**B**) In all bilateral tonic-clonic seizures, per-seizure paired differences in mean *z* values reveal significantly greater SC-FC correlation during pre-BTC ictal periods than preictal periods ($p < 0.05$), as well as significantly greater SC-FC correlation during pre-BTC ictal periods than post-BTC ictal periods ($p < 0.05$).

7.4.5 Virtual edge resection analysis

Given our finding that SC-FC coupling was significantly higher during ictal periods compared with preictal periods, we wanted to identify and characterize the structural edges that statistically accounted for this increase. After quantifying the contribution $\sigma(i)$ of each edge on the SC-FC coupling, we mapped the contributor edges onto each subject's brain (**Figure 7.5**) to facilitate subject-specific characterization of SC-FC relationships.

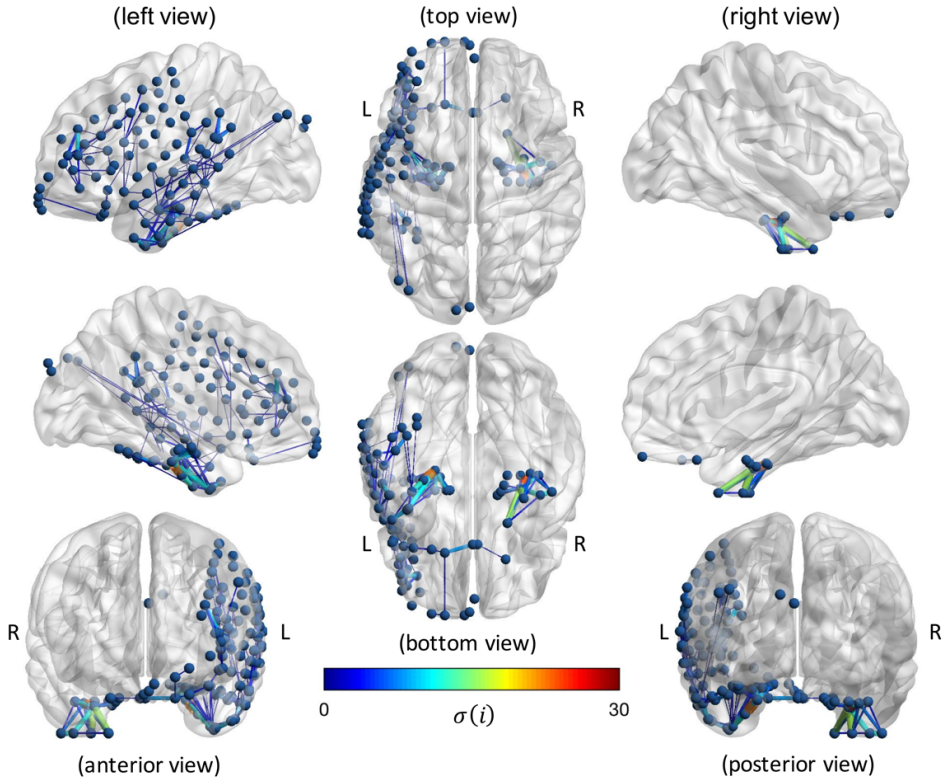

Figure 7.5: Subject-specific virtual edge resection approach to determine the contribution, $\sigma(i)$, of each structural edge i on the increase in SC-FC correlation during seizures. Results are shown for an example seizure in a patient with left temporal lobe epilepsy. Only "contributor" edges ($\sigma(i) > 0$ and $\Delta z_{ictal}(i) > 0$) are included to highlight edges that are associated with the SC-FC increase, with edge thickness and color used to representing magnitude of $\sigma(i)$.

Furthermore, at the group level, we determined that contributor edges were predominantly short-range, as quantified by significantly shorter edge lengths in contributors compared with non-contributors, based on both geometric Euclidean distance ($p < 0.05$, two-tailed paired t test) (**Figure 7.6A**) and streamline distance ($p < 0.05$, two-tailed paired t test) (**Figure 7.6B**). This finding held individually for each subject. Furthermore, within the contributor edges, we found a trend within each subject that higher contribution edges are shorter-range, both in terms of Euclidean distance (**Figure 7.6C**) and streamline length (**Figure 7.6D**). These findings held following distance regression (**Supplementary Figure 7.2**).

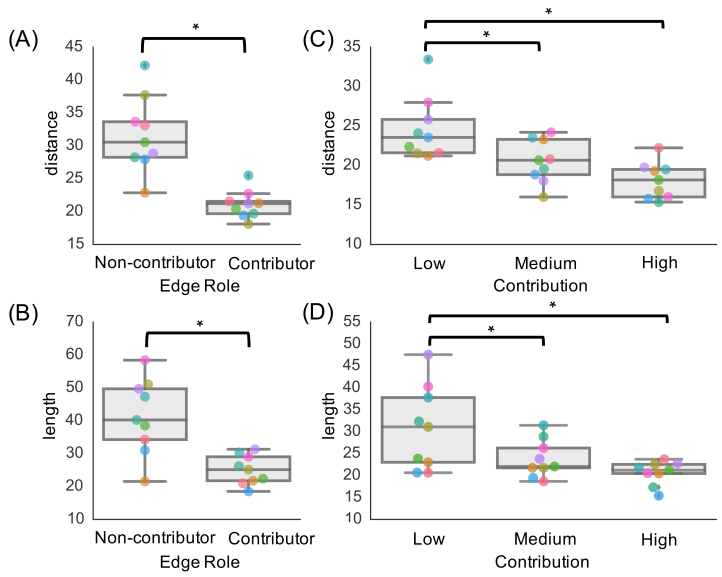

Figure 7.6: Relationship between edge contribution and edge length. Findings reveal that contributor edges are shorter-range in terms of both (**A**) Euclidean distance and (**B**) streamline length ($p < 0.05$, two-tailed paired t test). Furthermore, there is a trend that edges with higher contribution are shorter-range, in terms of both (**C**) Euclidean distance and (**D**) streamline length, with significant differences between low and medium contribution edges ($p < 0.05$, two-tailed paired t test), and low and high contribution edges ($p < 0.05$, two-tailed paired t test).

7.5 Discussion

The main goal of this study is to characterize the relationship between structural and functional connectivity during seizure onset and spread. Using network-based analysis of HARDI and iEEG data, we observe significant structure-function coupling at rest and a marked increase in this coupling during the progression from preictal to ictal states. This finding persists across frequency bands, with subject-specific levels of frequency-dependent increases. Furthermore, we present a technique for assessing the impact of individual structural connections to the observed ictal increase in structure-function correlation, and demonstrate that the effect is primarily due to short-range connections. Consistency of findings across seizures within each patient suggest that the spatiotemporal patterns of structure-function coupling are highly stereotyped. Our findings shed light on the dynamics of focal epileptic seizures in relation to underlying structure by demonstrating that seizure spread is tightly controlled by short-range structural connections.

7.5.1 Structure-function coupling across time, frequency and space

We observe greater coupling between structural and broadband functional networks during preictal and interictal periods than expected by chance. This finding is consistent with studies relating DTI-based structural networks with resting-state fMRI-based functional networks in healthy adults [73,117,132,296,297,299]. It is important to note that the functional signals recorded using iEEG are fundamentally different from

those recorded using fMRI. While recent studies suggest that blood-oxygen level dependent (BOLD) signal fluctuations correlate with slow fluctuations in EEG gamma power, the exact relationship between fMRI (BOLD) signals and electrophysiology has yet to be resolved [328–331] Nonetheless, our finding suggests that the tie between structure and function at rest is robust across diverse measurements of functional connectivity.

Interestingly, we observe that preictal FC networks in lower frequency bands have higher correlation to SC networks than preictal FC networks in higher frequency bands. This relationship decreases during the ictal period, with high SC-FC coupling in all frequency bands. Since it is believed that lower frequencies facilitate long-distance connections in the brain while higher frequencies facilitate shorter connections [275,332], our finding may suggest a relative shift to short-range, high-frequency connectivity during seizure generation. However, this observation could be influenced by the spatial distribution of electrodes, which tend to be clustered around the putative seizure onset zone, leading to a bias towards short-range connections within the seizure generating network. Therefore, we plan to corroborate these findings in patients with stereoelectroencephalography (stereo-EEG), an increasingly popular and less invasive method that records from stereotactically placed intracranial depth electrodes and allows for wider sampling of the brain network [333–335].

Despite individual variations inherent to our patient population, the finding of increased SC-FC coupling during ictal periods compared with preictal periods is

extremely robust, using both broadband and narrow-band functional connectivity. We compare SC-FC time courses from ictal periods to those of immediately preictal periods to allow for matched pairwise comparisons and to facilitate visualization along a continuous temporal scale. To ensure that activity immediately prior to seizure onset is a good representation of non-ictal activity, we repeat our analysis after substituting the preictal periods with interictal periods far away from seizure activity, and attain consistent results. The rise in SC-FC coupling during seizures indicates that seizures may rely on the brain's underlying architecture during initial seizure spread. We note that in several of the patients, the rise in SC-FC correlation occurs prior to the clinically-marked earliest electrographic change (EEC) representative of seizure onset, suggesting that SC-FC coupling may also be a valuable biomarker for seizure prediction or its early generation.

We discover that in focal to bilateral tonic-clonic seizures, there is a significant decrease in SC-FC coupling before onset of bilateral tonic-clonic activity. This finding is not surprising, given that bilateral tonic-clonic periods are associated with generalized hypersynchronous neural activity that is not localized to particular brain regions or pathways. This finding also supports that the observed SC-FC coupling increase during seizures relates to seizure propagation, and is not simply a result of highly synchronous activity.

Of note, the temporal dynamics of SC-FC coupling is highly consistent between seizures within each patient. This indicates that seizures may be "hard-wired" in a sense,

and is a macroscopic analog to the microscale finding of stereotyped ictal progression [336]. However, since our dataset consists of a relatively small group of adult focal epilepsy patients, with the majority having temporal lobe epilepsy, these conclusions may be specific to our dataset and should be confirmed using larger, more diverse patient populations.

To assess the role of each structural connection on the rise in SC-FC coupling during seizures, we implement a virtual edge resection method. Such leave-one-out simulation-based methods have been gaining popularity to probe the role of individual nodes and edges on overall network topology [139,337–339]. In our case, we determine the contribution of structural connections to SC-FC correlation and generate seizure-specific brain maps of these connections. Group-level analysis reveals that connections with high contribution are predominantly short-range, in terms of both streamline length and Euclidean distance. While the connections themselves are short, the locations of these connections appear distributed across the brain, including connections that are contralateral to seizure onset. This suggests that seizure dynamics rely on a distributed network of locally clustered connections. While further analyses and validation are needed, mapping connections in relation to seizure onset and spread could ultimately be useful in pinpointing networks for therapeutic removal via targeted methods such as laser ablation [1] or neurostimulation [2].

7.5.2 Methodological Considerations and Limitations

An important but inevitable limitation of this work relates to the incomplete sampling of the network via iEEG. Electrode placement is limited by clinical necessity and constrained by the boundaries of the craniotomy, in order to minimize invasiveness and reduce patient morbidity. Therefore, it is not possible to sample functional connectivity from the entire brain at high resolution time scales accessible through iEEG. While clinicians aim to place electrodes around putative seizure onset zones, it is possible that the entire seizure network may not be captured in certain cases. Recent efforts to map whole-brain iEEG using recordings from multiple subjects [281] and to construct models of whole-brain iEEG within individual subjects [282] may help circumvent this issue. Furthermore, while limited by impedance from the skull and inability to localize subcortical activity, ictal scalp EEG recordings, or ictal MEG recordings could supplement our intracranial analysis as both allow for consistent, grid-like spatial sampling with temporal resolution comparable to iEEG. The feasibility of such approaches has already been demonstrated in a recent paper revealing significant overlap between DTI networks and scalp EEG functional networks in the interictal state [303], and in early work on ictal MEG.

Our structural network findings are also limited by the capacity of our imaging methods. While HARDI has demonstrated superiority over conventional DTI in terms of its ability to resolve crossing fibers in regions of high fiber heterogeneity [307], HARDI tractography is still only a proxy for true white matter pathways. Similar to other

neuroimaging modalities, it is subject to partial volume effects and artifacts such as eddy current and susceptibility distortions [340,341]. Diffusion-based tractography is documented to recapitulate known pathways types including the short and long association fibers linking cortical gyri, the projection fiber connecting the cortex to lower portions of the brain, and the commissural fibers linking the two hemispheres [342], but may not reconstruct unmyelinated intracortical axons. Furthermore, streamline count may not be a direct measure of the strength of anatomical connectivity.

Due to the strong relationship between spatial proximity and structural connection strength, it is not possible to entirely disentangle the effects of Euclidean distance on our findings. Given prior work that epileptiform activity propagates within layer V of the neocortex [343], it is possible that local functional connections could partially be attributed to local cortical spreading phenomena rather than white matter propagation along short-range arcuate fibers. Local functional connectivity could also be due to measurement of a common source of signal. Despite these concerns, our finding of higher SC-FC coupling during seizures hold after regressing out Euclidean distance from our structural networks. This suggests that SC-FC coupling goes beyond solely distance-based effects.

Finally, while this study considers only direct structural connections, functional connectivity in the brain is also partially attributed to indirect structural connections [71,73,296]. Future studies could employ the property of communicability [344] to

incorporate path lengths of greater than one into the construction of structural networks while also accounting for the effects of spatial proximity.

7.5.3 Conclusions

We present a comprehensive approach to understanding the relationship between structure and function in the epileptic brain. Our work provides important insights into the structural underpinnings of seizure dynamics. It is our hope that by openly sharing our data and pipeline that we can accelerate translating this nascent field of network analysis in clinical epilepsy to help patients.

7.6 Acknowledgements

This work was supported by National Institutes of Health grants 1R01NS099348, K23-NS073801, 1R01NS085211, and 1R01MH112847. We also acknowledge support by the Thornton Foundation, the Mirowski Family Foundation, the ISI Foundation, the John D. and Catherine T. MacArthur Foundation, the Sloan Foundation, and the Paul Allen Foundation.

7.7 Supplementary Information

7.7.1 Supplementary Figures

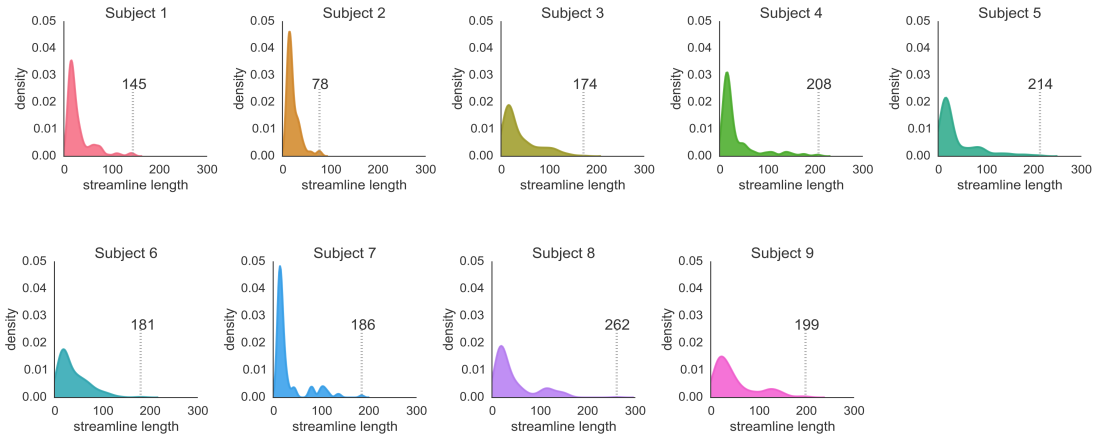

Supplementary Figure 7.1: Distributions of streamline lengths for each subject, along with max streamline length for each subject (dotted grey lines).

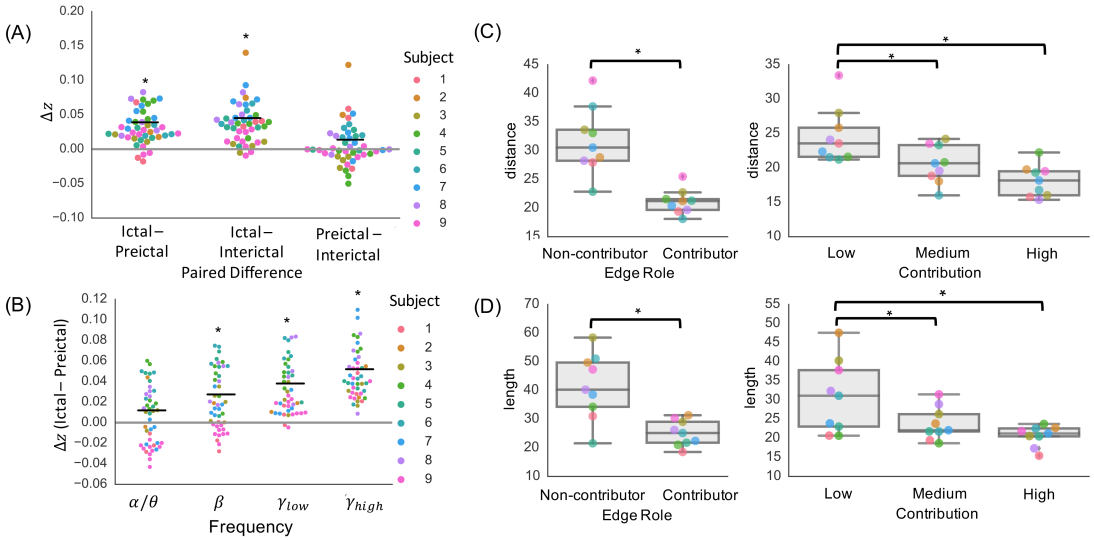

Supplementary Figure 7.2: Repetition of key SC-FC coupling analyses repeated following distance regression. (A) SC-FC analysis using broadband functional connectivity. (B) Frequency-specific SC-FC analysis. (C) Relationship between edge contribution and edge length.

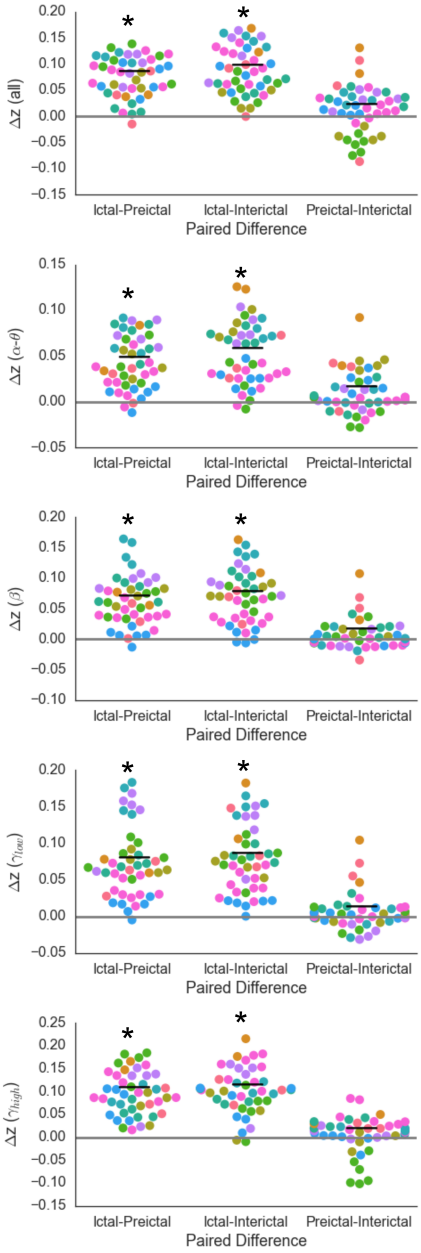

Supplementary Figure 7.3: Per-seizure paired differences in mean *z* values reveal significantly greater SC-FC correlation during ictal periods than preictal periods in all frequency bands ($p < 0.05$, linear mixed effects analysis with subject as random effect). This effect holds when substituting preictal periods with randomly chosen interictal clips of equivalent duration at least 6 hours away from seizure activity ($p < 0.05$), with no significant difference between preictal and interictal period SC-FC correlation values ($p > 0.05$). See **Figures 7.2B** and 7.**3C** for details.

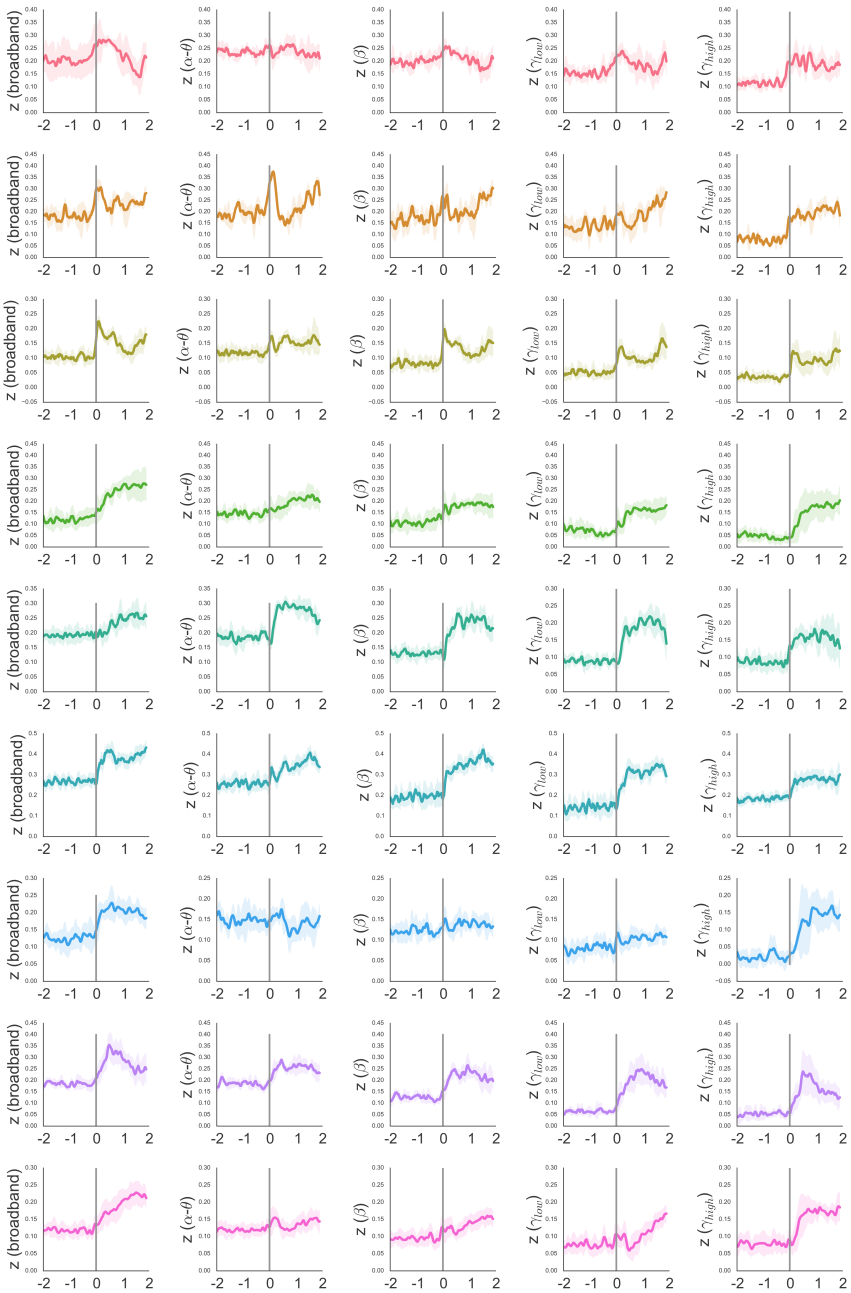

Supplementary Figure 7.4: Temporal dynamics of SC-FC correlation as measured by Fisher's *z* in alpha/theta, beta, low gamma, and high gamma frequency bands (mean +/- standard deviation across seizures in each subject, following interpolation to normalize ictal and preictal durations), delineated by subject (row/color) and band (column). See **Figure 7.3A** for details.

Chapter 8: Conclusions

Using the framework of network neuroscience, this thesis incorporates data from high resolution structural and functional neuroimaging, electrophysiology, and expert clinicians to map epileptic networks in drug-resistant epilepsy patients. The key innovations of this work are detailed below:

1) Multimodal approach: Most brain network studies focus solely on either function or structure, but there is a growing understanding that the two are intertwined [27–29]. The approaches outlined in this thesis help elucidate the interplay between function and structure, and investigate how this relationship may be altered in epilepsy patients. I employ data derived from different modalities, including high resolution structural and resting-state functional MRI, high angular resolution diffusion imaging (HARDI), and iEEG. A combined structural-functional approach to epilepsy can provide complementary information to aid in localizing seizure onset, predicting pathways of seizure spread, and informing clinical decision making.

2) Novel methods: To facilitate analyses, I developed new analytical methods and applied existing methods in unique ways. For example, I defined intra-MTL network asymmetry-based metrics in Chapters 3 and 4 as biomarkers for unilateral temporal lobe

epilepsy. In Chapter 5 and 6, I explored quantitative tools to map subject-specific iEEG networks. In Chapter 7, I developed a simple framework for merging structural and function data, and for characterizing structure-function coupling across different temporal states (interictal, pre-ictal, and ictal). I constructed robust permutation-based methods and null models to evaluate the statistical significance of our findings in these unique multivariate datasets.

3) Focus on clinical application: While a number of studies have analyzed group-level differences of neuroimaging and EEG-based measures between epilepsy patients and healthy subjects, or between different groups of epilepsy patients (e.g. partial vs. complex), there is a lack of application of these findings to clinical practice. This is because group-level findings can be relatively unhelpful for characterization of individual patients. This thesis aims to bring graph theoretical analyses of neurological data to clinical application by carrying out subject-level analyses whenever possible.

4) Data sharing: The methods and analyses described in this thesis require validation on larger clinical datasets. Therefore, to facilitate replicability of our findings across multiple institutions, scanners, and protocols, I provide open-source code, data, and pipelines on Github. My repositories are publicly available here: https://github.com/shahpreya.

Future work entails bringing these multimodal seizure network mapping methods to clinical utility. The next step will be to use classification-based analysis to facilitate subject-specific predictions of diagnosis and prognosis. For example, I have written a simple classification algorithm to distinguish TLE patients and healthy controls based on the structural and functional asymmetry features presented in Chapters 3 and 4, which I hope to apply in future, larger-scale 7T MRI datasets. Spatiotemporal spectrographic biomarkers (such as those described in Chapter 5), node-level and edge-level network synchrony metrics (such as those described in Chapter 6) and measures of structure-function relationships (such as those described in Chapter 7) could all be incorporated as features in machine learning models for seizure localization or outcome prediction. Epilepsy data can be messy, complex, and incredibly heterogeneous across the patient population. While one metric or modality alone will likely not be the "magic bullet" for seizure localization, multimodal biomarkers of structural and functional connectivity show great promise in identifying abnormal epileptic networks that can be targeted for removal.

.

References

1. Willie JT, Laxpati NG, Drane DL, Gowda A, Appin C, Hao C, et al. Real-time magnetic resonance-guided stereotactic laser amygdalohippocampotomy for mesial temporal lobe epilepsy. Neurosurgery. 2014;74: 569–584. doi:10.1227/NEU.0000000000000343

2. Fisher RS, Velasco AL. Electrical brain stimulation for epilepsy. Nat Rev Neurol. Nature Publishing Group; 2014;10: 261–270. doi:10.1038/nrneurol.2014.59

3. Engel J. Mesial temporal lobe epilepsy: what have we learned? Neuroscientist. 2001;7: 340–52. Available: http://www.ncbi.nlm.nih.gov/pubmed/11488399

4. Kwan P, Schachter SC, Brodie MJ. Drug-Resistant Epilepsy. N Engl J Med. 2011;10365: 919–26.

5. Engel J. Surgery for Seizures. N Engl J Med. 1996;334: 647–653. doi:10.1056/NEJM199603073341008

6. Fazel S, Wolf A, Långström N, Newton CR, Lichtenstein P. Premature mortality in epilepsy and the role of psychiatric comorbidity: a total population study. Lancet (London, England). 2013;382: 1646–54. doi:10.1016/S0140-6736(13)60899-5

7. French JA. Refractory Epilepsy: Clinical Overview. Epilepsia. Blackwell Publishing Inc; 2007;48: 3–7. doi:10.1111/j.1528-1167.2007.00992.x

8. Spencer SS, Berg AT, Vickrey BG, Sperling MR, Bazil CW, Shinnar S, et al. Predicting long-term seizure outcome after resective epilepsy surgery: The Multicenter Study. Neurology. 2005;65: 912–918. doi:10.1212/01.wnl.0000176055.45774.71

9. Wiebe S. Epilepsy: Outcome patterns in epilepsy surgery—the long-term view. Nat Rev Neurol. Nature Publishing Group; 2012;8: 123–124. doi:10.1038/nrneurol.2012.9

10. Siegel AM, Jobst BC, Thadani VM, Rhodes CH, Lewis PJ, Roberts DW, et al. Medically Intractable, Localization-related Epilepsy with Normal MRI: Presurgical Evaluation and Surgical Outcome in 43 Patients. Epilepsia. Blackwell Science Inc; 2001;42: 883–888. doi:10.1046/j.1528-1157.2001.042007883.x

11. Téllez-Zenteno JF, Ronquillo LH, Moien-Afshari F, Wiebe S. Surgical outcomes in lesional and non-lesional epilepsy: A systematic review and meta-analysis. Epilepsy Res. 2010;89: 310–318. doi:10.1016/j.eplepsyres.2010.02.007

12. Burneo JG, Steven DA, McLachlan RS, Parrent AG. Morbidity associated with the use of intracranial electrodes for epilepsy surgery. Can J Neurol Sci. 2006;33: 223–7. Available: http://www.ncbi.nlm.nih.gov/pubmed/16736735

13. Greiner HM, Horn PS, Tenney JR, Arya R, Jain S V., Holland KD, et al. Preresection intraoperative electrocorticography (ECoG) abnormalities predict seizure-onset zone and outcome in pediatric epilepsy surgery. Epilepsia. Wiley/Blackwell (10.1111); 2016;57: 582–589. doi:10.1111/epi.13341

14. Bernhardt BC, Hong S, Bernasconi A, Bernasconi N. Imaging structural and functional brain networks in temporal lobe epilepsy. Front Hum Neurosci. Frontiers; 2013;7: 624. doi:10.3389/fnhum.2013.00624

15. Chu CJ, Kramer MA, Pathmanathan J, Bianchi MT, Westover MB, Wizon L, et al. Emergence of Stable Functional Networks in Long-Term Human Electroencephalography. J Neurosci. 2012;32: 2703–2713. doi:10.1523/JNEUROSCI.5669-11.2012

16. Bassett DS, Sporns O. Network neuroscience [Internet]. Nature Neuroscience. Nature Research; 2017. pp. 353–364. doi:10.1038/nn.4502

17. Bullmore E, Sporns O. Complex brain networks: Graph theoretical analysis of structural and functional systems [Internet]. Nature Reviews Neuroscience. Nature Publishing Group; 2009. pp. 186–198. doi:10.1038/nrn2575

18. Mechelli A, Friston KJ, Frackowiak RS, Price CJ. Structural Covariance in the Human Cortex. J Neurosci. 2005;25: 8303–8310. doi:10.1523/JNEUROSCI.0357-05.2005

19. Hagmann P, Cammoun L, Gigandet X, Meuli R, Honey CJ, Wedeen VJ, et al. Mapping the Structural Core of Human Cerebral Cortex. Friston KJ, editor. PLoS Biol. Public Library of Science; 2008;6: e159. doi:10.1371/journal.pbio.0060159

20. Pedersen M, Omidvarnia AH, Walz JM, Jackson GD. Increased segregation of brain networks in focal epilepsy: An fMRI graph theory finding. NeuroImage Clin. Elsevier; 2015;8: 536–542. doi:10.1016/j.nicl.2015.05.009

21. van Mierlo P, Papadopoulou M, Carrette E, Boon P, Vandenberghe S, Vonck K, et al. Functional brain connectivity from EEG in epilepsy: Seizure prediction and epileptogenic focus localization. Prog Neurobiol. Elsevier Ltd; 2014;121: 19–35. doi:10.1016/j.pneurobio.2014.06.004

22. Kramer MA, Eden UT, Lepage KQ, Kolaczyk ED, Bianchi MT, Cash SS. Emergence of Persistent Networks in Long-Term Intracranial EEG Recordings. J

Neurosci. 2011;31: 15757–15767. doi:10.1523/JNEUROSCI.2287-11.2011

23. Tomlinson SB, Porter BE, Marsh ED. Interictal network synchrony and local heterogeneity predict epilepsy surgery outcome among pediatric patients. Epilepsia. 2017;58: 402–411. doi:10.1111/epi.13657

24. Khambhati AN, Litt B, Bassett DS. Dynamic network drivers of seizure generation, propagation and termination in human epilepsy. 2014; doi:10.1073/pnas.0709640104

25. Korzeniewska A, Cervenka MC, Jouny CC, Perilla JR, Harezlak J, Bergey GK, et al. Ictal propagation of high frequency activity is recapitulated in interictal recordings: Effective connectivity of epileptogenic networks recorded with intracranial EEG. Neuroimage. 2014;101: 96–113. doi:10.1016/j.neuroimage.2014.06.078

26. Khambhati AN, Bassett DS, Oommen BS, Chen SH, Lucas TH, Davis KA, et al. Recurring functional interactions predict network architecture of interictal and ictal states in neocortical epilepsy. eneuro. 2017; ENEURO.0091-16.2017. doi:10.1523/ENEURO.0091-16.2017

27. Squire LR, Zola-Morgan S. The medial temporal lobe memory system. Science (80-). 1991;253: 1380–1386. doi:10.1126/science.1896849

28. Buckner RL, Sepulcre J, Talukdar T, Krienen FM, Liu H, Hedden T, et al. Cortical Hubs Revealed by Intrinsic Functional Connectivity: Mapping, Assessment of Stability, and Relation to Alzheimer's Disease. J Neurosci. 2009;29: 1860–1873. doi:10.1523/JNEUROSCI.5062-08.2009

29. Mueller SG, Schuff N, Yaffe K, Madison C, Miller B, Weiner MW. Hippocampal atrophy patterns in mild cognitive impairment and Alzheimer's disease. Hum Brain Mapp. 2010;31: 1339–1347. doi:10.1002/hbm.20934

30. Mueller SG, Laxer KD, Barakos J, Cheong I, Garcia P, Weiner MW. Subfield atrophy pattern in temporal lobe epilepsy with and without mesial sclerosis detected by high-resolution MRI at 4 Tesla: Preliminary results. Epilepsia. 2009;50: 1474–1483. doi:10.1111/j.1528-1167.2009.02010.x

31. Small SA, Schobel SA, Buxton RB, Witter MP, Barnes CA. A pathophysiological framework of hippocampal dysfunction in ageing and disease. Nat Rev Neurosci. Nature Publishing Group; 2011;12: 585–601. doi:10.1038/nrn3085

32. Schobel SA, Lewandowski NM, Corcoran CM, Moore H, Brown T, Malaspina D, et al. Differential Targeting of the CA1 Subfield of the Hippocampal Formation by

Schizophrenia and Related Psychotic Disorders. Arch Gen Psychiatry. American Medical Association; 2009;66: 938. doi:10.1001/archgenpsychiatry.2009.115

33. Posener JA, Wang L, Price JL, Gado MH, Province MA, Miller MI, et al. High-Dimensional Mapping of the Hippocampus in Depression. Am J Psychiatry. 2003;160: 83–89. doi:10.1176/appi.ajp.160.1.83

34. Suthana NA, Donix M, Wozny DR, Bazih A, Jones M, Heidemann RM, et al. High-resolution 7T fMRI of Human Hippocampal Subfields during Associative Learning. J Cogn Neurosci. 2015;27: 1194–206. doi:10.1162/jocn_a_00772

35. Guzowski JF, Knierim JJ, Moser EI. Ensemble Dynamics of Hippocampal Regions CA3 and CA1. Neuron. 2004;44: 581–584. doi:10.1016/j.neuron.2004.11.003

36. Suthana NA, Ekstrom AD, Moshirvaziri S, Knowlton B, Bookheimer SY. Human Hippocampal CA1 Involvement during Allocentric Encoding of Spatial Information. J Neurosci. 2009;29: 10512–10519. doi:10.1523/JNEUROSCI.0621-09.2009

37. Leal SL, Yassa MA. Neurocognitive Aging and the Hippocampus across Species. Trends Neurosci. 2015;38: 800–812. doi:10.1016/j.tins.2015.10.003

38. Leutgeb JK, Leutgeb S, Moser M-B, Moser EI. Pattern Separation in the Dentate Gyrus and CA3 of the Hippocampus. Science (80-). 2007;315: 961–966. doi:10.1126/science.1135801

39. Bartsch T, Dohring J, Rohr A, Jansen O, Deuschl G. CA1 neurons in the human hippocampus are critical for autobiographical memory, mental time travel, and autonoetic consciousness. Proc Natl Acad Sci. 2011;108: 17562–17567. doi:10.1073/pnas.1110266108

40. Bartsch T, Schönfeld R, Müller FJ, Alfke K, Leplow B, Aldenhoff J, et al. Focal lesions of human hippocampal CA1 neurons in transient global amnesia impair place memory. Science. 2010;328: 1412–1415. doi:10.1126/science.1188160

41. Lavenex P, Amaral DG. Hippocampal-neocortical interaction: A hierarchy of associativity. Hippocampus. John Wiley & Sons, Inc.; 2000;10: 420–430. doi:10.1002/1098-1063(2000)10:4<420::AID-HIPO8>3.0.CO;2-5

42. Moreno H, Wu WE, Lee T, Brickman A, Mayeux R, Brown TR, et al. Imaging the Aβ-Related Neurotoxicity of Alzheimer Disease. Arch Neurol. American Medical Association; 2007;64: 1467. doi:10.1001/archneur.64.10.1467

43. de Leon MJ, Convit A, Wolf OT, Tarshish CY, DeSanti S, Rusinek H, et al. Prediction of cognitive decline in normal elderly subjects with 2-[(18)F]fluoro-2-deoxy-D-glucose/poitron-emission tomography (FDG/PET). Proc Natl Acad Sci U S A. National Academy of Sciences; 2001;98: 10966–71. doi:10.1073/pnas.191044198

44. de Flores R, La Joie R, Chételat G. Structural imaging of hippocampal subfields in healthy aging and Alzheimer's disease. Neuroscience. 2015;309: 29–50. doi:10.1016/j.neuroscience.2015.08.033

45. Wolk DA, Das SR, Mueller SG, Weiner MW, Yushkevich PA, Alzheimer's Disease Neuroimaging Initiative. Medial temporal lobe subregional morphometry using high resolution MRI in Alzheimer's disease. Neurobiol Aging. 2017;49: 204–213. doi:10.1016/j.neurobiolaging.2016.09.011

46. Das SR, Mechanic-Hamilton D, Pluta J, Korczykowski M, Detre JA, Yushkevich PA. Heterogeneity of functional activation during memory encoding across hippocampal subfields in temporal lobe epilepsy. Neuroimage. 2011;58: 1121–1130. doi:10.1016/j.neuroimage.2011.06.085

47. Wang Z, Neylan TC, Mueller SG, Lenoci M, Truran D, Marmar CR, et al. Magnetic Resonance Imaging of Hippocampal Subfields in Posttraumatic Stress Disorder. Arch Gen Psychiatry. 2010;67: 296. doi:10.1001/archgenpsychiatry.2009.205

48. Sheline YI, Wang PW, Gado MH, Csernansky JG, Vannier MW. Hippocampal atrophy in recurrent major depression. Proc Natl Acad Sci U S A. 1996;93: 3908–13. doi:10.1073/pnas.93.9.3908

49. Malykhin NV, Coupland NJ. Hippocampal neuroplasticity in major depressive disorder. Neuroscience. 2015;309: 200–213. doi:10.1016/j.neuroscience.2015.04.047

50. Zalesky A, Fornito A, Harding IH, Cocchi L, Yücel M, Pantelis C, et al. Whole-brain anatomical networks: Does the choice of nodes matter? Neuroimage. 2010;50: 970–983. doi:10.1016/j.neuroimage.2009.12.027

51. Kitzbichler MG, Henson RNA, Smith ML, Nathan PJ, Bullmore ET. Cognitive effort drives workspace configuration of human brain functional networks. J Neurosci. 2011;31: 8259–70. doi:10.1523/JNEUROSCI.0440-11.2011

52. Braun U, Schäfer A, Walter H, Erk S, Romanczuk-Seiferth N, Haddad L, et al. Dynamic reconfiguration of frontal brain networks during executive cognition in humans. Proc Natl Acad Sci. 2015;112: 11678–11683.

doi:10.1073/pnas.1422487112

53. Bassett DS, Bullmore ET, Meyer-Lindenberg A, Apud JA, Weinberger DR, Coppola R. Cognitive fitness of cost-efficient brain functional networks. Proc Natl Acad Sci. 2009;106: 11747–11752. doi:10.1073/pnas.0903641106

54. Stanley ML, Dagenbach D, Lyday RG, Burdette JH, Laurienti PJ. Changes in global and regional modularity associated with increasing working memory load. Front Hum Neurosci. 2014;8: 954. doi:10.3389/fnhum.2014.00954

55. Bassett DS, Nelson BG, Mueller BA, Camchong J, Lim KO. Altered resting state complexity in schizophrenia. Neuroimage. 2012;59: 2196–2207. doi:10.1016/j.neuroimage.2011.10.002

56. Bernhardt BC, Chen Z, He Y, Evans AC, Bernasconi N. Graph-Theoretical Analysis Reveals Disrupted Small-World Organization of Cortical Thickness Correlation Networks in Temporal Lobe Epilepsy. Cereb Cortex. 2011;21: 2147–2157. doi:10.1093/cercor/bhq291

57. Supekar K, Menon V, Rubin D, Musen M, Greicius MD. Network Analysis of Intrinsic Functional Brain Connectivity in Alzheimer's Disease. Sporns O, editor. PLoS Comput Biol. Public Library of Science; 2008;4: e1000100. doi:10.1371/journal.pcbi.1000100

58. Zhang Z, Liao W, Chen H, Mantini D, Ding J-R, Xu Q, et al. Altered functional-structural coupling of large-scale brain networks in idiopathic generalized epilepsy. Brain. Oxford University Press; 2011;134: 2912–28. doi:10.1093/brain/awr223

59. Minkova L, Eickhoff SB, Abdulkadir A, Kaller CP, Peter J, Scheller E, et al. Large-scale brain network abnormalities in Huntington's disease revealed by structural covariance. Hum Brain Mapp. 2016;37: 67–80. doi:10.1002/hbm.23014

60. Soto FA, Bassett DS, Ashby FG. Dissociable changes in functional network topology underlie early category learning and development of automaticity. Neuroimage. 2016;141: 220–241. doi:10.1016/j.neuroimage.2016.07.032

61. Ould Ismail AAO, Amouzandeh G, Grant SC. Structural connectivity within neural ganglia: A default small-world network. Neuroscience. 2016;337: 276–284. doi:10.1016/j.neuroscience.2016.09.024

62. Khalsa S, Mayhew SD, Chechlacz M, Bagary M, Bagshaw AP. The structural and functional connectivity of the posterior cingulate cortex: Comparison between deterministic and probabilistic tractography for the investigation of structure–

function relationships. Neuroimage. 2014;102: 118–127. doi:10.1016/j.neuroimage.2013.12.022

63. Palop JJ, Chin J, Roberson ED, Wang J, Thwin MT, Bien-Ly N, et al. Aberrant Excitatory Neuronal Activity and Compensatory Remodeling of Inhibitory Hippocampal Circuits in Mouse Models of Alzheimer's Disease. Neuron. 2007;55: 697–711. doi:10.1016/j.neuron.2007.07.025

64. Deco G, Ponce-Alvarez A, Hagmann P, Romani GL, Mantini D, Corbetta M. How Local Excitation-Inhibition Ratio Impacts the Whole Brain Dynamics. J Neurosci. 2014;34: 7886–7898. doi:10.1523/JNEUROSCI.5068-13.2014

65. Biswal B, Yetkin FZ, Haughton VM, Hyde JS. Functional connectivity in the motor cortex of resting human brain using echo-planar MRI. Magn Reson Med. 1995;34: 537–41. Available: http://www.ncbi.nlm.nih.gov/pubmed/8524021

66. Bassett DS, Bullmore E, Verchinski BA, Mattay VS, Weinberger DR, Meyer-Lindenberg A. Hierarchical Organization of Human Cortical Networks in Health and Schizophrenia. J Neurosci. 2008;28: 9239–9248. doi:10.1523/JNEUROSCI.1929-08.2008

67. Zielinski BA, Gennatas ED, Zhou J, Seeley WW. Network-level structural covariance in the developing brain. Proc Natl Acad Sci. National Acad Sciences; 2010;107: 18191–18196. doi:10.1073/pnas.1003109107

68. Alexander-Bloch A, Giedd JN, Bullmore E. Imaging structural co-variance between human brain regions. Nat Rev Neurosci. 2013;14: 322–336. doi:10.1038/nrn3465

69. Lerch JP, Worsley K, Shaw WP, Greenstein DK, Lenroot RK, Giedd J, et al. Mapping anatomical correlations across cerebral cortex (MACACC) using cortical thickness from MRI. Neuroimage. 2006;31: 993–1003. doi:10.1016/j.neuroimage.2006.01.042

70. Gong G, He Y, Chen ZJ, Evans AC. Convergence and divergence of thickness correlations with diffusion connections across the human cerebral cortex. Neuroimage. 2012;59: 1239–48. doi:10.1016/j.neuroimage.2011.08.017

71. Liang H, Wang H, Reus M de, Heuvel M van den, Berman M, McIntosh A, et al. Structure-Function Network Mapping and Its Assessment via Persistent Homology. Bassett DS, editor. PLOS Comput Biol. SIAM Monographs on Mathematical Modeling and Computation; 2017;13: e1005325. doi:10.1371/journal.pcbi.1005325

72. Honey CJ, Honey CJ, Sporns O, Sporns O, Cammoun L, Cammoun L, et al. Predicting human resting-state functional connectivity from structural connectivity. Proc Natl Acad Sci U S A. 2009;106: 2035–40. doi:10.1073/pnas.0811168106

73. Damoiseaux JS, Greicius MD. Greater than the sum of its parts: a review of studies combining structural connectivity and resting-state functional connectivity. Brain Struct Funct. 2009;213: 525–33. doi:10.1007/s00429-009-0208-6

74. Koch MA, Norris DG, Hund-Georgiadis M. An Investigation of Functional and Anatomical Connectivity Using Magnetic Resonance Imaging. Neuroimage. 2002;16: 241–250. doi:10.1006/nimg.2001.1052

75. Yushkevich PA, Pluta JB, Wang H, Xie L, Ding S-L, Gertje EC, et al. Automated volumetry and regional thickness analysis of hippocampal subfields and medial temporal cortical structures in mild cognitive impairment. Hum Brain Mapp. 2015;36: 258–287. doi:10.1002/hbm.22627

76. Wang H, Suh JW, Das SR, Pluta JB, Craige C, Yushkevich PA. Multi-Atlas Segmentation with Joint Label Fusion. IEEE Trans Pattern Anal Mach Intell. NIH Public Access; 2013;35: 611–23. doi:10.1109/TPAMI.2012.143

77. Wang H, Das SR, Suh JW, Altinay M, Pluta J, Craige C, et al. A learning-based wrapper method to correct systematic errors in automatic image segmentation: consistently improved performance in hippocampus, cortex and brain segmentation. Neuroimage. NIH Public Access; 2011;55: 968–85. doi:10.1016/j.neuroimage.2011.01.006

78. Yushkevich PA, Piven J, Hazlett HC, Smith RG, Ho S, Gee JC, et al. User-guided 3D active contour segmentation of anatomical structures: significantly improved efficiency and reliability. Neuroimage. 2006;31: 1116–28. doi:10.1016/j.neuroimage.2006.01.015

79. Pipitone J, Park MTM, Winterburn J, Lett TA, Lerch JP, Pruessner JC, et al. Multi-atlas segmentation of the whole hippocampus and subfields using multiple automatically generated templates. Neuroimage. 2014;101: 494–512. doi:10.1016/j.neuroimage.2014.04.054

80. Wisse LEM, Kuijf HJ, Honingh AM, Wang H, Pluta JB, Das SR, et al. Automated Hippocampal Subfield Segmentation at 7T MRI. Am J Neuroradiol. 2016;37: 1050–1057. doi:10.3174/ajnr.A4659

81. Friston KJ, Frith CD, Frackowiak RS, Turner R. Characterizing dynamic brain responses with fMRI: a multivariate approach. Neuroimage. 1995;2: 166–72.

Available: http://www.ncbi.nlm.nih.gov/pubmed/9343599

82. Kang X, Yund EW, Herron TJ, Woods DL. Improving the resolution of functional brain imaging: analyzing functional data in anatomical space. Magn Reson Imaging. 2007;25: 1070–8. doi:10.1016/j.mri.2006.12.005

83. Van Dijk KRA, Hedden T, Venkataraman A, Evans KC, Lazar SW, Buckner RL. Intrinsic Functional Connectivity As a Tool For Human Connectomics: Theory, Properties, and Optimization. J Neurophysiol. 2010;103.

84. Avants BB, Tustison NJ, Wu J, Cook PA, Gee JC. An open source multivariate framework for n-tissue segmentation with evaluation on public data. Neuroinformatics. NIH Public Access; 2011;9: 381–400. doi:10.1007/s12021-011-9109-y

85. Van Dijk KRA, Sabuncu MR, Buckner RL. The influence of head motion on intrinsic functional connectivity MRI. Neuroimage. 2012;59: 431–8. doi:10.1016/j.neuroimage.2011.07.044

86. Power JD, Barnes KA, Snyder AZ, Schlaggar BL, Petersen SE. Spurious but systematic correlations in functional connectivity MRI networks arise from subject motion. Neuroimage. NIH Public Access; 2012;59: 2142–54. doi:10.1016/j.neuroimage.2011.10.018

87. Carr VA, Rissman J, Wagner AD. Imaging the Human Medial Temporal Lobe with High-Resolution fMRI. Neuron. 2010;65: 298–308. doi:10.1016/j.neuron.2009.12.022

88. Zalesky A, Fornito A, Bullmore E. On the use of correlation as a measure of network connectivity. Neuroimage. 2012;60: 2096–2106. doi:10.1016/j.neuroimage.2012.02.001

89. Fisher RA. On the “probable error” of a coefficient of correlation deduced from a small sample. Metron. 1921;1: 3–32. doi:10.2307/1928524

90. Voevodskaya O, Simmons A, Nordenskjöld R, Kullberg J, Ahlström H, Lind L, et al. The effects of intracranial volume adjustment approaches on multiple regional MRI volumes in healthy aging and Alzheimer’s disease. Front Aging Neurosci. Frontiers Media SA; 2014;6: 264. doi:10.3389/fnagi.2014.00264

91. Wu K, Taki Y, Sato K, Kinomura S, Goto R, Okada K, et al. Age-related changes in topological organization of structural brain networks in healthy individuals. Hum Brain Mapp. Wiley Subscription Services, Inc., A Wiley Company; 2012;33: 552–568. doi:10.1002/hbm.21232

92. Hosseini SMH, Hoeft F, Kesler SR. GAT: A Graph-Theoretical Analysis Toolbox for Analyzing Between-Group Differences in Large-Scale Structural and Functional Brain Networks. Lambiotte R, editor. PLoS One. Public Library of Science; 2012;7: e40709. doi:10.1371/journal.pone.0040709

93. Bassett DS, Bullmore ET. Small-World Brain Networks Revisited. Neurosci. 2016; 107385841666772. doi:10.1177/1073858416667720

94. Li C, Wang H, De Haan W, Stam CJ, Mieghem P Van. The correlation of metrics in complex networks with applications in functional brain networks. J Stat Mech. 2011; doi:10.1088/1742-5468/2011/11/P11018

95. Lynall M-E, Bassett DS, Kerwin R, McKenna PJ, Kitzbichler M, Muller U, et al. Functional Connectivity and Brain Networks in Schizophrenia. J Neurosci. 2010;30: 9477–9487. doi:10.1523/JNEUROSCI.0333-10.2010

96. Rubinov M, Sporns O. Complex network measures of brain connectivity: Uses and interpretations. Neuroimage. Elsevier Inc.; 2010;52: 1059–1069. doi:10.1016/j.neuroimage.2009.10.003

97. Fox MD, Zhang D, Snyder AZ, Raichle ME. The Global Signal and Observed Anticorrelated Resting State Brain Networks. J Neurophysiol. 2009;101: 3270–3283. doi:10.1152/jn.90777.2008

98. Chai XJ, Castañón AN, Öngür D, Whitfield-Gabrieli S. Anticorrelations in resting state networks without global signal regression. Neuroimage. 2012;59: 1420–1428. doi:10.1016/j.neuroimage.2011.08.048

99. Murphy K, Fox MD. Towards a consensus regarding global signal regression for resting state functional connectivity MRI. Neuroimage. 2016; doi:10.1016/j.neuroimage.2016.11.052

100. Onnela JP, Saramäki J, Kertész J, Kaski K. Intensity and coherence of motifs in weighted complex networks. Phys Rev E - Stat Nonlinear, Soft Matter Phys. 2005;71. doi:10.1103/PhysRevE.71.065103

101. Latora V, Marchiori M. Efficient Behavior of Small-World Networks. 2001;87. doi:10.1103/PhysRevLett.87.198701

102. Latora V, Marchiori M. Economic small-world behavior in weighted networks. Eur Phys J B. 2003;32: 249–263. doi:10.1140/epjb/e2003-00095-5

103. Rubinov M, Bassett DS. Emerging evidence of connectomic abnormalities in schizophrenia. J Neurosci. Society for Neuroscience; 2011;31: 6263–5.

doi:10.1523/JNEUROSCI.0382-11.2011

104. Achard S, Bullmore E. Efficiency and cost of economical brain functional networks. PLoS Comput Biol. 2007;3: 0174–0183. doi:10.1371/journal.pcbi.0030017

105. Zuo X-N, Ehmke R, Mennes M, Imperati D, Castellanos FX, Sporns O, et al. Network Centrality in the Human Functional Connectome. Cereb Cortex. Oxford University Press; 2012;22: 1862–1875. doi:10.1093/cercor/bhr269

106. van den Heuvel MP, Sporns O. Network hubs in the human brain. Trends Cogn Sci. Elsevier; 2013;17: 683–696. doi:10.1016/j.tics.2013.09.012

107. Alexander-Bloch AF, Gogtay N, Meunier D, Birn R, Clasen L, Lalonde F, et al. Disrupted Modularity and Local Connectivity of Brain Functional Networks in Childhood-Onset Schizophrenia. Front Syst Neurosci. Frontiers; 2010;4: 147. doi:10.3389/fnsys.2010.00147

108. Doucet GE, Ashwini S, Pustina D, Skidmore C, Sperling MR, Tracy JI. Early and Late Age of Seizure Onset have a Differential Impact on Brain Resting-State Organization in Temporal Lobe Epilepsy. 2014;

109. Fair DA, Cohen AL, Power JD, Dosenbach NUF, Church JA, Miezin FM, et al. Functional brain networks develop from a “local to distributed” organization. PLoS Comput Biol. Public Library of Science; 2009;5: e1000381. doi:10.1371/journal.pcbi.1000381

110. Porter MA, Onnela J-P, Mucha PJ. Communities in Networks. Am Math Soc. 2009;56: 0–26. doi:10.1016/j.physrep.2009.11.002

111. Fortunato S. Community detection in graphs [Internet]. Physics Reports. 2010. pp. 75–174. doi:10.1016/j.physrep.2009.11.002

112. Bassett DS, Porter MA, Wymbs NF, Grafton ST, Carlson JM, Mucha PJ. Robust detection of dynamic community structure in networks. Chaos An Interdiscip J Nonlinear Sci. AIP Publishing; 2013;23: 13142. doi:10.1063/1.4790830

113. Newman MEJ. Fast algorithm for detecting community structure in networks. Phys Rev E - Stat Nonlinear, Soft Matter Phys. 2004;69. doi:10.1103/PhysRevE.69.066133

114. Blondel VD, Guillaume J-L, Lambiotte R, Lefebvre E. Fast unfolding of communities in large networks. J Stat Mech Theory Exp. 2008;10008: 6. doi:10.1088/1742-5468/2008/10/P10008

115. Liao W, Zhang Z, Mantini D, Xu Q, Wang Z, Chen G, et al. Relationship Between Large-Scale Functional and Structural Covariance Networks in Idiopathic Generalized Epilepsy. Brain Connect. 2013;3: 241–253. doi:10.1089/brain.2012.0132

116. Hermundstad AM, Brown KS, Bassett DS, Aminoff EM, Frithsen A, Johnson A, et al. Structurally-Constrained Relationships between Cognitive States in the Human Brain. Hilgetag CC, editor. PLoS Comput Biol. Public Library of Science; 2014;10: e1003591. doi:10.1371/journal.pcbi.1003591

117. Hermundstad AM, Bassett DS, Brown KS, Aminoff EM, Clewett D, Freeman S, et al. Structural foundations of resting-state and task-based functional connectivity in the human brain. Proc Natl Acad Sci. 2013;110: 6169–6174. doi:10.1073/pnas.1219562110

118. Doron KW, Bassett DS, Gazzaniga MS. Dynamic network structure of interhemispheric coordination. Proc Natl Acad Sci U S A. National Academy of Sciences; 2012;109: 18661–8. doi:10.1073/pnas.1216402109

119. Traud AL, Kelsic ED, Mucha PJ, Porter MA. Comparing Community Structure to Characteristics in Online Collegiate Social Networks *. 2011;53: 526–543. doi:10.1137/080734315

120. Friston KJ, Holmes AP, Worsley KJ, Poline JP, Frith CD, Frackowiak RSJ. Statistical parametric maps in functional imaging: A general linear approach. Hum Brain Mapp. 1994;2: 189–210. doi:10.1002/hbm.460020402

121. Smith SM, Jenkinson M, Woolrich MW, Beckmann CF, Behrens TEJ, Johansen-Berg H, et al. Advances in functional and structural MR image analysis and implementation as FSL. Neuroimage. 2004;23: S208–S219. doi:10.1016/j.neuroimage.2004.07.051

122. Avants B, Tustison N, Song G. Advanced Normalization Tools (ANTS). Insight J. 2009; 1–35. Available: ftp://ftp3.ie.freebsd.org/pub/sourceforge/a/project/ad/advants/Documentation/ants.pdf

123. Pedraza O, BOWERS D, GILMORE R. Asymmetry of the hippocampus and amygdala in MRI volumetric measurements of normal adults. J Int Neuropsychol Soc. 2004;10. doi:10.1017/S1355617704105080

124. Woolard AA, Heckers S. Anatomical and functional correlates of human hippocampal volume asymmetry. Psychiatry Res Neuroimaging. 2012;201: 48–53. doi:10.1016/j.pscychresns.2011.07.016

125. Hou G, Yang X, Yuan TF. Hippocampal asymmetry: Differences in structures and functions. Neurochemical Research. 2013. pp. 453–460. doi:10.1007/s11064-012-0954-3

126. Kelley WM, Miezin FM, McDermott KB, Buckner RL, Raichle ME, Cohen NJ, et al. Hemispheric specialization in human dorsal frontal cortex and medial temporal lobe for verbal and nonverbal memory encoding. Neuron. 1998;20: 927–936. doi:10.1016/S0896-6273(00)80474-2

127. Kennepohl S, Sziklas V, Garver KE, Wagner DD, Jones-Gotman M. Memory and the medial temporal lobe: Hemispheric specialization reconsidered. Neuroimage. 2007;36: 969–978. doi:10.1016/j.neuroimage.2007.03.049

128. Zeineh MM, Palomero-Gallagher N, Axer M, Gräβel D, Goubran M, Wree A, et al. Direct Visualization and Mapping of the Spatial Course of Fiber Tracts at Microscopic Resolution in the Human Hippocampus. Cereb Cortex. 2016;22: bhw010. doi:10.1093/cercor/bhw010

129. Stafstrom CE. The role of the subiculum in epilepsy and epileptogenesis. Epilepsy Curr. Blackwell Publishing, Inc; 2005;5: 121–9. doi:10.1111/j.1535-7511.2005.00049.x

130. Sporns O. Network attributes for segregation and integration in the human brain. Curr Opin Neurobiol. 2013;23: 162–171. doi:10.1016/j.conb.2012.11.015

131. Lacy JW, Stark CEL. Intrinsic functional connectivity of the human medial temporal lobe suggests a distinction between adjacent MTL cortices and hippocampus. Hippocampus. 2012;22: 2290–2302. doi:10.1002/hipo.22047

132. van den Heuvel MP, Mandl RCW, Kahn RS, Hulshoff Pol HE. Functionally linked resting-state networks reflect the underlying structural connectivity architecture of the human brain. Hum Brain Mapp. 2009;30: 3127–3141. doi:10.1002/hbm.20737

133. Goni J, van den Heuvel MP, Avena-Koenigsberger A, Velez de Mendizabal N, Betzel RF, Griffa A, et al. Resting-brain functional connectivity predicted by analytic measures of network communication. Proc Natl Acad Sci. 2014;111: 833–838. doi:10.1073/pnas.1315529111

134. Wirsich J, Perry A, Ridley B, Proix T, Golos M, Bénar C, et al. Whole-brain analytic measures of network communication reveal increased structure-function correlation in right temporal lobe epilepsy. NeuroImage Clin. 2016;11: 707–718. doi:10.1016/j.nicl.2016.05.010

135. Hagmann P, Kurant M, Gigandet X, Thiran P, Wedeen VJ, Meuli R, et al.

Mapping human whole-brain structural networks with diffusion MRI. PLoS One. 2007;2. doi:10.1371/journal.pone.0000597

136. Fornito A, Zalesky A, Breakspear M. Graph analysis of the human connectome: Promise, progress, and pitfalls. Neuroimage. 2013;80: 426–444. doi:10.1016/j.neuroimage.2013.04.087

137. Fornito A, Zalesky A, Breakspear M. The connectomics of brain disorders. Nat Rev Neurosci. Nature Research; 2015;16: 159–172. doi:10.1038/nrn3901

138. Li Y, Liu Y, Li J, Qin W, Li K, Yu C, et al. Brain Anatomical Network and Intelligence. Sporns O, editor. PLoS Comput Biol. Hunan Med College; 2009;5: e1000395. doi:10.1371/journal.pcbi.1000395

139. Khambhati AN, Davis KA, Lucas TH, Litt B, Bassett DS. Virtual Cortical Resection Reveals Push-Pull Network Control Preceding Seizure Evolution. Neuron. 2016;91: 1170–1182. doi:10.1016/j.neuron.2016.07.039

140. Pezawas L, Meyer-Lindenberg A, Drabant EM, Verchinski BA, Munoz KE, Kolachana BS, et al. 5-HTTLPR polymorphism impacts human cingulate-amygdala interactions: a genetic susceptibility mechanism for depression. Nat Neurosci. 2005;8: 828–834. doi:10.1038/nn1463

141. Modo M, Hitchens TK, Liu JR, Richardson RM, Modo M. Detection of Aberrant Hippocampal Mossy Fiber Connections: Ex Vivo Mesoscale Diffusion MRI and Microtractography With Histological Validation in a Patient With Uncontrolled Temporal Lobe Epilepsy. 2015; doi:10.1002/hbm.23066

142. Yassa MA, Muftuler LT, Stark CEL. Ultrahigh-resolution microstructural diffusion tensor imaging reveals perforant path degradation in aged humans in vivo. Proc Natl Acad Sci U S A. National Academy of Sciences; 2010;107: 12687–91. doi:10.1073/pnas.1002113107

143. Suthana NA, Donix M, Wozny DR, Bazih A, Jones M, Heidemann RM, et al. High-resolution 7T fMRI of Human Hippocampal Subfields during Associative Learning. J Cogn Neurosci. 2015;27: 1194–1206. doi:10.1162/jocn_a_00772

144. Das SR, Pluta J, Mancuso L, Kliot D, Orozco S, Dickerson BC, et al. Increased functional connectivity within medial temporal lobe in mild cognitive impairment. Hippocampus. 2013;23: 1–6. doi:10.1002/hipo.22051

145. Libby LA, Ekstrom AD, Ragland JD, Ranganath C. Differential Connectivity of Perirhinal and Parahippocampal Cortices within Human Hippocampal Subregions Revealed by High-Resolution Functional Imaging. J Neurosci. 2012;32. Available:

http://www.jneurosci.org/content/32/19/6550

146. Maass A, Berron D, Libby LA, Ranganath C, Düzel E, Barkhof F, et al. Functional subregions of the human entorhinal cortex. Elife. eLife Sciences Publications Limited; 2015;4: 111–120. doi:10.7554/eLife.06426

147. Das SR, Pluta J, Mancuso L, Kliot D, Yushkevich PA, Wolk DA. Anterior and posterior MTL networks in aging and MCI. Neurobiol Aging. 2015;36: S141–S150. doi:10.1016/j.neurobiolaging.2014.03.041

148. Insausti R, Juottonen K, Soininen H, Insausti a M, Partanen K, Vainio P, et al. MR volumetric analysis of the human entorhinal, perirhinal, and tempropolar cortices. Am J Med. 1998;19: 659–671.

149. Iglesias JE, Augustinack JC, Nguyen K, Player CM, Player A, Wright M, et al. A computational atlas of the hippocampal formation using ex vivo, ultra-high resolution MRI: Application to adaptive segmentation of in vivo MRI. Neuroimage. 2015;115: 117–137. doi:10.1016/j.neuroimage.2015.04.042

150. Simic G, Kostovic I, Winblad B, Bogdanovic N. Volume and Number Of Neurons Of the Human Hippocampal Formation In Normal Aging and Alzheimers Disease. J Comp Neurol. 1997;379: 482–494.

151. Harding A, Halliday GM, Kril JJ. Variation in hippocampal neuron number with age and brain volume. Cereb Cortex. Oxford University Press; 1998;8: 710–718. doi:10.1093/cercor/8.8.710

152. Pruessner JC, Köhler S, Crane J, Pruessner M, Lord C, Byrne A, et al. Volumetry of temporopolar, perirhinal, entorhinal and parahippocampal cortex from high-resolution MR images: considering the variability of the collateral sulcus. Cereb cortex. 2002;12: 1342–1353. doi:10.1093/cercor/12.12.1342

153. Engel J. Mesial Temporal Lobe Epilepsy: What Have We Learned? Neurosci. SAGE Publications; 2001;7: 340–352. doi:10.1177/107385840100700410

154. Wieser H-G. ILAE Commission Report. Mesial temporal lobe epilepsy with hippocampal sclerosis. Epilepsia. 2004;45: 695–714. doi:10.1111/j.0013-9580.2004.09004.x

155. Engel J. Surgery for Seizures. N Engl J Med. Massachusetts Medical Society ; 1996;334: 647–653. doi:10.1056/NEJM199603073341008

156. Chiang S, Haneef Z. Graph theory findings in the pathophysiology of temporal lobe epilepsy. Clin Neurophysiol. 2014;125: 1295–305.

doi:10.1016/j.clinph.2014.04.004

157. Haneef Z, Chiang S. Clinical correlates of graph theory findings in temporal lobe epilepsy. Seizure. 2014;23: 809–18. doi:10.1016/j.seizure.2014.07.004

158. Liao W, Zhang Z, Pan Z, Mantini D, Ding J, Duan X, et al. Altered functional connectivity and small-world in mesial temporal lobe epilepsy. PLoS One. Public Library of Science; 2010;5: e8525. doi:10.1371/journal.pone.0008525

159. Pereira FR, Alessio A, Sercheli MS, Pedro T, Bilevicius E, Rondina JM, et al. Asymmetrical hippocampal connectivity in mesial temporal lobe epilepsy: evidence from resting state fMRI. BMC Neurosci. BioMed Central; 2010;11: 66. doi:10.1186/1471-2202-11-66

160. James GA, Tripathi SP, Ojemann JG, Gross RE, Drane DL. Diminished default mode network recruitment of the hippocampus and parahippocampus in temporal lobe epilepsy. J Neurosurg. 2013;119: 288–300. doi:10.3171/2013.3.JNS121041

161. Morgan VL, Sonmezturk HH, Gore JC, Abou-Khalil B. Lateralization of temporal lobe epilepsy using resting functional magnetic resonance imaging connectivity of hippocampal networks. Epilepsia. Blackwell Publishing Ltd; 2012;53: 1628–1635. doi:10.1111/j.1528-1167.2012.03590.x

162. Pittau F, Grova C, Moeller F, Dubeau F, Gotman J. Patterns of altered functional connectivity in mesial temporal lobe epilepsy. Epilepsia. Blackwell Publishing Ltd; 2012;53: 1013–1023. doi:10.1111/j.1528-1167.2012.03464.x

163. Barron DS, Fox PT, Pardoe H, Lancaster J, Price LR, Blackmon K, et al. Thalamic functional connectivity predicts seizure laterality in individual TLE patients: Application of a biomarker development strategy. NeuroImage Clin. 2015;7: 273–280. doi:10.1016/j.nicl.2014.08.002

164. Haneef Z, Lenartowicz A, Yeh HJ, Engel J, Stern JM. Network Analysis of the Default Mode Network Using Functional Connectivity MRI in Temporal Lobe Epilepsy. J Vis Exp. 2014; e51442. doi:10.3791/51442

165. He X, Doucet GE, Sperling M, Sharan A, Tracy JI. Reduced thalamocortical functional connectivity in temporal lobe epilepsy. Epilepsia. 2015;56: 1571–1579. doi:10.1111/epi.13085

166. Bettus G, Guedj E, Joyeux F, Confort-Gouny S, Soulier E, Laguitton V, et al. Decreased basal fMRI functional connectivity in epileptogenic networks and contralateral compensatory mechanisms. Hum Brain Mapp. Wiley Subscription Services, Inc., A Wiley Company; 2009;30: 1580–1591. doi:10.1002/hbm.20625

167. Liu M, Concha L, Lebel C, Beaulieu C, Gross DW. Mesial temporal sclerosis is linked with more widespread white matter changes in temporal lobe epilepsy. NeuroImage Clin. 2012;1: 99–105. doi:10.1016/j.nicl.2012.09.010

168. Muhlhofer W, Tan Y-L, Mueller SG, Knowlton R. MRI-negative temporal lobe epilepsy-What do we know? Epilepsia. 2017;58: 727–742. doi:10.1111/epi.13699

169. Vaughan DN, Rayner G, Tailby C, Jackson GD. MRI-negative temporal lobe epilepsy. Neurology. 2016;87: 1934–1942. doi:10.1212/WNL.0000000000003289

170. Bernhardt BC, Bernasconi A, Liu M, Hong S-J, Caldairou B, Goubran M, et al. The spectrum of structural and functional imaging abnormalities in temporal lobe epilepsy. Ann Neurol. 2016;80: 142–153. doi:10.1002/ana.24691

171. Reyes A, Thesen T, Wang X, Hahn D, Yoo D, Kuzniecky R, et al. Resting-state functional MRI distinguishes temporal lobe epilepsy subtypes. Epilepsia. 2016;57: 1475–1484. doi:10.1111/epi.13456

172. Sharma AK, Reams RY, Jordan WH, Miller MA, Thacker HL, Snyder PW. Mesial Temporal Lobe Epilepsy: Pathogenesis, Induced Rodent Models and Lesions. Toxicol Pathol. 2007;35: 984–999. doi:10.1080/01926230701748305

173. Bonilha L, Martz GU, Glazier SS, Edwards JC. Subtypes of medial temporal lobe epilepsy: Influence on temporal lobectomy outcomes? [Internet]. Epilepsia. Blackwell Publishing Ltd; 2012. pp. 1–6. doi:10.1111/j.1528-1167.2011.03298.x

174. Wennberg R, Arruda F, Quesney LF, Olivier A. Preeminence of extrahippocampal structures in the generation of mesial temporal seizures: evidence from human depth electrode recordings. Epilepsia. 2002;43: 716–26. Available: http://www.ncbi.nlm.nih.gov/pubmed/12102674

175. van der Kolk AG, Hendrikse J, Zwanenburg JJM, Visser F, Luijten PR. Clinical applications of 7T MRI in the brain. Eur J Radiol. 2013;82: 708–718. doi:10.1016/j.ejrad.2011.07.007

176. Balchandani P, Naidich TP. Ultra-high-field MR neuroimaging [Internet]. American Journal of Neuroradiology. 2015. pp. 1204–1215. doi:10.3174/ajnr.A4180

177. Shah P, Bassett DS, Wisse LEM, Detre JA, Stein JM, Yushkevich PA, et al. Mapping the structural and functional network architecture of the medial temporal lobe using 7T MRI. Hum Brain Mapp. 2017; doi:10.1002/hbm.23887

178. Ver Hoef LW, Williams FB, Kennedy RE, Szaflarski JP, Knowlton RC. Predictive

value of hippocampal internal architecture asymmetry in temporal lobe epilepsy. Epilepsy Res. 2013;106: 155–163. doi:10.1016/j.eplepsyres.2013.05.008

179. Jokeit H, Okujava M, Woermann FG. Memory fMRI lateralizes temporal lobe epilepsy. Neurology. 2001;57: 1786–1793. doi:10.1212/WNL.57.10.1786

180. Davis KA, Nanga RPR, Das S, Chen SH, Hadar PN, Pollard JR, et al. Glutamate imaging (GluCEST) lateralizes epileptic foci in nonlesional temporal lobe epilepsy. Sci Transl Med. American Association for the Advancement of Science; 2015;7: 309ra161. doi:10.1126/scitranslmed.aaa7095

181. Cook MJ, Fish DR, Shorvon SD, Straughan K, Stevens JM. Hippocampal volumetric and morphometric studies in frontal and temporal lobe epilepsy. Brain. 1992;115 Pt 4: 1001–15. Available: https://watermark.silverchair.com/115-4-1001.pdf goo.gl/4cMeFa

182. Goffin K, Van Paesschen W, Dupont P, Baete K, Palmini A, Nuyts J, et al. Anatomy-based reconstruction of FDG-PET images with implicit partial volume correction improves detection of hypometabolic regions in patients with epilepsy due to focal cortical dysplasia diagnosed on MRI. Eur J Nucl Med Mol Imaging. 2010;37: 1148–1155. doi:10.1007/s00259-010-1405-5

183. Ver Hoef LW, Paige AL, Riley KO, Cure J, Soltani M, Williams FB, et al. Evaluating hippocampal internal architecture on MRI: inter-rater reliability of a proposed scoring system. Epilepsy Res. NIH Public Access; 2013;106: 146–54. doi:10.1016/j.eplepsyres.2013.05.009

184. Farid N, Girard HM, Kemmotsu N, Smith ME, Magda SW, Lim WY, et al. Temporal Lobe Epilepsy: Quantitative MR Volumetry in Detection of Hippocampal Atrophy. Radiology. Radiological Society of North America, Inc.; 2012;264: 542–550. doi:10.1148/radiol.12112638

185. Li Y-J, Ga S-N, Huo Y, Li S-Y, Gao X-G. Characteristics of hippocampal volumes in healthy Chinese from MRI. Neurol Res. Taylor & Francis; 2007;29: 803–806. doi:10.1179/016164107X223557

186. Shah P, Bassett DS, Wisse LEM, Detre JA, Stein JM, Yushkevich PA, et al. Mapping the structural and functional network architecture of the medial temporal lobe using 7T MRI. Hum Brain Mapp. Wiley-Blackwell; 2018;39: 851–865. doi:10.1002/hbm.23887 goo.gl/zRecRn

187. Henry TR, Chupin M, Lehericy S, Strupp JP, Sikora MA, Sha ZY, et al. Hippocampal sclerosis in temporal lobe epilepsy: findings at 7 T(1). Radiology. 2011;261: 199–209. doi:radiol.11101651 [pii]\r10.1148/radiol.11101651

188. Oppenheim C, Dormont D, Biondi A, Lehéricy S, Hasboun D, Clémenceau S, et al. Loss of digitations of the hippocampal head on high-resolution fast spin-echo MR: A sign of mesial temporal sclerosis. Am J Neuroradiol. 1998;19: 457–463.

189. Blümcke I, Thom M, Aronica E, Armstrong DD, Bartolomei F, Bernasconi A, et al. International consensus classification of hippocampal sclerosis in temporal lobe epilepsy: A Task Force report from the ILAE Commission on Diagnostic Methods. Epilepsia. 2013;54: 1315–1329. doi:10.1111/epi.12220

190. Bernhardt BC, Bernasconi A, Liu M, Hong S-J, Caldairou B, Goubran M, et al. The spectrum of structural and functional imaging abnormalities in temporal lobe epilepsy. Ann Neurol. 2016; 1–12. doi:10.1002/ana.24691

191. Lynall M-E, Bassett DS, Kerwin R, McKenna PJ, Kitzbichler M, Muller U, et al. Functional connectivity and brain networks in schizophrenia. J Neurosci. NIH Public Access; 2010;30: 9477–87. doi:10.1523/JNEUROSCI.0333-10.2010

192. Thom M. Review: Hippocampal sclerosis in epilepsy: a neuropathology review. Neuropathol Appl Neurobiol. Wiley-Blackwell; 2014;40: 520–43. doi:10.1111/nan.12150

193. Sone D, Sato N, Maikusa N, Ota M, Sumida K, Yokoyama K, et al. Automated subfield volumetric analysis of hippocampus in temporal lobe epilepsy using high-resolution T2-weighed MR imaging. 2016; doi:10.1016/j.nicl.2016.06.008

194. Bettus G, Bartolomei F, Confort-Gouny S, Guedj E, Chauvel P, Cozzone PJ, et al. Role of resting state functional connectivity MRI in presurgical investigation of mesial temporal lobe epilepsy. J Neurol Neurosurg Psychiatry. BMJ Publishing Group Ltd; 2010;81: 1147–54. doi:10.1136/jnnp.2009.191460

195. Bettus G, Guedj E, Joyeux F, Confort-Gouny S, Soulier E, Laguitton V, et al. Bettus G, Guedj E, Joyeux F, et al. Decreased basal fMRI functional connectivity in epileptogenic networks and contralateral compensatory mechanisms. Hum Brain Mapp. 2008;30: 1580–1591.

196. Bartolomei F, Wendling F, Régis J, Gavaret M, Guye M, Chauvel P. Pre-ictal synchronicity in limbic networks of mesial temporal lobe epilepsy. Epilepsy Res. 2004;61: 89–104. doi:10.1016/j.eplepsyres.2004.06.006

197. Uhlhaas PJ, Singer W. Neural Synchrony in Brain Disorders: Relevance for Cognitive Dysfunctions and Pathophysiology. Neuron. 2006;52: 155–168. doi:10.1016/j.neuron.2006.09.020

198. Bragin A, Engel J, Wilson CL, Fried I, Buzsáki G. High-frequency oscillations in

human brain. Hippocampus. 1999;9: 137–142. doi:10.1002/(SICI)1098-1063(1999)9:2<137::AID-HIPO5>3.0.CO;2-0

199. Schevon CA, Cappell J, Emerson R, Isler J, Grieve P, Goodman R, et al. Cortical abnormalities in epilepsy revealed by local EEG synchrony. Neuroimage. NIH Public Access; 2007;35: 140–8. doi:10.1016/j.neuroimage.2006.11.009

200. Bettus G, Wendling F, Guye M, Valton L, Régis J, Chauvel P, et al. Enhanced EEG functional connectivity in mesial temporal lobe epilepsy. Epilepsy Res. 2008;81: 58–68. doi:10.1016/j.eplepsyres.2008.04.020

201. Elkommos S, Weber B, Niehusmann P, Volmering E, Richardson MP, Goh YY, et al. Hippocampal internal architecture and postoperative seizure outcome in temporal lobe epilepsy due to hippocampal sclerosis. Seizure. Elsevier; 2016;35: 65–71. doi:10.1016/j.seizure.2016.01.007

202. Jackson GD, Berkovic SF, Duncan JS, Connelly A. Optimizing the diagnosis of hippocampal sclerosis using MR imaging. Am J Neuroradiol. 1993;14: 753–762. Available: http://www.ncbi.nlm.nih.gov/pubmed/8517369

203. Kuzniecky RI, Jackson GD. Magnetic Resonance in Epilepsy. Magnetic Resonance in Epilepsy. 2005. doi:10.1016/B978-0-12-431152-7.X5000-9

204. Fukuzako H, Yamada K, Kodama S, Yonezawa T, Fukuzako T, Takenouchi K, et al. Hippocampal volume asymmetry and age at illness onset in males with schizophrenia. Eur Arch Psychiatry Clin Neurosci. 1997;247: 248–51. Available: http://www.ncbi.nlm.nih.gov/pubmed/9444493

205. Shi F, Liu B, Zhou Y, Yu C, Jiang T. Hippocampal volume and asymmetry in mild cognitive impairment and Alzheimer's disease: Meta-analyses of MRI studies. Hippocampus. 2009;19: 1055–1064. doi:10.1002/hipo.20573

206. La Joie R, Perrotin A, De La Sayette V, Egret S, Doeuvre L, Belliard S, et al. Hippocampal subfield volumetry in mild cognitive impairment, Alzheimer's disease and semantic dementia. NeuroImage Clin. 2013;3: 155–162. doi:10.1016/j.nicl.2013.08.007

207. Bassett DS, Zurn P, Gold JI. On the nature and use of models in network neuroscience. Nature Reviews Neuroscience. 2018: 1–13. doi:10.1038/s41583-018-0038-8

208. Bom de Araujo N, Barca ML, Engedal K, Coutinho ESF, Deslandes AC, Laks J. Verbal fluency in Alzheimer's disease, Parkinson's disease, and major depression. Clinics. 2011;66: 623–627. doi:10.1590/S1807-59322011000400017

209. Metternich B, Buschmann F, Wagner K, Schulze-Bonhage A, Kriston L. Verbal Fluency in Focal Epilepsy: A Systematic Review and Meta-analysis. Neuropsychol Rev. Springer US; 2014;24: 200–218. doi:10.1007/s11065-014-9255-8

210. Ehlis A, Herrmann MJ, Plichta MM, Fallgatter AJ. Cortical activation during two verbal fluency tasks in schizophrenic patients and healthy controls as assessed by multi-channel near-infrared spectroscopy. 2007;156: 1–13. doi:10.1016/j.pscychresns.2006.11.007

211. Andreou G, Trott K. Verbal fluency in adults diagnosed with attention-deficit hyperactivity disorder (ADHD) in childhood. ADHD Atten Deficit Hyperact Disord. 2013;5: 343–351. doi:10.1007/s12402-013-0112-z

212. Troyer AK, Moscovitch M. Cognitive processes of verbal fluency tasks. Studies on neuropsychology, neurology, and cognition. 2006. p. xxiii, 365 . doi:10.4324/9780203720899

213. Shao Z, Janse E, Visser K, Meyer AS. What do verbal fluency tasks measure? Predictors of verbal fluency performance in older adults. Front Psychol. 2014;5. doi:10.3389/fpsyg.2014.00772

214. Hirshorn EA, Thompson-Schill SL. Role of the left inferior frontal gyrus in covert word retrieval: Neural correlates of switching during verbal fluency. Neuropsychol Cogn Affect Behav Neurosci. 2006;44: 2547–2557. doi:10.1016/j.neuropsychologia.2006.03.035

215. Boivin MJ, Giordani B, Berent S, Amato DA, Lehtinen S, Koeppe RA, et al. Verbal fluency and positron emission tomographic mapping of regional cerebral glucose metabolism. Cortex. Italy; 1992;28: 231–239.

216. Parks RW, Loewenstein DA, Dodrill KL, Barker WW, Yoshii F, Chang JY, et al. Cerebral metabolic effects of a verbal fluency test: A PET scan study. J Clin Exp Neuropsychol. Routledge; 1988;10: 565–575. doi:10.1080/01688638808402795

217. Schlösser R, Hutchinson M, Joseffer S, Rusinek H, Saarimaki A, Stevenson J, et al. Functional magnetic resonance imaging of human brain activity in a verbal fluency task. J Neurol Neurosurg Psychiatry. 1998;64: 492–498. doi:10.1136/jnnp.64.4.492

218. Abrahams S, Goldstein LH, Simmons A, Brammer MJ, Williams SCR, Giampietro VP, et al. Functional magnetic resonance imaging of verbal fluency and confrontation naming using compressed image acquisition to permit overt responses. Hum Brain Mapp. 2003;20: 29–40. doi:10.1002/hbm.10126

219. Li Y, Li P, Yang QX, Eslinger PJ, Sica CT, Karunanayaka P. Lexical-Semantic Search Under Different Covert Verbal Fluency Tasks: An fMRI Study. Front Behav Neurosci. 2017;11: 1–15. doi:10.3389/fnbeh.2017.00131

220. Paulesu E, Goldacre B, Scifo P, Cappa SF, Gilardi MC, Castiglioni I, et al. Functional heterogeneity of left inferior frontal cortex as revealed by fMRI. 2016;8: 2011–2016.

221. Heim S, Eickhoff SB, Ischebeck AK, Friederici AD, Stephan KE, Amunts K. Effective connectivity of the left BA 44, BA 45, and inferior temporal gyrus during lexical and phonological decisions identified with DCM. Hum Brain Mapp. Wiley Subscription Services, Inc., A Wiley Company; 2009;30: 392–402. doi:10.1002/hbm.20512

222. Birn RM, Kenworthy L, Case L, Caravella R, Jones TB, Bandettini PA, et al. Neural systems supporting lexical search guided by letter and semantic category cues: A self-paced overt response fMRI study of verbal fluency. Neuroimage. 2010;49: 1099–1107. doi:10.1016/j.neuroimage.2009.07.036

223. Glikmann-Johnston Y, Oren N, Hendler T, Shapira-Lichter I. Distinct functional connectivity of the hippocampus during semantic and phonemic fluency. Neuropsychologia. Elsevier; 2015;69: 39–49. doi:10.1016/j.neuropsychologia.2015.01.031

224. Tupak S V, Badewien M, Dresler T, Hahn T, Ernst LH, Herrmann MJ, et al. Neuropsychologia Differential prefrontal and frontotemporal oxygenation patterns during phonemic and semantic verbal fluency. Neuropsychologia. Elsevier Ltd; 2012;50: 1565–1569. doi:10.1016/j.neuropsychologia.2012.03.009

225. Kahlaoui K, Di G, Barbeau J, Maheux M, Lesage F, Ska B, et al. Brain & Language Contribution of NIRS to the study of prefrontal cortex for verbal fluency in aging. Brain Lang. Elsevier Inc.; 2012;121: 164–173. doi:10.1016/j.bandl.2011.11.002

226. Troyer AK, Moscovitch M, Winocur G. Clustering and switching as two components of verbal fluency: Evidence from younger and older healthy adults. Neuropsychology. 1997;11: 138–146. doi:10.1037/0894-4105.11.1.138

227. Billingsley RL, Simos PG, Castillo EM, Sarkari S, Breier JI, Pataraia E, et al. Spatio-Temporal Cortical Dynamics of Phonemic and Semantic Fluency. J Clin Exp Neuropsychol. 2004;26: 1031–1043. doi:10.1080/13803390490515333

228. Crone NE, Boatman D, Gordon B, Hao L. Induced electrocorticographic gamma activity during auditory perception. Brazier Award-winning article, 2001. Clin

Neurophysiol. 2001;112: 565–582. doi:10.1016/S1388-2457(00)00545-9

229. Towle VL, Castelle M, Edgar JC, Biassou NM, Frim DM, Spire J, et al. ECoG gamma activity during a language task : differentiating expressive and receptive speech areas. 2018; doi:10.1093/brain/awn147

230. Edwards E, Nagarajan SS, Dalal SS, Canolty RT, Kirsch HE, Barbaro NM, et al. Spatiotemporal imaging of cortical activation during verb generation and picture naming. Neuroimage. NIH Public Access; 2010;50: 291–301. doi:10.1016/j.neuroimage.2009.12.035

231. Sederberg PB, Kahana MJ, Howard MW, Donner EJ, Madsen JR. Theta and gamma oscillations during encoding predict subsequent recall. J Neurosci. 2003;23: 10809–10814. doi:23/34/10809 [pii]

232. Sederberg PB, Schulze-Bonhage A, Madsen JR, Bromfield EB, Litt B, Brandt A, et al. Gamma Oscillations Distinguish True From False Memories. Psychol Sci. 2007;18: 927–932. doi:10.1111/j.1467-9280.2007.02003.x

233. Jenkinson M, Beckmann CF, Behrens TEJ, Woolrich MW, Smith SM. Fsl. Neuroimage. 2012;62: 782–790. doi:10.1016/j.neuroimage.2011.09.015

234. Cervenka MC, Corines J, Boatman-Reich DF, Eloyan A, Sheng X, Franaszczuk PJ, et al. Electrocorticographic functional mapping identifies human cortex critical for auditory and visual naming. Neuroimage. Elsevier Inc.; 2013;69: 267–276. doi:10.1016/j.neuroimage.2012.12.037

235. Brumberg JS, Krusienski DJ, Chakrabarti S, Gunduz A, Brunner P, Ritaccio AL, et al. Spatio-Temporal Progression of Cortical Activity Related to Continuous Overt and Covert Speech Production in a Reading Task. PLoS One. Public Library of Science; 2016;11: e0166872. doi:10.1371/journal.pone.0166872

236. Gaillard W, Berl M, Moore E, Ritzl EK, Rosenberger L, Theodore WH. Atypical language in lesional and nonlesional complex partial epilepsy. Neurology. 2008;70: 1761–1771. doi:10.1212/01.wnl.0000316841.43348.20

237. Behroozmand R, Shebek R, Hansen DR, Oya H, Robin DA, Howard MA, et al. NeuroImage Sensory – motor networks involved in speech production and motor control : An fMRI study. Neuroimage. Elsevier Inc.; 2015;109: 418–428. doi:10.1016/j.neuroimage.2015.01.040

238. Bookheimer SY, Zeffiro TA, Blaxton TA, Gaillard W, Theodore WH. Activation of language cortex with automatic speech tasks. Neurology. 2000;55: 1151–1157. doi:10.1212/WNL.55.8.1151

239. Indefrey P. The Spatial and Temporal Signatures of Word Production Components: A Critical Update. Front Psychol. 2011;2: 1–16. doi:10.3389/fpsyg.2011.00255

240. Gaskell MG, Marslen-Wilson WD. Ambiguity, competition, and blending in spoken word recognition. Cogn Sci. 1999;23: 439–462. doi:10.1207/s15516709cog2304_3

241. Wen J, Yu T, Liu L, Hu Z, Yan J, Li Y, et al. Evaluating the roles of left middle frontal gyrus in word production using electrocorticography. Neurocase. Routledge; 2017;23: 263–269. doi:10.1080/13554794.2017.1387275

242. Bouchard KE, Mesgarani N, Johnson K, Chang EF. Functional organization of human sensorimotor cortex for speech articulation. Nature. Nature Publishing Group; 2013;495: 327–332. doi:10.1038/nature11911

243. Wise RJS, Scott SK, Blank SC, Mummery CJ, Murphy K, Warburton EA. Separate neural subsystems within "Wernicke"s area'. Brain. 2001;124: 83–95. doi:10.1093/brain/124.1.83

244. Blank SC. Speech production: Wernicke, Broca and beyond. Brain. 2002;125: 1829–1838. doi:10.1093/brain/awf191

245. Kutas M, Federmeier KD. Thirty Years and Counting: Finding Meaning in the N400 Component of the Event-Related Brain Potential (ERP). Annu Rev Psychol. 2011;62: 621–647. doi:10.1146/annurev.psych.093008.131123

246. Marinkovic K, Dhond RP, Dale AM, Glessner M, Carr V, Halgren E. Spatiotemporal Dynamics of Modality-Specific and Supramodal Word Processing. Neuron. 2003;38: 487–497. doi:10.1016/S0896-6273(03)00197-1

247. Piai V, Anderson KL, Lin JJ, Dewar C, Parvizi J, Dronkers NF, et al. Direct brain recordings reveal hippocampal rhythm underpinnings of language processing. Proc Natl Acad Sci. 2016;113: 11366–11371. doi:10.1073/pnas.1603312113

248. Covington N V., Duff MC. Expanding the Language Network: Direct Contributions from the Hippocampus. Trends Cogn Sci. Elsevier Ltd; 2016;xx: 1–2. doi:10.1016/j.tics.2016.10.006

249. Hamamé CM, Alario FX, Llorens A, Liégeois-Chauvel C, Trébuchon-Da Fonseca A. High frequency gamma activity in the left hippocampus predicts visual object naming performance. Brain Lang. 2014;135: 104–114. doi:10.1016/j.bandl.2014.05.007

250. Gleissner U, Elger C. The hippocampal contribution to verbal fluency in patients with temporal lobe epilepsy. Cortex. 2001;37: 55–63. doi:10.1016/S0010-9452(08)70557-4

251. Sheldon S, Moscovitch M. The nature and time-course of medial temporal lobe contributions to semantic retrieval: An fMRI study on verbal fluency. Hippocampus. 2012;22: 1451–1466. doi:10.1002/hipo.20985

252. Collard MJ, Fifer MS, Benz HL, McMullen DP, Wang Y, Milsap GW, et al. Cortical subnetwork dynamics during human language tasks. Neuroimage. 2016;135: 261–272. doi:10.1016/j.neuroimage.2016.03.072

253. Appelle S, Oswald LE. Simple Reaction Time as a Function of Alertness and Prior Mental Activity. Percept Mot Skills. 1974;38: 1263–1268.

254. Wang W, Degenhart AD, Sudre GP, Pomerleau DA, Tyler-Kabara EC. Decoding semantic information from human electrocorticographic (ECoG) signals. Proc Annu Int Conf IEEE Eng Med Biol Soc EMBS. 2011; 6294–6298. doi:10.1109/IEMBS.2011.6091553

255. World Health Organization. Epilepsy. In: WHO fact sheet. 2018.

256. French JA. Refractory epilepsy: Clinical overview. Epilepsia. 2007;48: 3–7. doi:10.1111/j.1528-1167.2007.00992.x

257. Lachaux JP, Rudrauf D, Kahane P. Intracranial EEG and human brain mapping. J Physiol Paris. 2003;97: 613–628. doi:10.1016/j.jphysparis.2004.01.018

258. Kramer MA, Cash SS. Epilepsy as a Disorder of Cortical Network Organization. Neurosci. SAGE PublicationsSage CA: Los Angeles, CA; 2012;18: 360–372. doi:10.1177/1073858411422754

259. Lopes MA, Richardson MP, Abela E, Rummel C, Schindler K, Goodfellow M, et al. Elevated ictal brain network ictogenicity enables prediction of optimal seizure control. Front Neurol. Frontiers; 2018;9: 98. doi:10.3389/fneur.2018.00098

260. Kramer MA, Kolaczyk ED, Kirsch HE. Emergent network topology at seizure onset in humans. Epilepsy Res. 2008;79: 173–186. doi:10.1016/j.eplepsyres.2008.02.002

261. Wagenaar JB, Brinkmann BH, Ives Z, Worrell GA, Litt B. A multimodal platform for cloud-based collaborative research. 2013 6th International IEEE/EMBS Conference on Neural Engineering (NER). IEEE; 2013. pp. 1386–1389. doi:10.1109/NER.2013.6696201

262. Kini LG, Davis KA, Wagenaar JB. Data integration: Combined imaging and electrophysiology data in the cloud. Neuroimage. Elsevier Inc.; 2016;124: 1175–1181. doi:10.1016/j.neuroimage.2015.05.075

263. Alsaadi TM, Ulmer JL, Mitchell MJ, Morris GL, Swanson SJ, Mueller WM. Magnetic Resonance Analysis of Postsurgical Temporal Lobectomy. J Neuroimaging. Wiley/Blackwell (10.1111); 2001;11: 243–247. doi:10.1111/j.1552-6569.2001.tb00041.x

264. Avants BB, Tustison NJ, Song G, Cook PA, Klein A, Gee JC. A reproducible evaluation of ANTs similarity metric performance in brain image registration. Neuroimage. 2011;54: 2033–2044. doi:10.1016/j.neuroimage.2010.09.025

265. Ludwig KA, Miriani RM, Langhals NB, Joseph MD, Anderson DJ, Kipke DR. Using a Common Average Reference to Improve Cortical Neuron Recordings From Microelectrode Arrays. J Neurophysiol. American Physiological Society; 2009;101: 1679–1689. doi:10.1152/jn.90989.2008

266. Kramer MA, Eden UT, Kolaczyk ED, Zepeda R, Eskandar EN, Cash SS. Coalescence and Fragmentation of Cortical Networks during Focal Seizures. J Neurosci. 2010;30: 10076–10085. doi:10.1523/JNEUROSCI.6309-09.2010

267. Khambhati AN, Davis KA, Oommen BS, Chen SH, Lucas TH, Litt B, et al. Dynamic Network Drivers of Seizure Generation, Propagation and Termination in Human Neocortical Epilepsy. PLoS Comput Biol. Public Library of Science; 2015;11: e1004608. doi:10.1371/journal.pcbi.1004608

268. Bromfield EB, Cavazos JE, Sirven JI. Basic Mechanisms Underlying Seizures and Epilepsy. American Epilepsy Society; 2006; Available: https://www.ncbi.nlm.nih.gov/books/NBK2510/?report=reader

269. Goodfellow M, Rummel C, Abela E, Richardson MP, Schindler K, Terry JR. Estimation of brain network ictogenicity predicts outcome from epilepsy surgery. Sci Rep. Nature Publishing Group; 2016;6: 29215. doi:10.1038/srep29215

270. Burns SP, Santaniello S, Yaffe RB, Jouny CC, Crone NE, Bergey GK, et al. Network dynamics of the brain and influence of the epileptic seizure onset zone. Proc Natl Acad Sci. 2014;111: E5321–E5330. doi:10.1073/pnas.1401752111

271. Li A, Chennuri B, Subramanian S, Yaffe R, Gliske S, Stacey W, et al. Using network analysis to localize the epileptogenic zone from invasive EEG recordings in intractable focal epilepsy. 2018; doi:10.1162/netn_a_00043

272. Sinha N, Dauwels J, Kaiser M, Cash SS, Brandon Westover M, Wang Y, et al.

Predicting neurosurgical outcomes in focal epilepsy patients using computational modelling. Brain. Oxford University Press; 2017;140: 319–332. doi:10.1093/brain/aww299

273. Yang C, Luan G, Wang Q, Liu Z, Zhai F, Wang QY. Localization of epileptogenic zone with the correction of pathological networks. Front Neurol. Frontiers; 2018;9: 143. doi:10.3389/FNEUR.2018.00143

274. Murin Y, Kim J, Parvizi J, Goldsmith A. SozRank: A new approach for localizing the epileptic seizure onset zone. Babadi B, editor. PLOS Comput Biol. Public Library of Science; 2018;14: e1005953. doi:10.1371/journal.pcbi.1005953

275. Kopell N, Ermentrout GB, Whittington MA, Traub RD. Gamma rhythms and beta rhythms have different synchronization properties. Proc Natl Acad Sci. 2000;97: 1867–1872. doi:10.1073/pnas.97.4.1867

276. Roopun AK. concatenation underlies interactions between gamma and beta rhythms in neocortex. Front Cell Neurosci. 2008;2. doi:10.3389/neuro.03.001.2008

277. Whittington MA, Traub RD, Kopell N, Ermentrout B, Buhl EH. Inhibition-based rhythms: Experimental and mathematical observations on network dynamics. International Journal of Psychophysiology. 2000. pp. 315–336. doi:10.1016/S0167-8760(00)00173-2

278. Chu CJ, Kramer MA, Pathmanathan J, Bianchi MT, Westover MB, Wizon L, et al. Emergence of Stable Functional Networks in Long-Term Human Electroencephalography. J Neurosci. 2012;32. Available: http://www.jneurosci.org/content/32/8/2703.short

279. Warren CP, Hu S, Stead M, Brinkmann BH, Bower MR, Worrell GA. Synchrony in Normal and Focal Epileptic Brain: The Seizure Onset Zone is Functionally Disconnected. 2010; 3530–3539. doi:10.1152/jn.00368.2010

280. Dauwels J, Eskandar E, Cash S. Localization of seizure onset area from intracranial non-seizure EEG by exploiting locally enhanced synchrony. Proceedings of the 31st Annual International Conference of the IEEE Engineering in Medicine and Biology Society: Engineering the Future of Biomedicine, EMBC 2009. IEEE; 2009. pp. 2180–2183. doi:10.1109/IEMBS.2009.5332447

281. Betzel RF, Medaglia JD, Kahn AE, Soffer J, Schonhaut DR, Bassett DS. Inter-regional ECoG correlations predicted by communication dynamics, geometry, and correlated gene expression. 2017; Available: https://arxiv.org/pdf/1706.06088.pdf

282. Owen LLW, Manning JR. Towards human Super EEG. bioRxiv. 2017; 1–20.

doi:10.1101/121020

283. Frauscher B, von Ellenrieder N, Zelmann R, Doležalová I, Minotti L, Olivier A, et al. Atlas of the normal intracranial electroencephalogram: neurophysiological awake activity in different cortical areas. Brain. 2018;141: 1130–1144. doi:10.1093/brain/awy035

284. Hesdorffer DC, Logroscino G, Benn EKT, Katri N, Cascino G, Hauser WA. Estimating risk for developing epilepsy: a population-based study in Rochester, Minnesota. Neurology. Wolters Kluwer Health, Inc. on behalf of the American Academy of Neurology; 2011;76: 23–7. doi:10.1212/WNL.0b013e318204a36a

285. Biswal B, Zerrin Yetkin F, Haughton VM, Hyde JS. Functional connectivity in the motor cortex of resting human brain using echo-planar mri. Magn Reson Med. Wiley Subscription Services, Inc., A Wiley Company; 1995;34: 537–541. doi:10.1002/mrm.1910340409

286. Salvador R, Suckling J, Coleman MR, Pickard JD, Menon D, Bullmore E. Neurophysiological Architecture of Functional Magnetic Resonance Images of Human Brain. Cereb Cortex. Oxford University Press; 2004;15: 1332–1342. doi:10.1093/cercor/bhi016

287. Stam CJ. Functional connectivity patterns of human magnetoencephalographic recordings: A “small-world” network? Neurosci Lett. 2004;355: 25–28. doi:10.1016/j.neulet.2003.10.063

288. Micheloyannis S, Pachou E, Stam CJ, Vourkas M, Erimaki S, Tsirka V. Using graph theoretical analysis of multi channel EEG to evaluate the neural efficiency hypothesis. Neurosci Lett. 2006;402: 273–277. doi:10.1016/j.neulet.2006.04.006

289. Raj A, Mueller SG, Young K, Laxer KD, Weiner M. Network-level analysis of cortical thickness of the epileptic brain. Neuroimage. 2010;52: 1302–13. doi:10.1016/j.neuroimage.2010.05.045

290. Taylor PN, Han CE, Schoene-Bake J-C, Weber B, Kaiser M. Structural connectivity changes in temporal lobe epilepsy: Spatial features contribute more than topological measures. 2015; doi:10.1016/j.nicl.2015.02.004

291. Vaessen MJ, Jansen JFA, Vlooswijk MCG, Hofman PAM, Majoie HJM, Aldenkamp AP, et al. White Matter Network Abnormalities Are Associated with Cognitive Decline in Chronic Epilepsy. Cereb Cortex. 2012;22: 2139–2147. doi:10.1093/cercor/bhr298

292. de Campos BM, Coan AC, Lin Yasuda C, Casseb RF, Cendes F. Large-scale brain

networks are distinctly affected in right and left mesial temporal lobe epilepsy. Hum Brain Mapp. 2016;0. doi:10.1002/hbm.23231

293. Proix T, Bartolomei F, Guye M, Jirsa VK. Individual structural connectivity defines propagation networks in partial epilepsy. 2016; Available: http://arxiv.org/abs/1604.08508

294. Jirsa VK, Proix T, Perdikis D, Woodman MM, Wang H, Gonzalez-Martinez J, et al. The Virtual Epileptic Patient: Individualized whole-brain models of epilepsy spread. Neuroimage. Academic Press; 2017;145: 377–388. doi:10.1016/J.NEUROIMAGE.2016.04.049

295. Vlooswijk MCG, Vaessen MJ, Jansen JFA, de Krom MCFTM, Majoie HJM, Hofman PAM, et al. Loss of network efficiency associated with cognitive decline in chronic epilepsy. Neurology. 2011;77: 938–944. doi:10.1212/WNL.0b013e31822cfc2f

296. Honey CJ, Sporns O, Cammoun L, Gigandet X, Thiran JP, Meuli R, et al. Predicting human resting-state functional connectivity from structural connectivity. Proc Natl Acad Sci U S A. National Academy of Sciences; 2009;106: 2035–40. doi:10.1073/pnas.0811168106

297. Zhang D, Snyder AZ, Shimony JS, Fox MD, Raichle ME. Noninvasive functional and structural connectivity mapping of the human thalamocortical system. Cereb Cortex. Oxford University Press; 2010;20: 1187–94. doi:10.1093/cercor/bhp182

298. Finger H, Bönstrup M, Cheng B, Messé A, Hilgetag C, Thomalla G, et al. Modeling of Large-Scale Functional Brain Networks Based on Structural Connectivity from DTI: Comparison with EEG Derived Phase Coupling Networks and Evaluation of Alternative Methods along the Modeling Path. PLoS Comput Biol. 2016;12. doi:10.1371/journal.pcbi.1005025

299. Skudlarski P, Jagannathan K, Calhoun VD, Hampson M, Skudlarska BA, Pearlson G. Measuring brain connectivity: Diffusion tensor imaging validates resting state temporal correlations. Neuroimage. Elsevier Inc.; 2008;43: 554–561. doi:10.1016/j.neuroimage.2008.07.063

300. Hagmann P, Sporns O, Madan N, Cammoun L, Pienaar R, Wedeen VJ, et al. White matter maturation reshapes structural connectivity in the late developing human brain. Proc Natl Acad Sci U S A. National Academy of Sciences; 2010;107: 19067–72. doi:10.1073/pnas.1009073107

301. Rubinov M, Sporns O, van Leeuwen C, Breakspear M. Symbiotic relationship between brain structure and dynamics. BMC Neurosci. 2009;10.

doi:10.1186/1471-2202-10-55

302. Greicius, Supekar, Menon, Dougherty. Resting-state functional connectivity reflects structural connectivity in the default mode network. Cereb Cortex. 2009;19: 72–78. Available: http://www.ncbi.nlm.nih.gov/entrez/query.fcgi?db=pubmed&cmd=Retrieve&dopt=AbstractPlus&list_uids=18403396%5Cnpapers://3fee8da1-24f9-490b-9ed9-3b7bcb767493/Paper/p21

303. Chu CJ, Tanaka N, Diaz J, Edlow BL, Wu O, Hämäläinen M, et al. EEG functional connectivity is partially predicted by underlying white matter connectivity. Neuroimage. 2015;108: 23–33. doi:10.1016/j.neuroimage.2014.12.033

304. Zhang Z, Liao W, Chen H, Mantini D, Ding JR, Xu Q, et al. Altered functional-structural coupling of large-scale brain networks in idiopathic generalized epilepsy. Brain. 2011;134: 2912–2928. doi:10.1093/brain/awr223

305. Chiang S, Stern JM, Engel J, Haneef Z. Structural-functional coupling changes in temporal lobe epilepsy. Brain Res. 2015;1616: 45–57. doi:10.1016/j.brainres.2015.04.052

306. Penfield W, Jasper H. Epilepsy and the Functional Anatomy of the Human Brain. JAMA J Am Med Assoc. 1954;155: 86–86. doi:10.1001/jama.1954.03690190092039

307. Tuch DS, Reese TG, Wiegell MR, Makris N, Belliveau JW, Van Wedeen J. High angular resolution diffusion imaging reveals intravoxel white matter fiber heterogeneity. Magn Reson Med. 2002;48: 577–582. doi:10.1002/mrm.10268

308. Litt B, Esteller R, Echauz J, D'Alessandro M, Shor R, Henry T, et al. Epileptic seizures may begin hours in advance of clinical onset: A report of five patients. Neuron. 2001;30: 51–64. doi:10.1016/S0896-6273(01)00262-8

309. Fisher RS, Cross JH, Souza CD', French JA, Haut SR, Higurashi N, et al. Instruction manual for the ILAE 2017 operational classification of seizure types. Epilepsia. 2017;58: 531–542. doi:10.1111/epi.13671

310. Tzourio-Mazoyer N, Landeau B, Papathanassiou D, Crivello F, Etard O, Delcroix N, et al. Automated Anatomical Labeling of Activations in SPM Using a Macroscopic Anatomical Parcellation of the MNI MRI Single-Subject Brain. Neuroimage. 2002;15: 273–289. doi:10.1006/nimg.2001.0978

311. Desikan RS, Ségonne F, Fischl B, Quinn BT, Dickerson BC, Blacker D, et al. An

automated labeling system for subdividing the human cerebral cortex on MRI scans into gyral based regions of interest. Neuroimage. 2006;31: 968–980. doi:10.1016/j.neuroimage.2006.01.021

312. Avants BB, Epstein CL, Grossman M, Gee JC. Symmetric diffeomorphic image registration with cross-correlation: Evaluating automated labeling of elderly and neurodegenerative brain. Med Image Anal. 2008;12: 26–41. doi:10.1016/j.media.2007.06.004

313. Andersson JLR, Sotiropoulos SN. An integrated approach to correction for off-resonance effects and subject movement in diffusion MR imaging. Neuroimage. Academic Press; 2016;125: 1063–1078. doi:10.1016/J.NEUROIMAGE.2015.10.019

314. Greve DN, Fischl B. Accurate and robust brain image alignment using boundary-based registration. Neuroimage. 2009;48: 63–72. doi:10.1016/j.neuroimage.2009.06.060

315. Wang S, Peterson DJ, Gatenby JC, Li W, Grabowski TJ, Madhyastha TM. Evaluation of Field Map and Nonlinear Registration Methods for Correction of Susceptibility Artifacts in Diffusion MRI. Front Neuroinform. Frontiers; 2017;11: 17. doi:10.3389/fninf.2017.00017

316. Yeh FC, Wedeen VJ, Tseng WYI. Generalized q-sampling imaging. IEEE Trans Med Imaging. 2010;29: 1626–1635. doi:10.1109/TMI.2010.2045126

317. Otsu N. Threshold selection method from gray level histograms. IEEE Trans Syst Man Cybern. 1979;SMC-9: 62–66. Available: https://www.scopus.com/record/display.uri?eid=2-s2.0-0018306059&origin=inward&txGid=b0cd16e2e7bd0be890360eee58c9bfb3

318. Taylor PN, Sinha N, Wang Y, Vos SB, de Tisi J, Miserocchi A, et al. The impact of epilepsy surgery on the structural connectome and its relation to outcome. NeuroImage Clin. Elsevier; 2018;18: 202–214. doi:10.1016/J.NICL.2018.01.028

319. Bonilha L, Gleichgerrcht E, Nesland T, Rorden C, Fridriksson J. Gray Matter Axonal Connectivity Maps. Front Psychiatry. Frontiers; 2015;6: 35. doi:10.3389/fpsyt.2015.00035

320. Park B, Eo J, Park H-J. Structural Brain Connectivity Constrains within-a-Day Variability of Direct Functional Connectivity. Front Hum Neurosci. Frontiers; 2017;11: 408. doi:10.3389/fnhum.2017.00408

321. Halekoh U, Højsgaard S. A Kenward-Roger Approximation and Parametric

Bootstrap Methods for Tests in Linear Mixed Models - The R Package pbkrtest. J Stat Softw. 2014;59: 1–32. doi:10.18637/jss.v059.i09

322. Davison AC (Anthony C, Hinkley D V. Bootstrap methods and their application. Technometrics. 1997; 582. doi:10.2307/1271471

323. Anderson MJ. Permutational Multivariate Analysis of Variance (PERMANOVA). Wiley StatsRef: Statistics Reference Online. Chichester, UK: John Wiley & Sons, Ltd; 2017. pp. 1–15. doi:10.1002/9781118445112.stat07841

324. Donahue CJ, Sotiropoulos SN, Jbabdi S, Hernandez-Fernandez M, Behrens TE, Dyrby TB, et al. Using Diffusion Tractography to Predict Cortical Connection Strength and Distance: A Quantitative Comparison with Tracers in the Monkey. J Neurosci. Society for Neuroscience; 2016;36: 6758–70. doi:10.1523/JNEUROSCI.0493-16.2016

325. Kaiser M, Hilgetag CC. Modelling the development of cortical systems networks. Neurocomputing. 2004;58–60: 297–302. doi:10.1016/j.neucom.2004.01.059

326. Lewis JD, Theilmann RJ, Sereno MI, Townsend J. The relation between connection length and degree of connectivity in young adults: A DTI analysis. Cereb Cortex. 2009;19: 554–562. doi:10.1093/cercor/bhn105

327. Rubinov M, Ypma RJF, Watson C, Bullmore ET. Wiring cost and topological participation of the mouse brain connectome. Proc Natl Acad Sci. 2015;112: 10032–10037. doi:10.1073/pnas.1420315112

328. He BJ, Raichle ME. The fMRI signal, slow cortical potential and consciousness. Trends Cogn Sci. 2009;13: 302–309. doi:10.1016/j.tics.2009.04.004

329. He B, Liu Z. Multimodal Functional Neuroimaging: Integrating Functional MRI and EEG/MEG. IEEE Rev Biomed Eng. NIH Public Access; 2008;1: 23–40. doi:10.1109/RBME.2008.2008233

330. Logothetis NK, J P, M A, T T, A O. Neurophysiological investigation of thebasis of the fMRI signal. Nature. 2001; 1–8. Available: https://www.nature.com/nature/journal/v412/n6843/pdf/412150a0.pdf

331. Ko AL, Darvas F, Poliakov A, Ojemann J, Sorensen LB. Quasi-periodic Fluctuations in Default Mode Network Electrophysiology. J Neurosci. 2011;31: 11728–11732. doi:10.1523/JNEUROSCI.5730-10.2011

332. Miller KJ, Leuthardt EC, Schalk G, Rao RPN, Anderson NR, Moran DW, et al. Spectral Changes in Cortical Surface Potentials during Motor Movement. J

Neurosci. 2007;27: 2424–2432. doi:10.1523/JNEUROSCI.3886-06.2007

333. Luders H, LoRusso G, Miller JP, Gonzalez-Martinez J, Kahane P, Lhatoo S. Stereotactic electroencephalography (SEEG) in the pre-surgical investigation of refractory focal epilepsy. Epilepsy Curr. 2013;13: 492. Available: http://www.embase.com/search/results?subaction=viewrecord&from=export&id=L71197314%5Cnhttp://www.aesnet.org/file/13-1-s-2012-meeting-abstract-supplement%5Cnhttp://sfx.library.uu.nl/utrecht?sid=EMBASE&issn=15357597&id=doi:&atitle=Stereotactic+electroenceph

334. Cossu M, Cardinale F, Castana L, Citterio A, Francione S, Tassi L, et al. Stereoelectroencephalography in the presurgical evaluation of focal epilepsy: a retrospective analysis of 215 procedures. Neurosurgery. 2005;57. doi:10.1093/neurosurgery/57.4.706

335. Varotto G, Tassi L, Franceschetti S, Spreafico R, Panzica F. Epileptogenic networks of type II focal cortical dysplasia: A stereo-EEG study. Neuroimage. 2012;61: 591–598. doi:10.1016/j.neuroimage.2012.03.090

336. Wenzel M, Hamm JP, Peterka DS, Yuste R. Reliable and Elastic Propagation of Cortical Seizures In Vivo. Cell Rep. Cell Press; 2017;19: 2681–2693. doi:10.1016/J.CELREP.2017.05.090

337. Alstott J, Breakspear M, Hagmann P, Cammoun L, Sporns O. Modeling the Impact of Lesions in the Human Brain. Friston KJ, editor. PLoS Comput Biol. Public Library of Science; 2009;5: e1000408. doi:10.1371/journal.pcbi.1000408

338. Honey CJ, Sporns O. Dynamical consequences of lesions in cortical networks. Hum Brain Mapp. Wiley-Blackwell; 2008;29: 802–809. doi:10.1002/hbm.20579

339. Rafal RD, Koller K, Bultitude JH, Mullins P, Ward R, Mitchell AS, et al. Connectivity between the superior colliculus and the amygdala in humans and macaque monkeys: virtual dissection with probabilistic DTI tractography. J Neurophysiol. American Physiological Society Bethesda, MD; 2015;114: 1947–1962. doi:10.1152/jn.01016.2014

340. Assaf Y, Pasternak O. Diffusion tensor imaging (DTI)-based white matter mapping in brain research: A review. J Mol Neurosci. 2008;34: 51–61. doi:10.1007/s12031-007-0029-0

341. Le Bihan D, Poupon C, Amadon A, Lethimonnier F. Artifacts and pitfalls in diffusion MRI. J Magn Reson Imaging. Wiley-Blackwell; 2006;24: 478–488. doi:10.1002/jmri.20683

342. Mamata H, Mamata Y, Westin C-F, Shenton ME, Kikinis R, Jolesz FA, et al. High-resolution line scan diffusion tensor MR imaging of white matter fiber tract anatomy. AJNR Am J Neuroradiol. American Journal of Neuroradiology; 2002;23: 67–75. Available: http://www.ncbi.nlm.nih.gov/pubmed/11827877

343. Badawy RAB, Harvey AS, Macdonell RAL. Cortical hyperexcitability and epileptogenesis: Understanding the mechanisms of epilepsy - Part 2 [Internet]. Journal of Clinical Neuroscience. Churchill Livingstone; 2009. pp. 485–500. doi:10.1016/j.jocn.2008.10.001

344. Estrada E, Hatano N. Communicability in complex networks. Phys Rev E - Stat Nonlinear, Soft Matter Phys. 2008;77. doi:10.1103/PhysRevE.77.036111

345. Honey CJ, Thivierge J-P, Sporns O. Can structure predict function in the human brain? Neuroimage. 2010;52: 766–776. doi:10.1016/j.neuroimage.2010.01.071

346. Díaz-Parra A, Osborn Z, Canals S, Moratal D, Sporns O. Structural and functional, empirical and modeled connectivity in the cerebral cortex of the rat. Neuroimage. Academic Press; 2017;159: 170–184. doi:10.1016/J.NEUROIMAGE.2017.07.046